AFRL-RV-PS-
TR-2018-0076

AFRL-RV-PS-
TR-2018-0076

BODY AND SURFACE WAVES FROM MULTIPLE NEAR-SIMULTANEOUS NUCLEAR EXPLOSIONS

Jeffry L. Stevens and Michael O'Brien

Leidos
10260 Campus Point Drive
San Diego, CA 92121

15 May 2018

Final Report

AIR FORCE RESEARCH LABORATORY
Space Vehicles Directorate
3550 Aberdeen Ave SE
AIR FORCE MATERIEL COMMAND
KIRTLAND AIR FORCE BASE, NM 87117-5776

DTIC COPY

NOTICE AND SIGNATURE PAGE

AFRL-RV-PS-TR-2018-0076 HAS BEEN REVIEWED AND IS APPROVED FOR PUBLICATION IN ACCORDANCE WITH ASSIGNED DISTRIBUTION STATEMENT.

//SIGNED//	//SIGNED//
Dr. Frederick Schult Program Manager/AFRL/RVBYE	Dr. Thomas R. Caudill, Chief AFRL Battlespace Environment Division

REPORT DOCUMENTATION PAGE	*Form Approved* *OMB No. 0704-0188*

1. REPORT DATE *(DD-MM-YYYY)* 15-05-2018	**2. REPORT TYPE** Final Report	**3. DATES COVERED** *(From - To)* 08 Apr 2016 – 07 Apr 2018

4. TITLE AND SUBTITLE Body and Surface Waves from Multiple Near-Simultaneous Nuclear Explosions	**5a. CONTRACT NUMBER** FA9453-16-C-0020
	5b. GRANT NUMBER
	5c. PROGRAM ELEMENT NUMBER 62601F
6. AUTHOR(S) Jeffry L. Stevens and Michael O'Brien	**5d. PROJECT NUMBER** 1010
	5e. TASK NUMBER PPM00027859
	5f. WORK UNIT NUMBER EF128744
7. PERFORMING ORGANIZATION NAME(S) AND ADDRESS(ES) Leidos 10260 Campus Point Drive San Diego, CA 92121	**8. PERFORMING ORGANIZATION REPORT NUMBER**
9. SPONSORING / MONITORING AGENCY NAME(S) AND ADDRESS(ES) Air Force Research Laboratory Space Vehicles Directorate 3550 Aberdeen Avenue SE Kirtland AFB, NM 87117-5776	**10. SPONSOR/MONITOR'S ACRONYM(S)** AFRL/RVBYE
	11. SPONSOR/MONITOR'S REPORT NUMBER(S) AFRL-RV-PS-TR-2018-0076

12. DISTRIBUTION / AVAILABILITY STATEMENT

Approved for public release; distribution is unlimited. (AFMC-2018-0441 dtd 01 Oct 2018)

13. SUPPLEMENTARY NOTES

14. ABSTRACT

We perform numerical simulations of multiple near-simultaneous explosions, and evaluate the effect of the close location in time and space on body and surface waves. We perform a set of 2D axisymmetric calculations of double and triple explosions using the Eulerian hydrodynamic code STELLAR; extending the representation theorem code to work with STELLAR; and propagating these calculations to far-field body waves. The calculations show that at low frequencies far-field body waves from multiple explosions are identical to those from a single explosion of the same yield, but at high frequencies the body waves differ. We modify CRAM3D to allow calculations of multiple explosions and run calculations using the same depths and separations used in the STELLAR calculations, but now including the free surface and three-dimensional effects. The results are consistent with the STELLAR calculations, but the CRAM3D calculations also allow us to calculate surface reflected phases, surface waves and full regional seismograms. Long period surface waves show azimuthal variability for multiple explosions in a horizontal configuration. Although we find some differences in higher frequency body waves and in surface waves, the differences are small enough to conclude that yield estimates derived from seismic signals from multiple explosions should in most cases be an accurate estimate of the total yield of the explosions.

15. SUBJECT TERMS

nonlinear finite element calculations, nuclear explosion monitoring, multiple explosions

16. SECURITY CLASSIFICATION OF:			**17. LIMITATION OF ABSTRACT**	**18. NUMBER OF PAGES**	**19a. NAME OF RESPONSIBLE PERSON** Dr. Frederick Schult
a. REPORT Unclassified	**b. ABSTRACT** Unclassified	**c. THIS PAGE** Unclassified	Unlimited	**68**	**19b. TELEPHONE NUMBER** *(include area code)*

This page is intentionally left blank.

Table of Contents

List of Figures

List of Tables

1. Summary

We perform numerical simulations of multiple near-simultaneous explosions, and evaluate the effect of the close location in time and space on body and surface waves. We perform a set of 2D axisymmetric calculations of double and triple explosions using the Eulerian hydrodynamic code STELLAR; extending the representation theorem code to work with STELLAR; and propagating these calculations to far-field body waves. The calculations show that at low frequencies far-field body waves from multiple explosions are identical to those from a single explosion of the same yield, but at high frequencies the body waves differ (Figure 1).

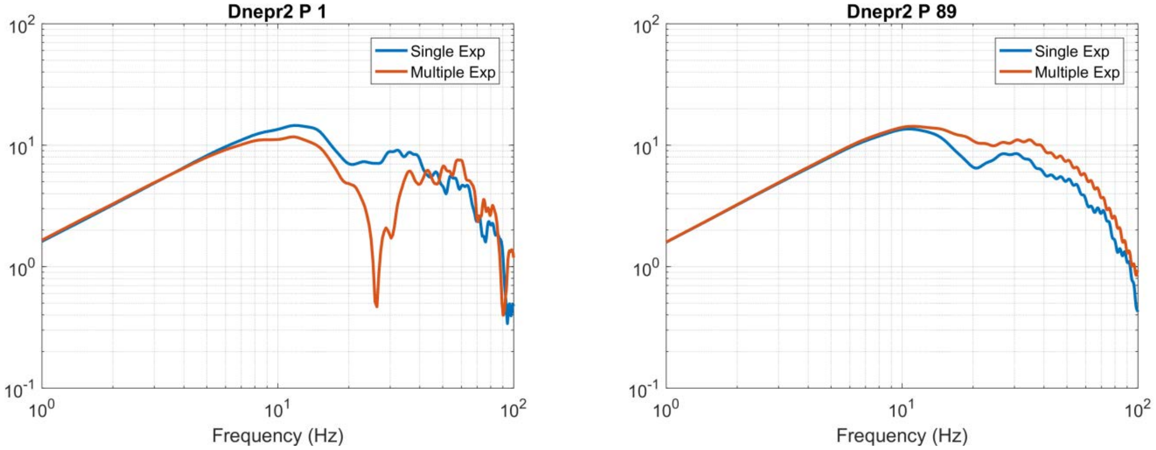

Figure 1. Dnepr2 double and yield equivalent single explosion P-wave spectra. ***Single explosion spectrum is higher along axis of the two explosions (left), while P-wave spectrum from the double explosion is higher perpendicular to the axis. Differences vanish at low frequencies.***

We modify CRAM3D to allow calculations of multiple explosions and run calculations using the same depths and separations used in the STELLAR calculations, but now including the free surface and three-dimensional effects (Figure 2). The results are generally consistent with the STELLAR calculations, but the CRAM3D calculations also allow us to calculate surface reflected phases, surface waves and full regional seismograms. Long period surface waves show azimuthal variability for multiple explosions in a horizontal configuration. In the Dnepr2 calculation shown in Figure 2, surface waves are smaller along the axis between the two explosions and larger in the perpendicular direction.

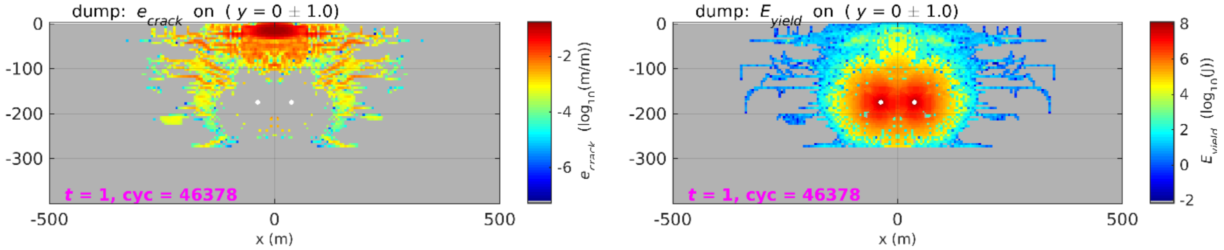

Figure 2. Dnepr2: Tensile crack strains (left) and plastic work (right) show regions of nonlinear deformation.

Although we find some differences in higher frequency body waves and in surface waves, the differences are small enough to conclude that yield estimates derived from seismic signals from multiple explosions should in most cases be an accurate estimate of the total yield of the explosions.

2. Introduction

An important open nuclear monitoring question is whether multiple nuclear explosions conducted either simultaneously or very close together in time generate seismic waves that are sufficiently different from a tamped single explosion to cause errors in yield estimation or discrimination. In particular, Novaya Zemlya tests with multiple explosions were observed to have low m_b, leading to underestimation of the total explosion yield. According to Murphy and Barker (2001), "aggregate yields of Novaya Zemlya explosions published by the Russian Federation (1996) can be interpreted to suggest that the Semipalatinsk m_b/yield relation may underestimate the yields of Novaya Zemlya tests by as much as a factor of two." In addition, a recent Russian book by Adushkin and Spivak (2007) indicates that single, vertical borehole explosions at the Southern Novaya Zemlya test site show the same m_b/yield relation as Semipalatinsk. This shows that the anomaly at the Northern Novaya Zemlya test site at Matochkin Shah cannot be attributed to differences in upper mantle attenuation relative to Semipalatinsk.

The Russian Federation report lists the number of "salvo explosions"[1] for each event together with a yield range, and there are as many as eight separate devices in a single test. Similarly, Figure 3 shows a US test, Rio Blanco, which consists of 3 nearly identical explosions (e.g. Von Seggern, 1974).

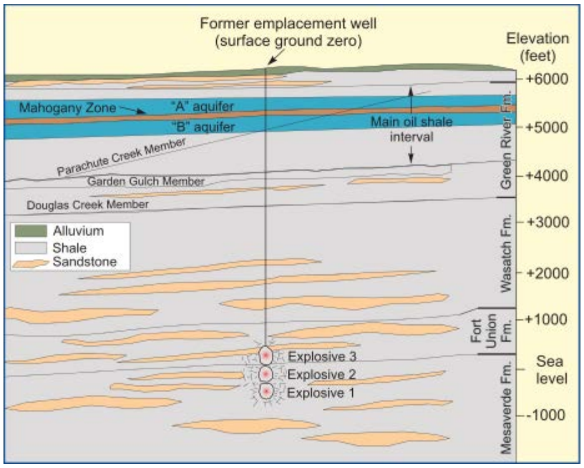

Figure 3. The Rio Blanco nuclear test consisted of three 33 kiloton explosions vertically spaced approximately 100 meters apart.

To address this question, we perform numerical simulations of multiple explosions consistent with the separation distances and yields of known multiple nuclear explosions. We then use the representation theorem to calculate far-field body waves, surface waves and when appropriate, regional phases (Stevens et al, 1991, 2011). Calculation of far-field body waves is the most important result, because they directly show the change in m_b due to variations in the source. We perform simulations for multiple events with known yields and event separations and then determine the change in m_b caused by multiple detonations.

---

[1] A "salvo explosion" is defined to mean two or more separate explosions where the period of time between successive individual explosions does not exceed 5 seconds and where the burial points of all explosive devices can be connected by the segments of straight lines, each of them connecting two burial points and it does not exceed 40 kilometers in length (Russian Federation, 1996).

3. Technical Approach

3.1. The CRAM3D Code

CRAM 3D is an explicit three-dimensional Lagrangian finite element code designed to run on multiple processors (Stevens et al, 2011, 2014, 2017). For an explosion simulation, the cavity is placed near the center of the grid and is enclosed by a spider grid which facilitates applying the pressure boundary condition and rezoning elements (Figure 4). The well-tested nonlinear material models from CRAM 2D have been implemented in CRAM 3D. The code includes gravity and so includes the important effects that result from variation of overburden pressure with depth. Gravitational equilibrium is established by running an initial calculation with no source, followed by a second calculation including the explosion source. CRAM3D also has the capability to include tectonic prestress in the calculations. In this project, we extend CRAM3D to be able to calculate multiple near-simultaneous explosions.

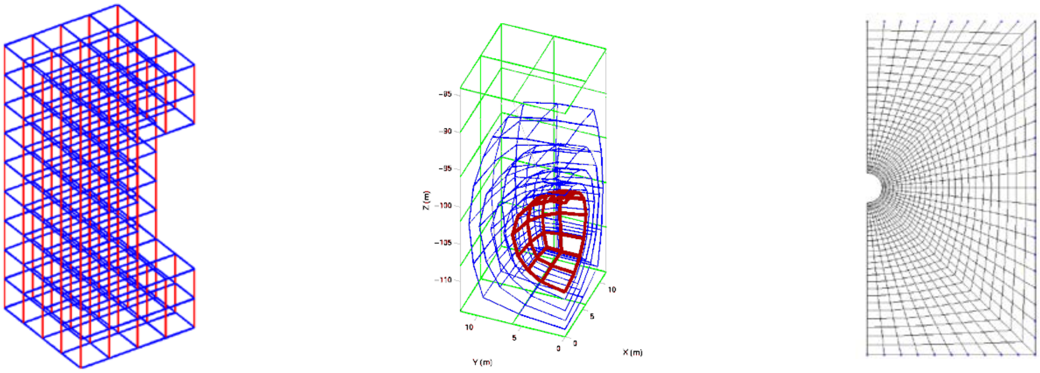

Figure 4. The CRAM 3D finite element outer grid (left) is rectangular. ***The inner grid (center) is shaped to match the shape of the explosion shock wave. CRAM2D uses a similar axisymmetric spider grid (right) in the region around the explosion.***

3.2. Propagation with the Elastodynamic Representation Theorem

The representation theorem allows us to perform arbitrarily complex nonlinear calculations in the source region, and then propagate them with an appropriate Green's function. The representation theorem is exact. That is, no matter how complex the 3D motion is on the source region boundary, it will be correctly propagated by the representation theorem. The only exception is that it will not calculate the interaction of backscattered waves reflected from outside the source region with complexities of the source region.

In the three-dimensional numerical finite difference calculations, we save displacements and stresses due to the seismic source on a monitoring surface on the boundary of a rectangle (5 planar surfaces, excluding the upper surface), and calculate Green's functions from each point on the monitoring surface to the receiver and so the synthetic seismogram at the receiver point X outside of the monitoring surface is obtained by integrating over the monitoring surface S_M

$$u_i(X) = \int\limits_{S_M} \Big\{ G_j^i(\xi; X) * T_j^M(\xi) - u_j^M(\xi) * S_{jk}^i(\xi; X) n_k \Big\} dA \qquad (1)$$

in the frequency domain, where $G_j^i(\xi;X)$ and $S_{jk}^i(\xi;X)$ are the Green's function and the stress tensor on the monitoring surface due to a unit impulsive force at *X* in direction *i*, T_j^M is the traction on the monitoring surface due to the seismic source, *u* is the displacement on the monitoring surface, and *n* is the normal to the monitoring surface. The operator * denotes convolution and the summation convention is assumed.

We use a plane-layered Green's function outside the source region. The Green's functions for the complete seismograms are derived from an algorithm based on the work of Luco and Apsel (1983) and Apsel and Luco (1983). The technique used for surface waves is similar to the method of Bache et al. (1982). The Green's functions for body waves are generated by a procedure similar to that described by Bache and Harkrider (1976) using a saddle point approximation to calculate a far-field plane wave for a given takeoff angle from a source in a plane-layered medium. We use a similar technique to calculate far-field body waves in a whole space for calculations without a free surface.

3.3. The STELLAR Eulerian Finite Difference Code

STELLAR is a second-order accurate Eulerian one-, two- and three-dimensional stress wave propagation code, developed using the methodology of Colella and Woodward (1984). It is very useful for calculating explosions that are close together because it handles strong interactions and strongly deformed boundaries. It also handles material strength correctly, which is uncommon for Eulerian codes. We have used STELLAR for a number of projects for calculations of partially decoupled cavities of various shapes (e.g. Rimer et al, 1994). The technique is to run STELLAR until the shock wave has propagated well into the surrounding material, and then overlay the solution into CRAM to propagate it into the elastic region, and finally use the representation theorem to propagate the solution to teleseismic distances. In the current project, we have extended the representation theorem code so that it works directly with STELLAR output.

4. Results and Discussion

4.1 STELLAR Calculations of Multiple Explosions

We use the Eulerian hydrodynamic code STELLAR to calculate the strong interaction between multiple explosions and far field body waves from these explosions. STELLAR is particularly useful for cases where the explosions are at comparable depth and deep enough that the interaction with the free surface is not a dominating effect. In this chapter we perform calculations of nine known multiple explosions and a single explosion that was close to one of the multiple explosions. For each of the multiple explosions we also perform a calculation of a single explosion with the same total yield as the multiple explosions. The explosions calculated are listed in Table 1.

Table 1. List of explosions used for calculations (from Sultanov et al, 1999).

Event	Date	Depths and Yield
Azgir 1	1978/10/17	18 kt at 1040m depth + 56 kt at 970m
Azgir 2	1979/01/17	12.5 kt at 995m depth + 56 kt, at 934m
Azgir 3	1979/07/14	Three 7kt, depths 849, 916 and 983m (916±66m)
Azgir 10	1979/10/24	Two 16.5 kt, depths 915m and 980m
Butane 1	1965/03/30	Two 2.3 kt explosions, 200m apart, 1341m and 1375m depth
Dnepr 2	1984/08/27	Two 1.7 kt at 175m depth, 75m apart
Dnepr 1	1972/09/04	Single explosion 2.1 kt at 131m depth in the same mine as Dnepr 2
Rio Blanco	1973/05/17	Three 33kt, depths 1779, 1899 and 2039m (1900±126m)
Taiga	1971/03/23	Three 15 kt explosions at 127m depth separated by 165m
Telkem 2	1968/11/12	Three 0.24 kt at 31.4m depth, 40m separation

Salt was used as the material for all of the calculations. Although some of the explosions were in different materials, salt was used because it is a relatively simple material and it allows us to do a more direct comparison of the effects of differing source yields, separations and depths. The explosion was modeled as a sphere of vaporized salt containing the energy of the explosion. The size of the sphere was calculated using the empirical relation that a nuclear explosion vaporizes 70 tons of material for each kiloton of explosion. The density of salt is 2200 kg/m^3, so the initial cavity radii are 1.97 W$^{1/3}$ meters where W is the yield in kilotons, and the initial energy density is 6.0x10^7 J/kg. The compressional velocity of the salt is 4550 m/s and the shear velocity is 2540 m/s. Each axisymmetric calculation used a grid spacing of one meter and grid dimensions of 500m horizontally and 1200m vertically. Symmetric explosions used just the upper half of the grid so that the vertical dimension was 600m. Calculations were run out to 0.1 seconds, just prior to the initial motion reaching the horizontal grid boundary. The initial and final cavity sizes for the Azgir1 calculation are shown in Figure 5. The cavity locations are determined by a sharp decrease in density.

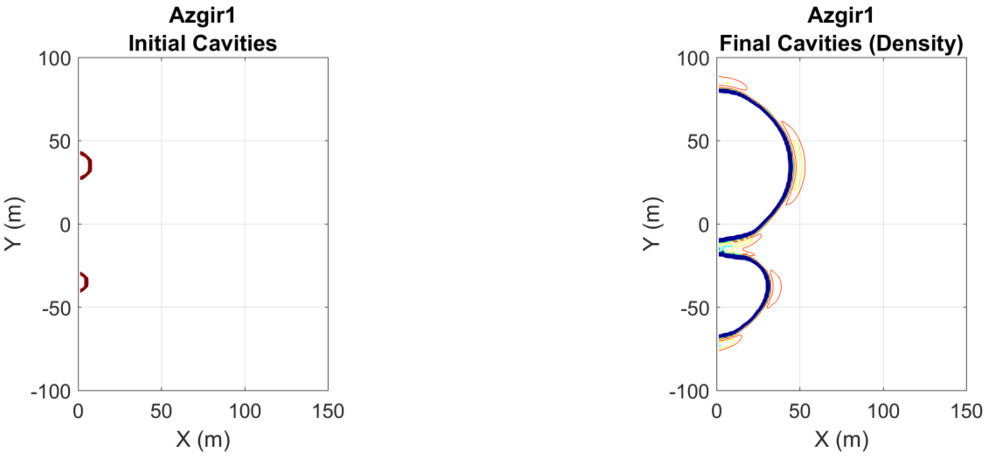

Figure 5. Initial (left) and final (right) cavity sizes for Azgir1 calculation.

We want to propagate the solution to points far from the explosion using the representation theorem. In these axisymmetric calculations, we save displacements and stresses due to the seismic source on a monitoring surface on a cylindrical boundary, and calculate Green's functions from each point on the monitoring surface to the receiver. We obtain the synthetic seismogram at the receiver point outside of the monitoring surface by integrating the Green's functions together with the stresses and displacements as discussed in section 3.2. The Green's functions in this case are whole space Green's functions calculated for a point source in an infinite salt medium.

To do this, we need to propagate the solution through a monitoring surface from the first motion until all motion has ceased. We rezone the calculation to a larger grid (Figure 6) that extends to 2000 meters in direction from the origin. The calculation is then run to 0.75 seconds which allows the motion from the calculation to propagate through the monitoring surface, and ending just prior to the time any spurious reflections from the surface would propagate to the monitoring surface.

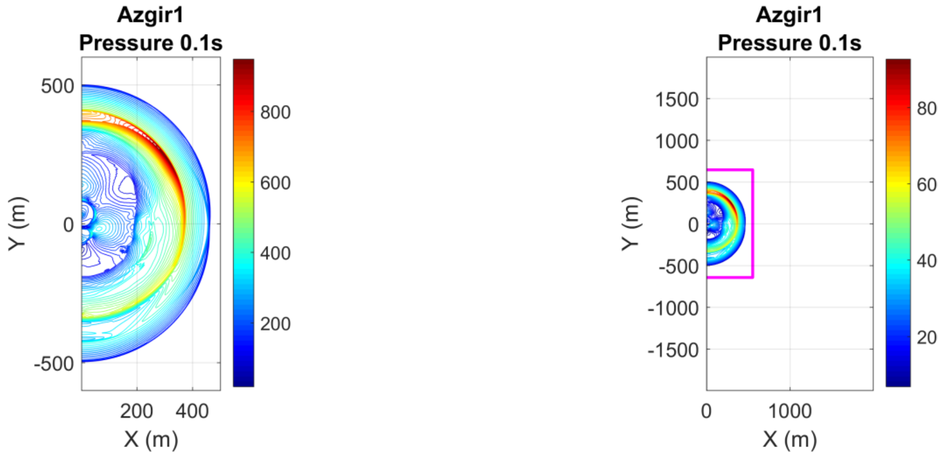

Figure 6. The calculation is rezoned to a larger grid at 0.1 seconds and run to 0.75 seconds, with displacements and stresses saved on the monitoring surface shown in the rezoned figure on the right. Left figure shows the pressure field prior to rezone.

In the following sections, we show results for calculations of all of the explosions listed in Table 1. For each multiple explosion, and for each equivalent single explosion, we show the P waves at 1 degree (almost vertical in Figure 6) and 89 degree (almost horizontal in Figure 6) take-off angles. These are far-field P-waves in an infinite uniform medium, normalized to a distance of one meter. We use these angles to avoid some numerical problems that occur at exactly 0 and 90 degrees. We also show P waves and SV waves at 45 degrees, the spectra of each of these waveforms, and the average ratio of multiple explosion spectra to single explosion spectra (the low amplitude SV from the single explosion is numerical noise).

In each case we find one very consistent result: at long periods, yield dependent but less than a few Hz for all calculations, the single and multiple explosion spectra are identical. This means that if yields are estimated from body waves in the normal frequency range of about 1 Hz, accurate total yields will be obtained from multiple explosions. However, at higher frequencies the waveforms from the individual explosions start to separate and there are differences between the single explosion and multiple explosion waveforms and spectra. Figure 7 shows an example from the Rio Blanco calculation, three 33 kiloton explosions each separated by 126m. Here the 3 explosions are clearly seen in the vertical direction, but not in the horizontal.

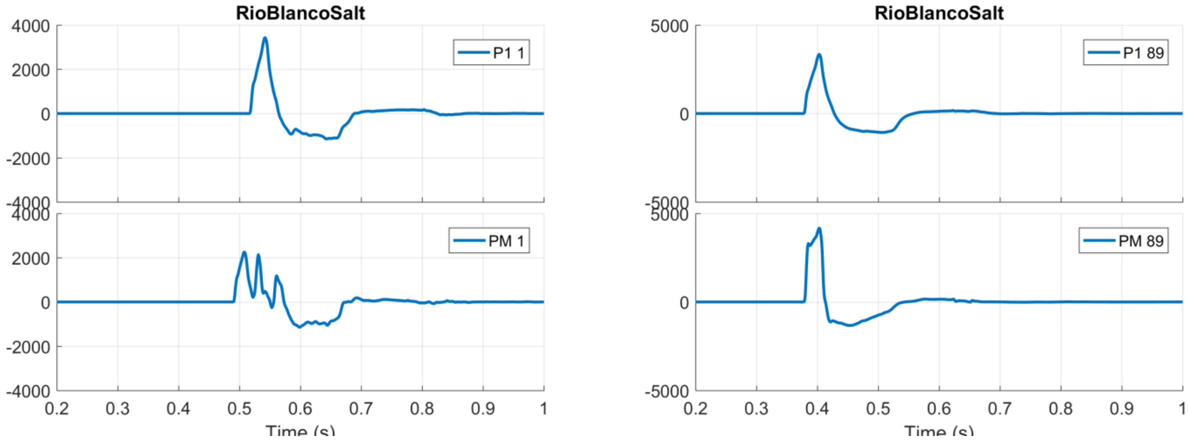

Figure 7. Waveforms from Rio Blanco calculation. *Top row: P waves at 1 and 89 degrees from single event calculation. Bottom row: P waves from multiple (triple) event calculation.*

Similarly, as shown in Figure 8, there are differences in spectra at high frequencies, with multiple explosion spectra generally smaller than the single explosion in the vertical direction and larger in the horizontal direction above about 5 Hz.

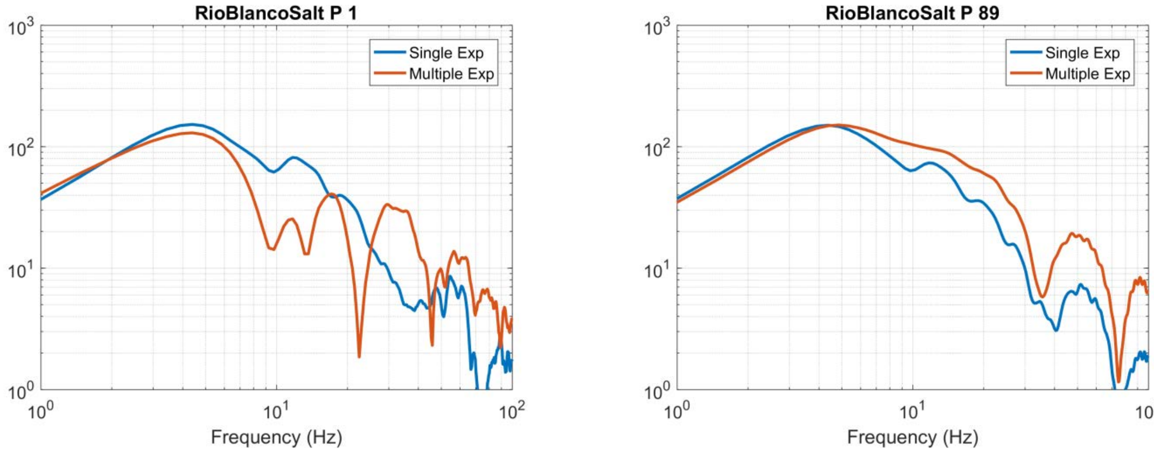

Figure 8. Spectra for the waveforms shown above.

4.1.1 Azgir 1: 1978/10/17

18 kiloton at 1040m depth + 56 kiloton at 970m depth.

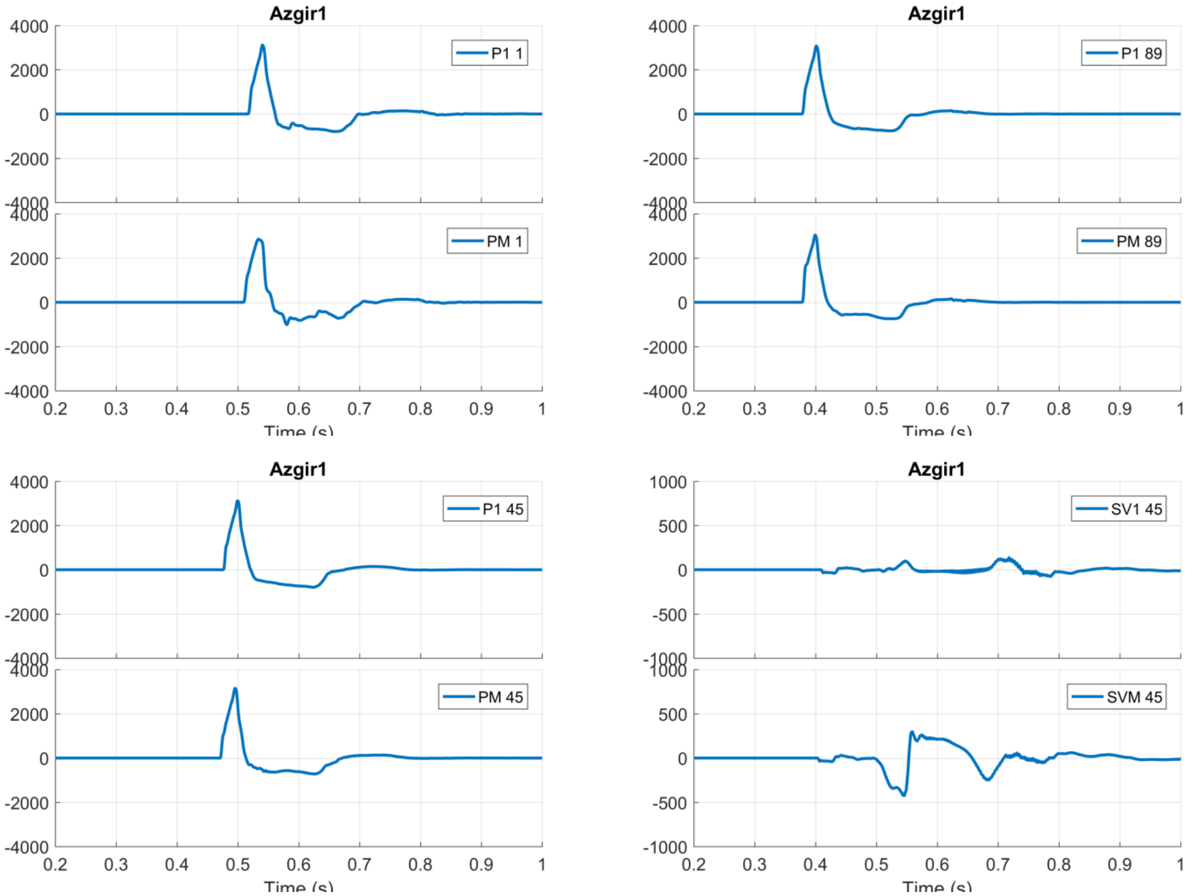

Figure 9. Waveforms from Azgir 1 calculation. ***Top row: P waves at 1 and 89 degrees. Bottom row: P and SV waves at 45 degrees. P1 corresponds to a single explosion with the same total yield. PM to the multiple explosion. SV from the single explosion is just numerical noise.***

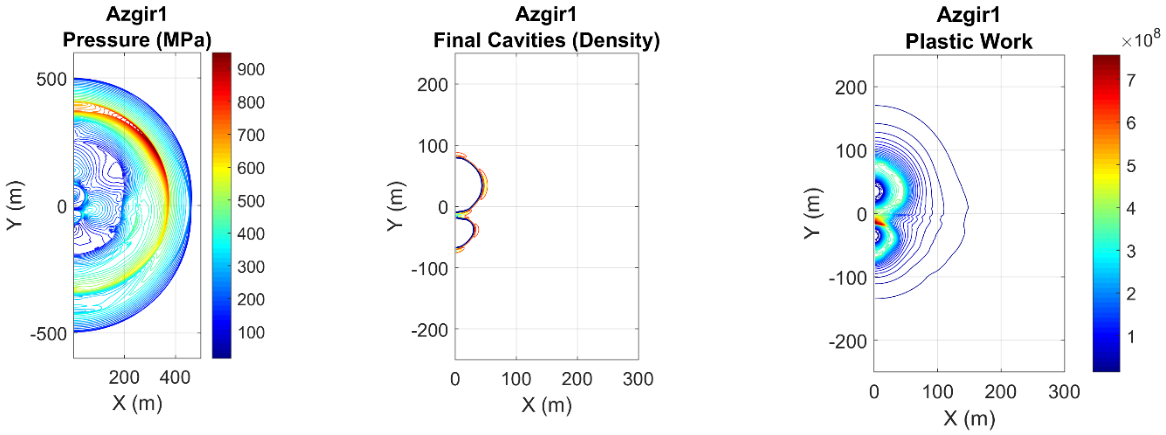

Figure 10. Left: Azgir 1 pressure at 0.1 seconds. Middle: Final cavity shapes (contours of density). Right: Plastic work.

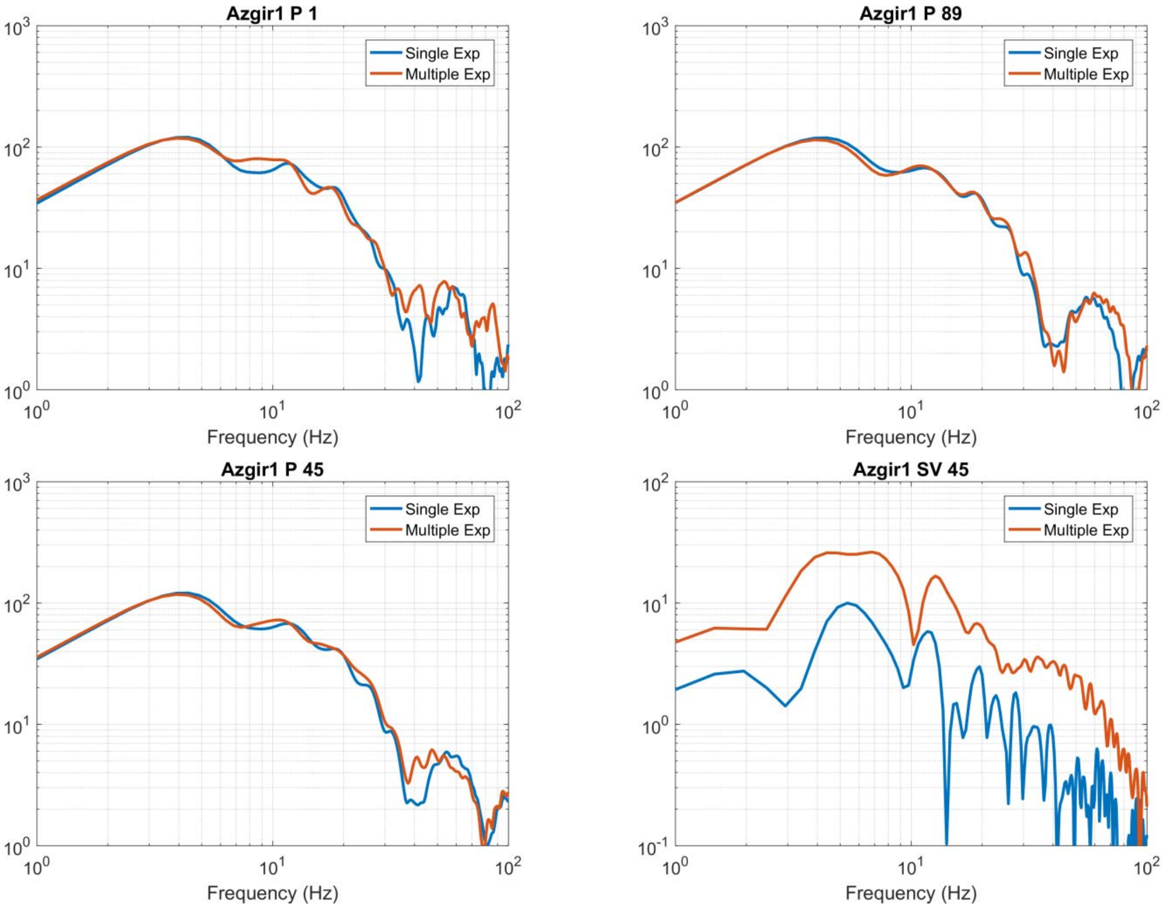

Figure 11. Spectra for the waveforms shown above.

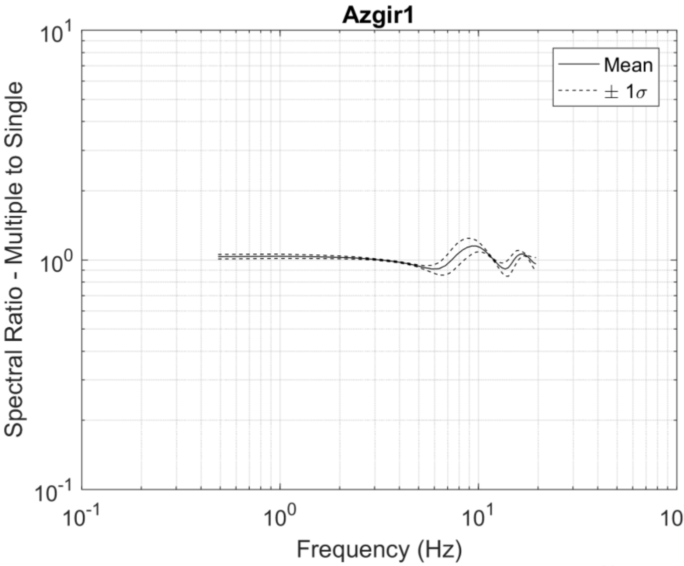

Figure 12. Ratio of multiple to single explosion averaged over all takeoff angles shown together with ±1 standard deviation.

4.1.2 Azgir 2: 1979/01/17

12.5 kiloton at 995m depth plus 56 kiloton at 934m depth

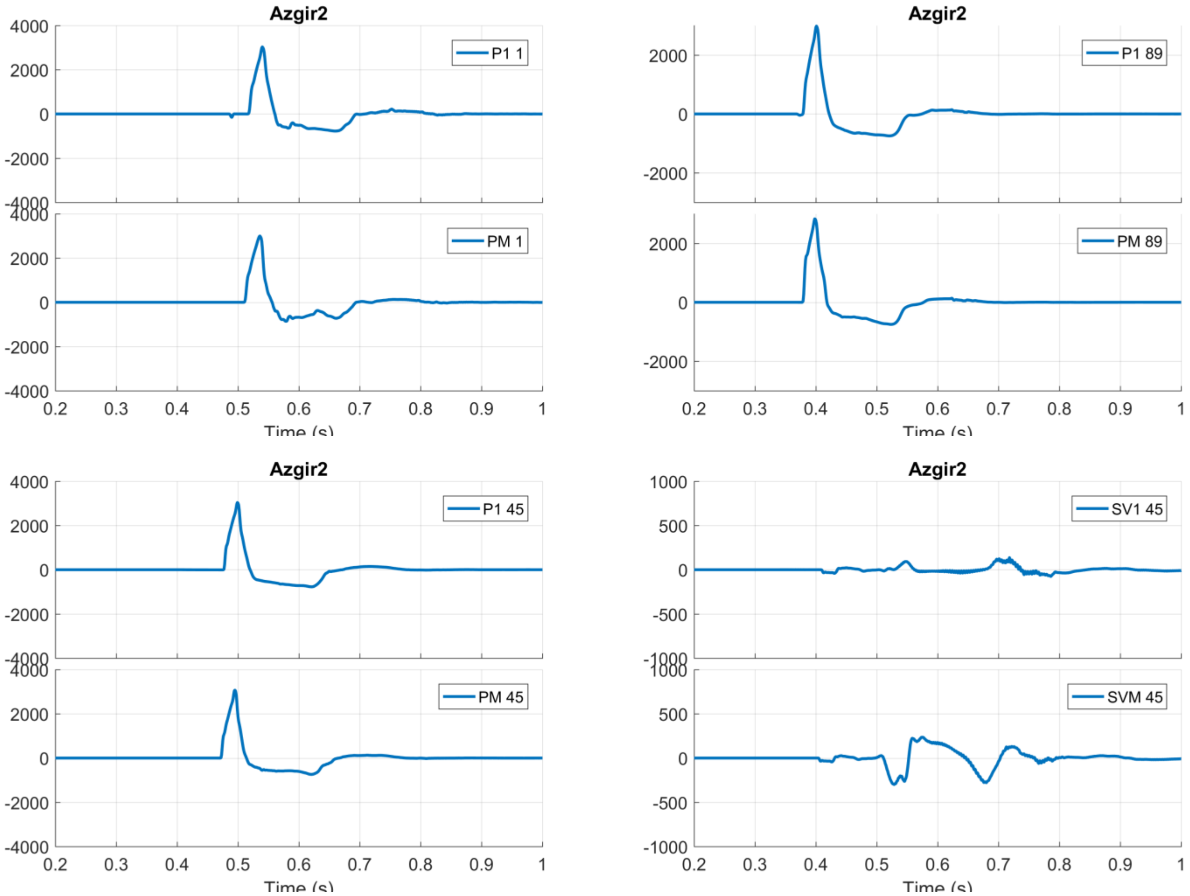

Figure 13. Waveforms from Azgir 2 calculation. ***Top row: P waves at 1 and 89 degrees. Bottom row: P and SV waves at 45 degrees. P1 corresponds to a single explosion with the same total yield. PM to the multiple explosion.***

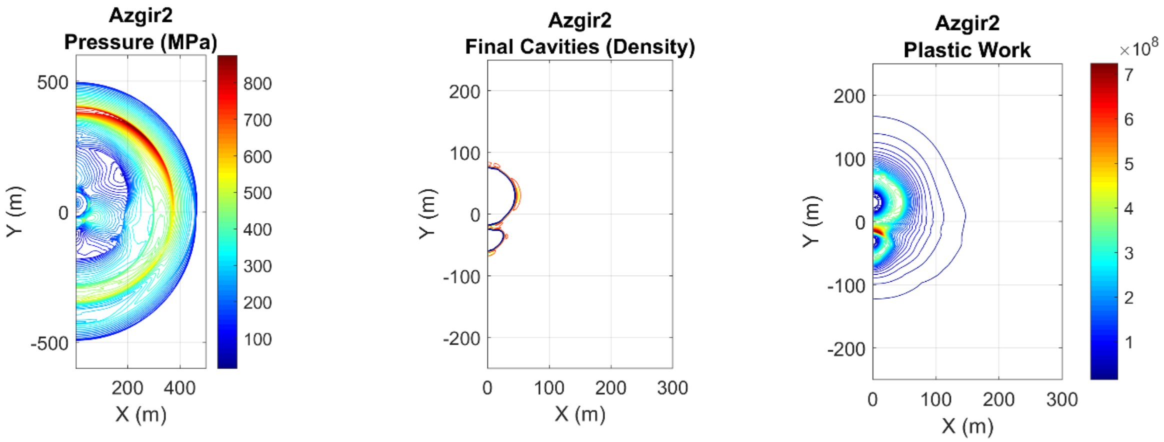

Figure 14. Left: Azgir 2 pressure at 0.1 seconds. Middle: Final cavity shapes (contours of density). Right: Plastic work.

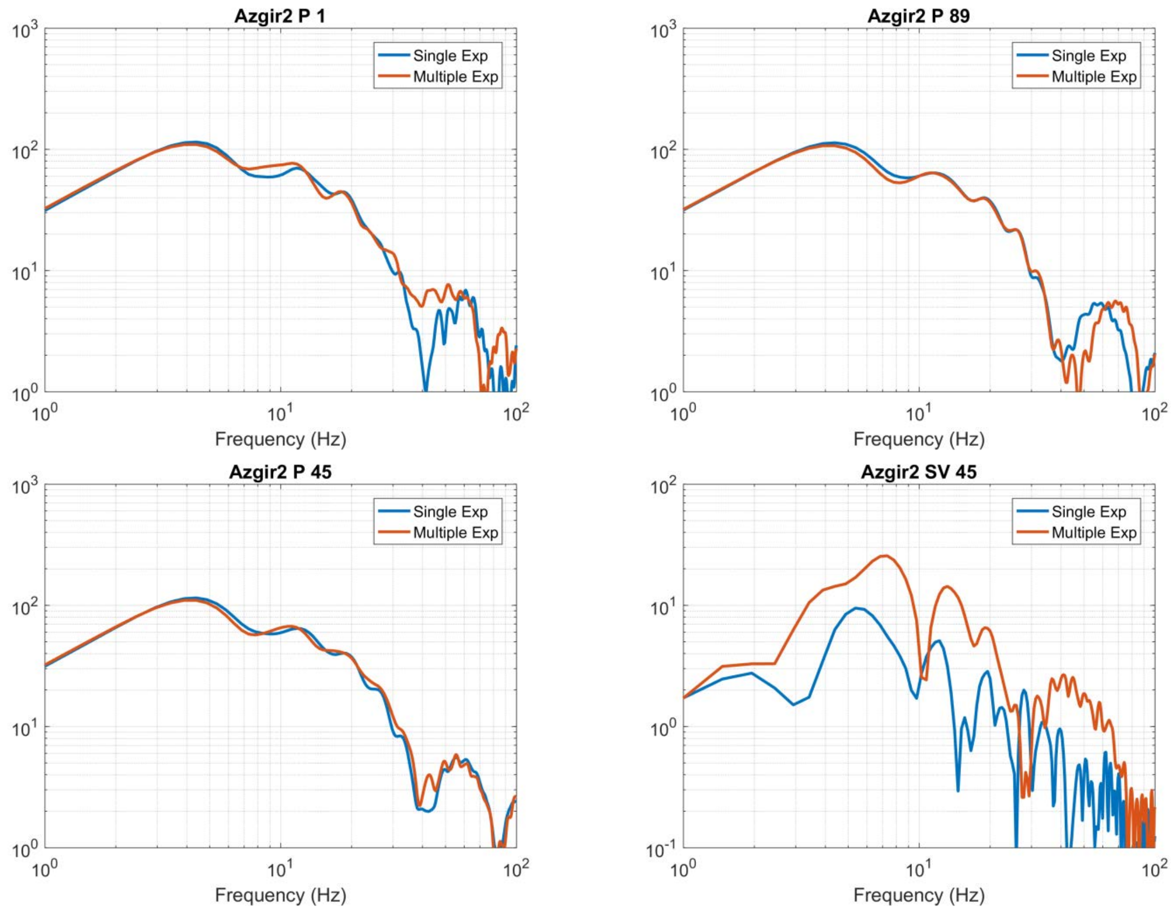

Figure 15. Spectra for the waveforms shown above.

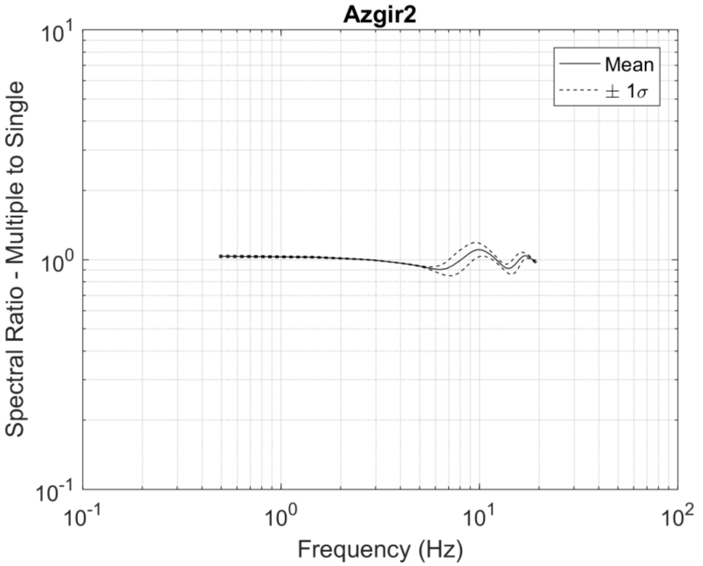

Figure 16. Ratio of multiple to single explosion averaged over all takeoff angles shown together with ±1 standard deviation.

4.1.3 Azgir 3: 1979/07/14

Three 7 kiloton explosions at 916±66m depth

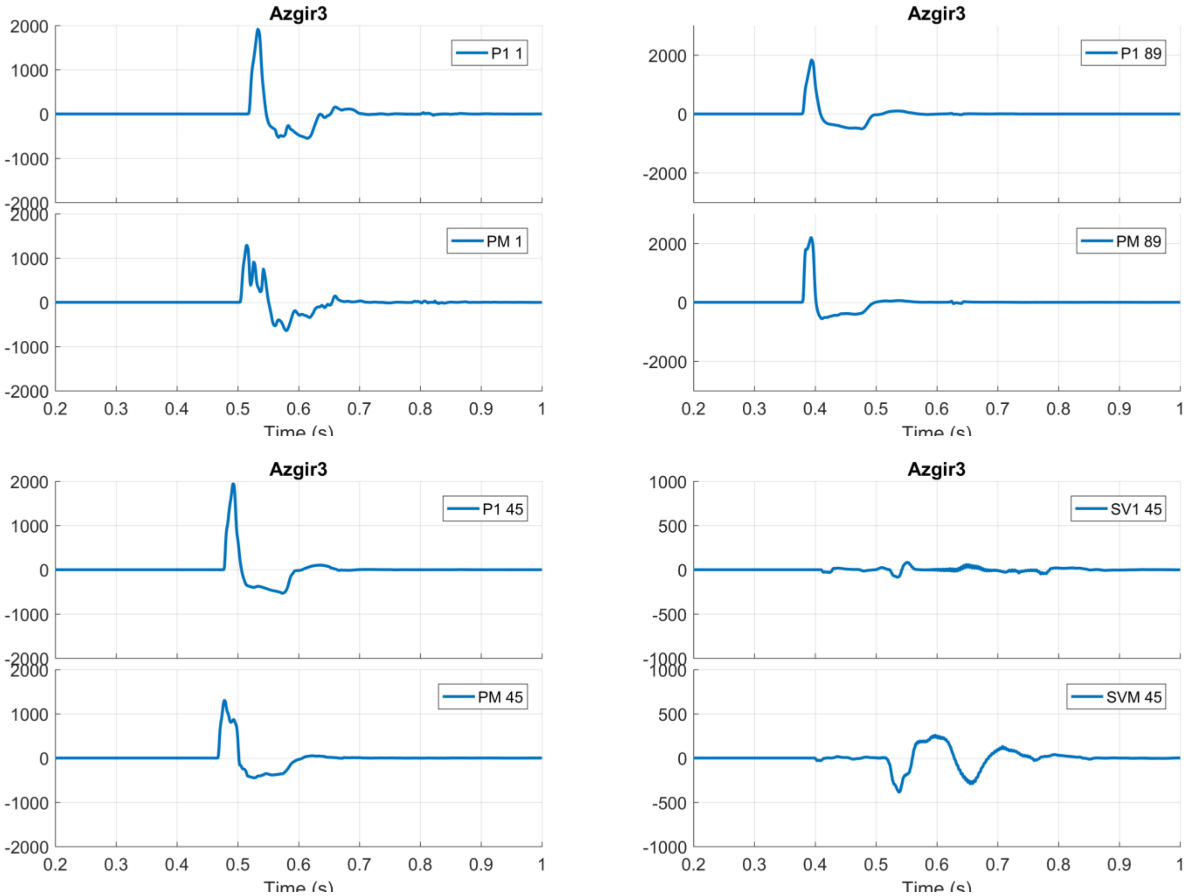

Figure 17. Waveforms from Azgir 3 calculation. ***Top row: P waves at 1 and 89 degrees. Bottom row: P and SV waves at 45 degrees. P1 corresponds to a single explosion with the same total yield. PM to the multiple explosion.***

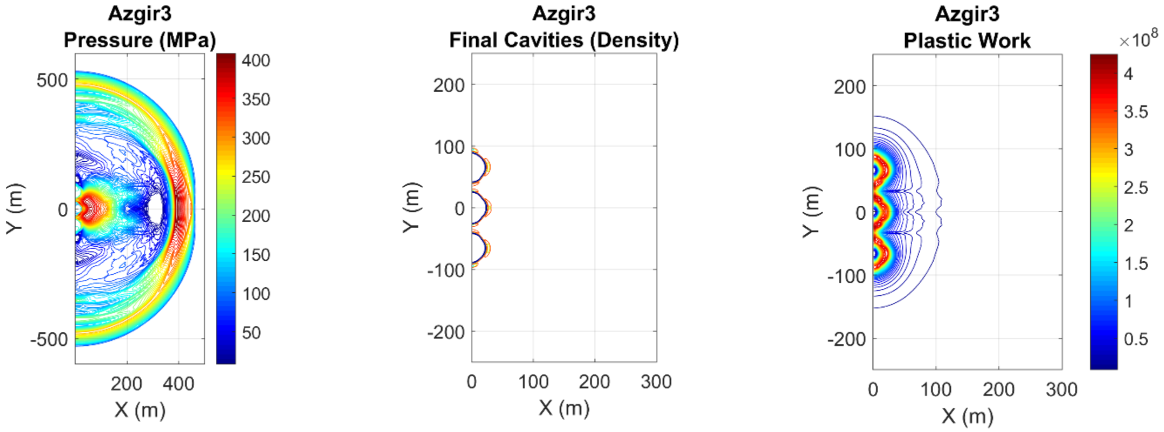

Figure 18. Left: Azgir 3 pressure at 0.1 seconds. Middle: Final cavity shapes (contours of density). Right: Plastic work.

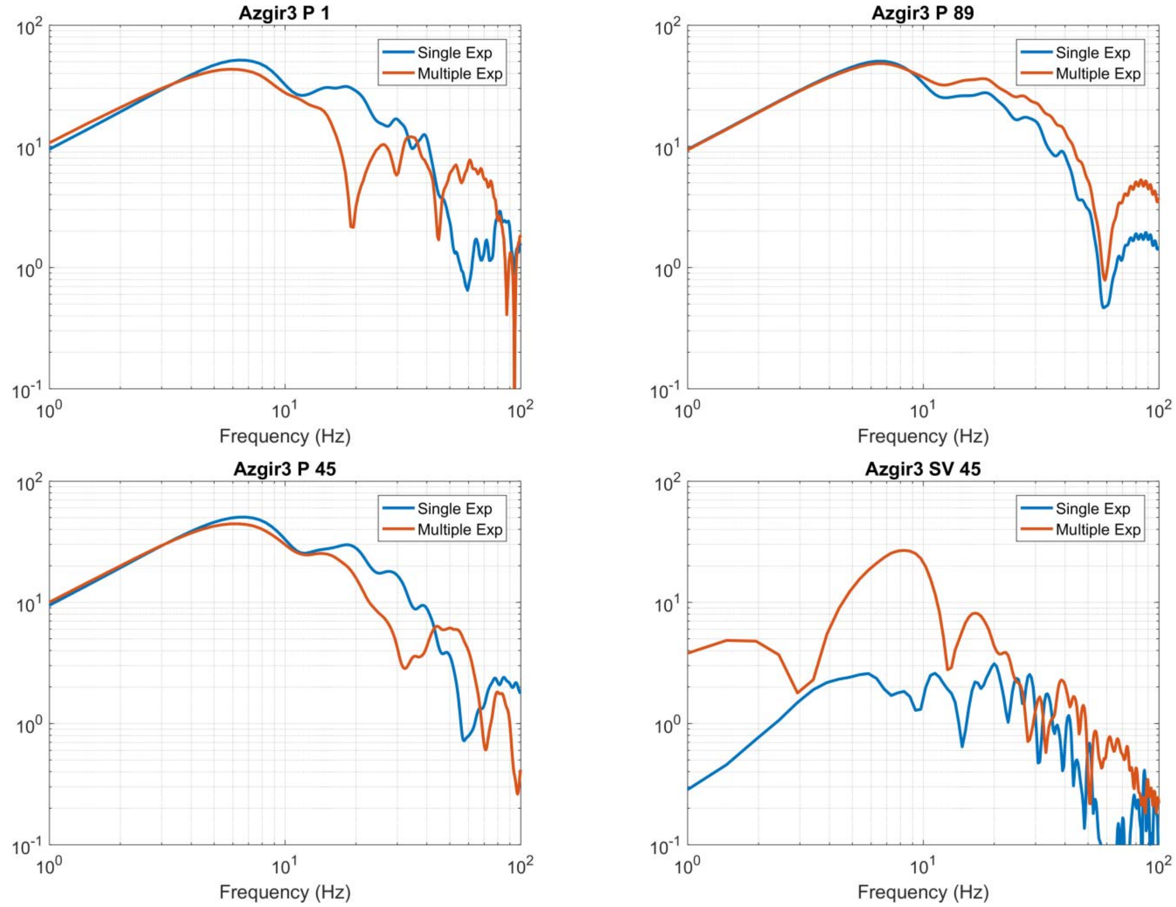

Figure 19. Spectra for the waveforms shown above.

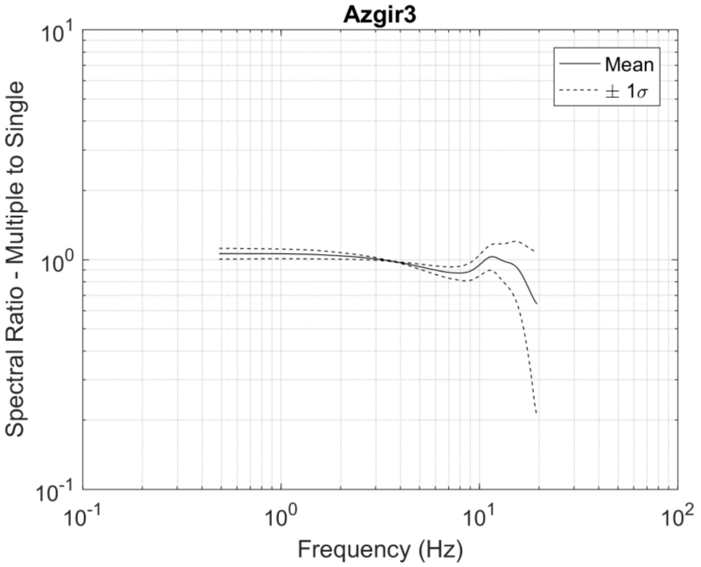

Figure 20. Ratio of multiple to single explosion averaged over all takeoff angles shown together with ±1 standard deviation.

4.1.4 Azgir 10: 1979/10/24

Two 16.5 kiloton at 915 and 980 meters depth

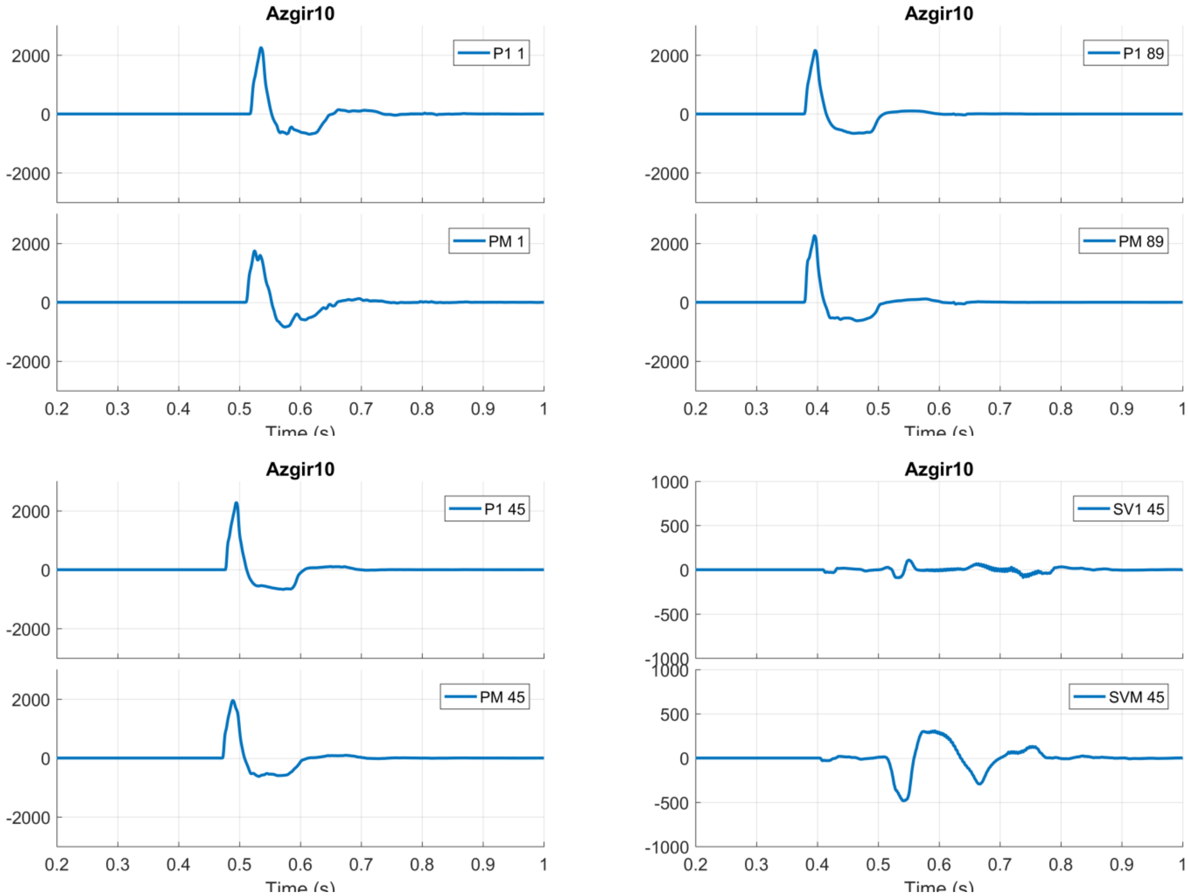

Figure 21. Waveforms from Azgir 10 calculation. ***Top row: P waves at 1 and 89 degrees. Bottom row: P and SV waves at 45 degrees. P1 corresponds to a single explosion with the same total yield. PM to the multiple explosion.***

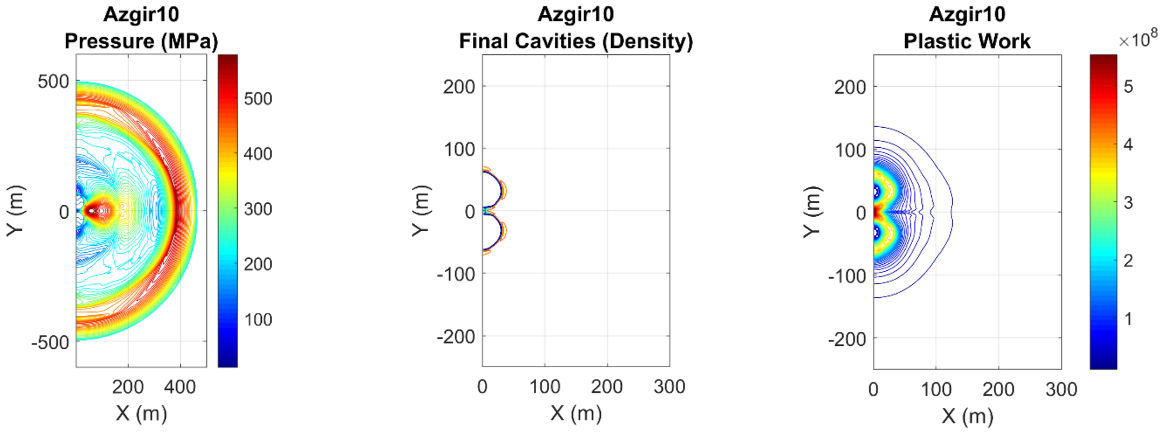

Figure 22. Left: Azgir 10 pressure at 0.1 seconds. Middle: Final cavity shapes (contours of density). Right: Plastic work.

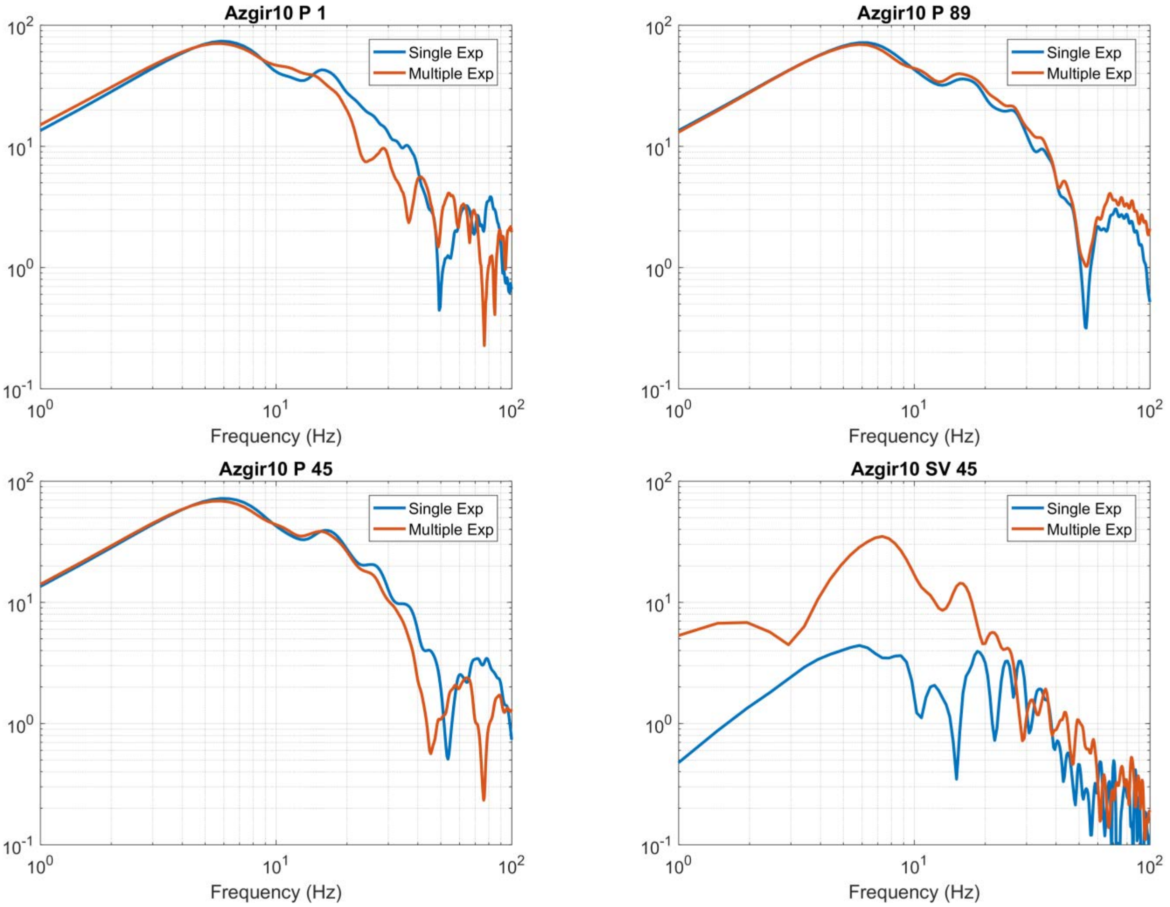

Figure 23. Spectra for the waveforms shown above.

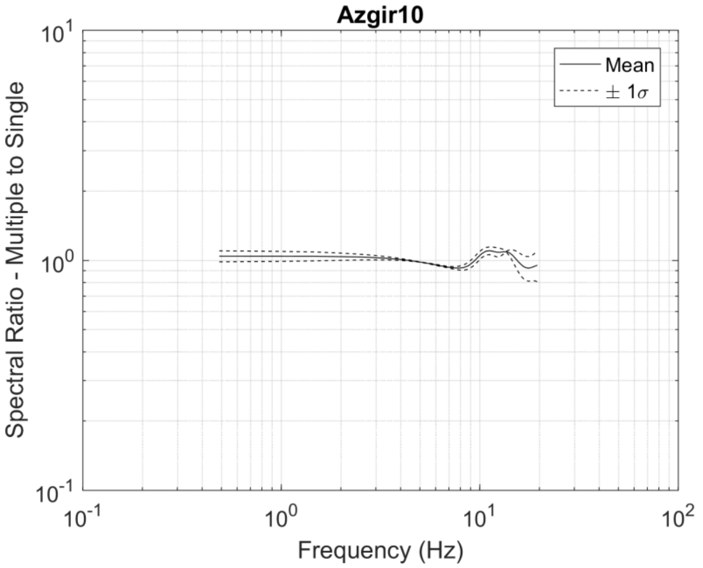

Figure 24. Ratio of multiple to single explosion averaged over all takeoff angles shown together with ±1 standard deviation.

4.1.5 Butane 1: 1965/03/30

Two 2.3 kt explosions, 200 meters apart, 1341 and 1375m depth.

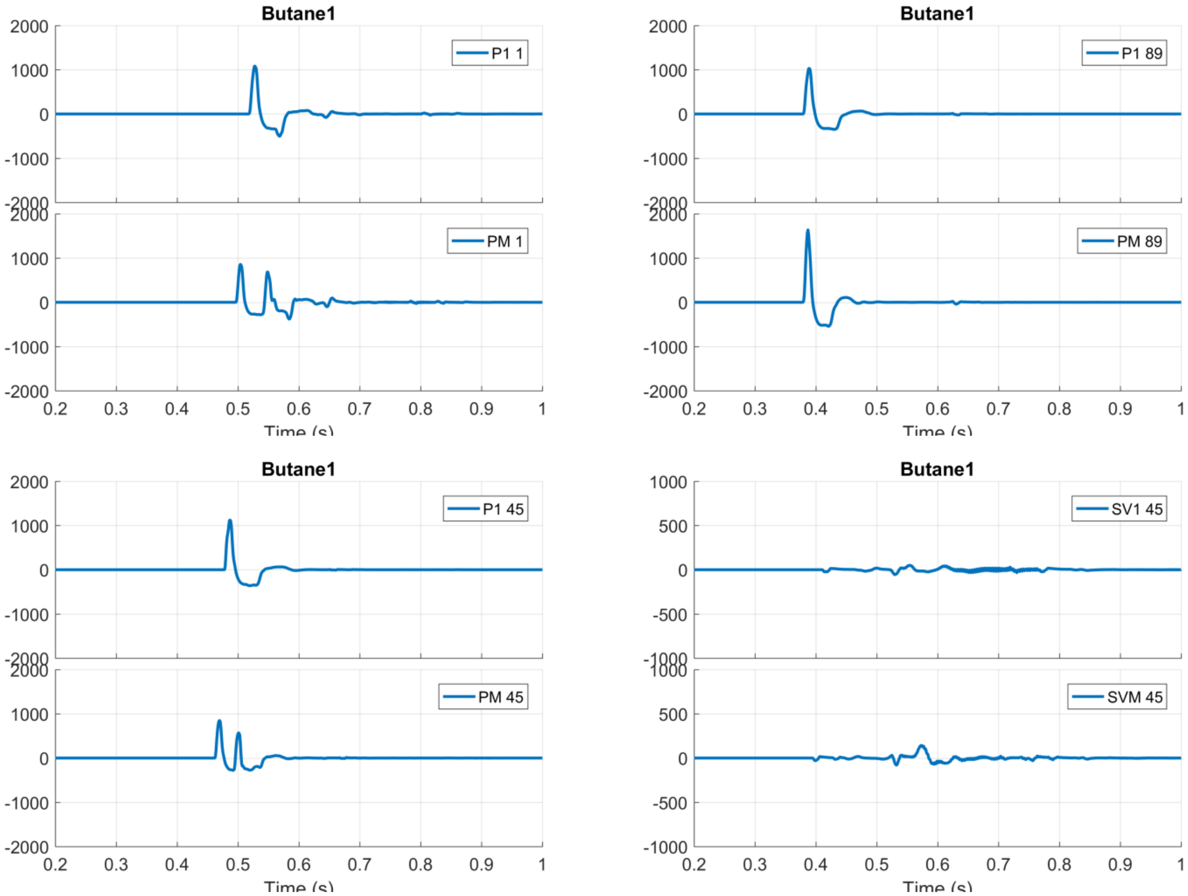

Figure 25. Waveforms from Butane 1 calculation. ***Top row: P waves at 1 and 89 degrees. Bottom row: P and SV waves at 45 degrees. P1 corresponds to a single explosion with the same total yield. PM to the multiple explosion.***

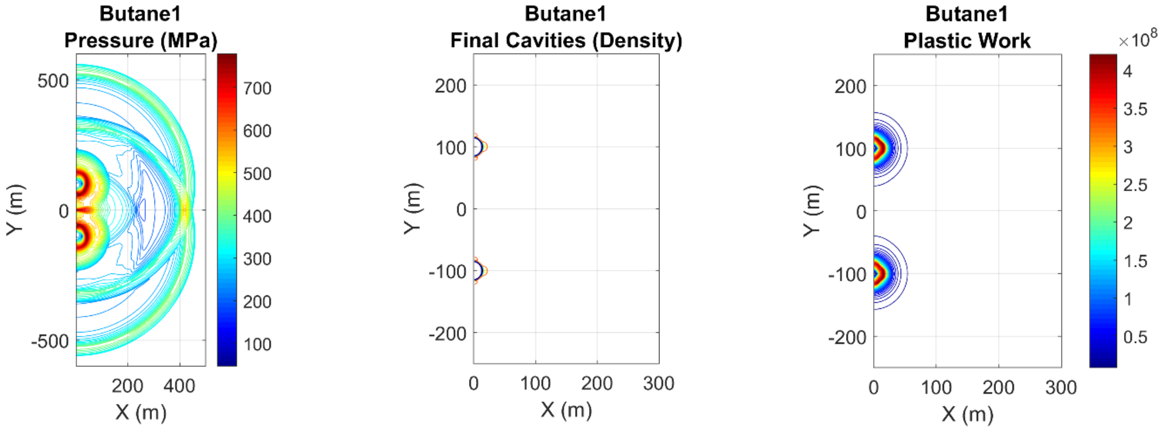

Figure 26. Left: Butane 1 pressure at 0.1 seconds. Middle: Final cavity shapes (contours of density). Right: Plastic work.

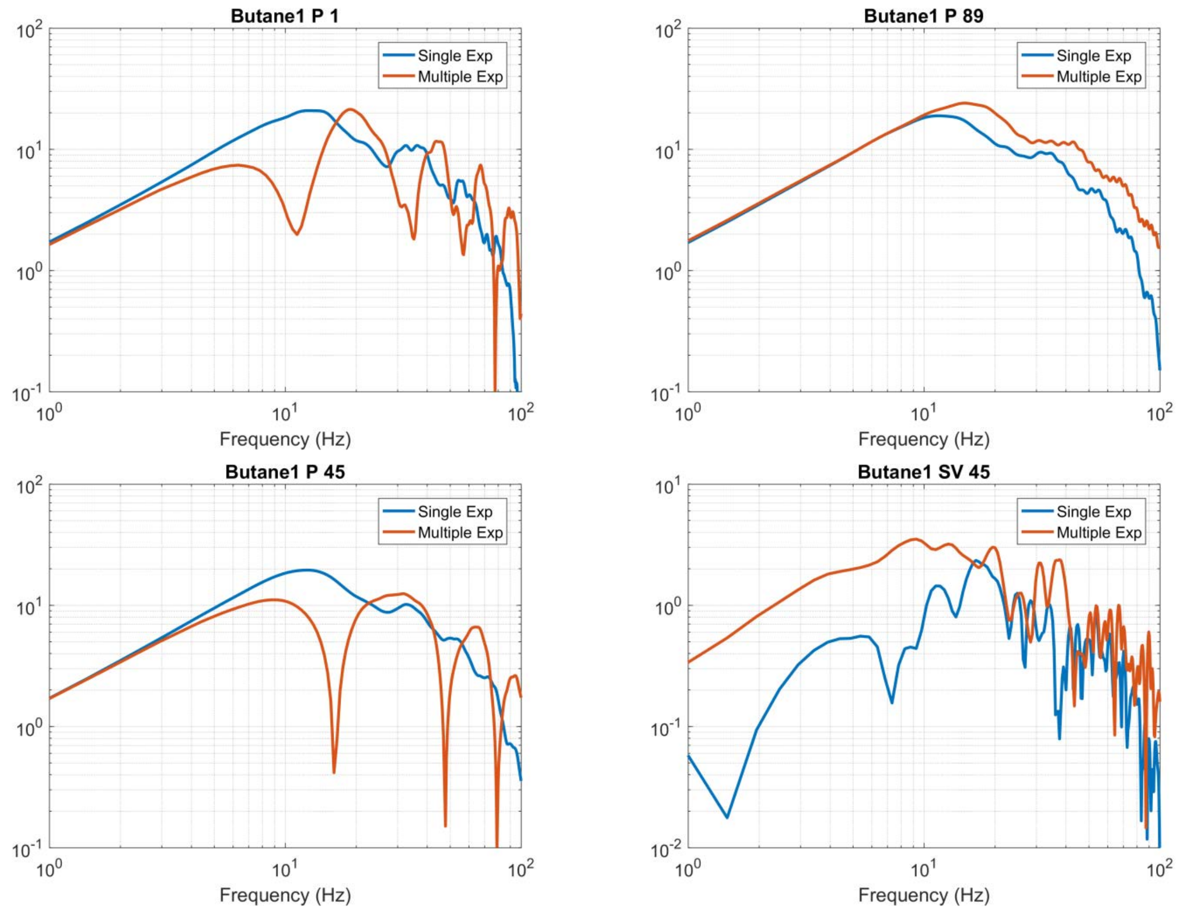

Figure 27. Spectra for the waveforms shown above.

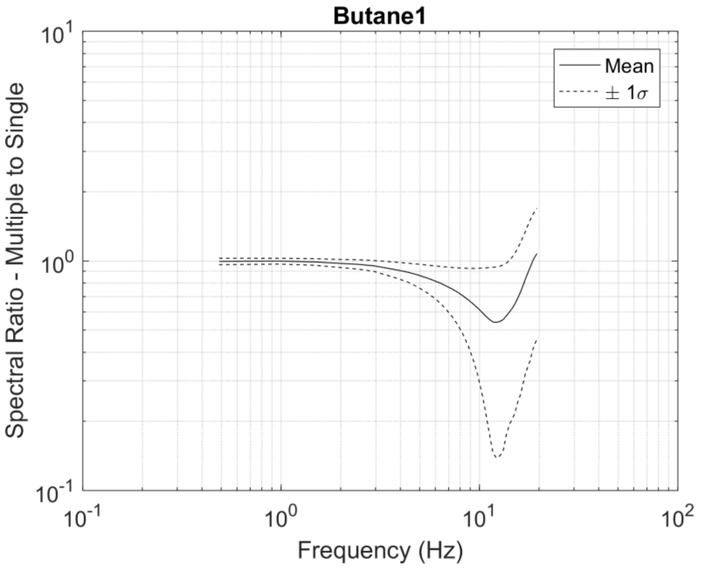

Figure 28. Ratio of multiple to single explosion averaged over all takeoff angles shown together with ±1 standard deviation.

4.1.6 Dnepr 2: 1984/08/27

Two 1.7 kiloton at 175m depth, 75 m apart

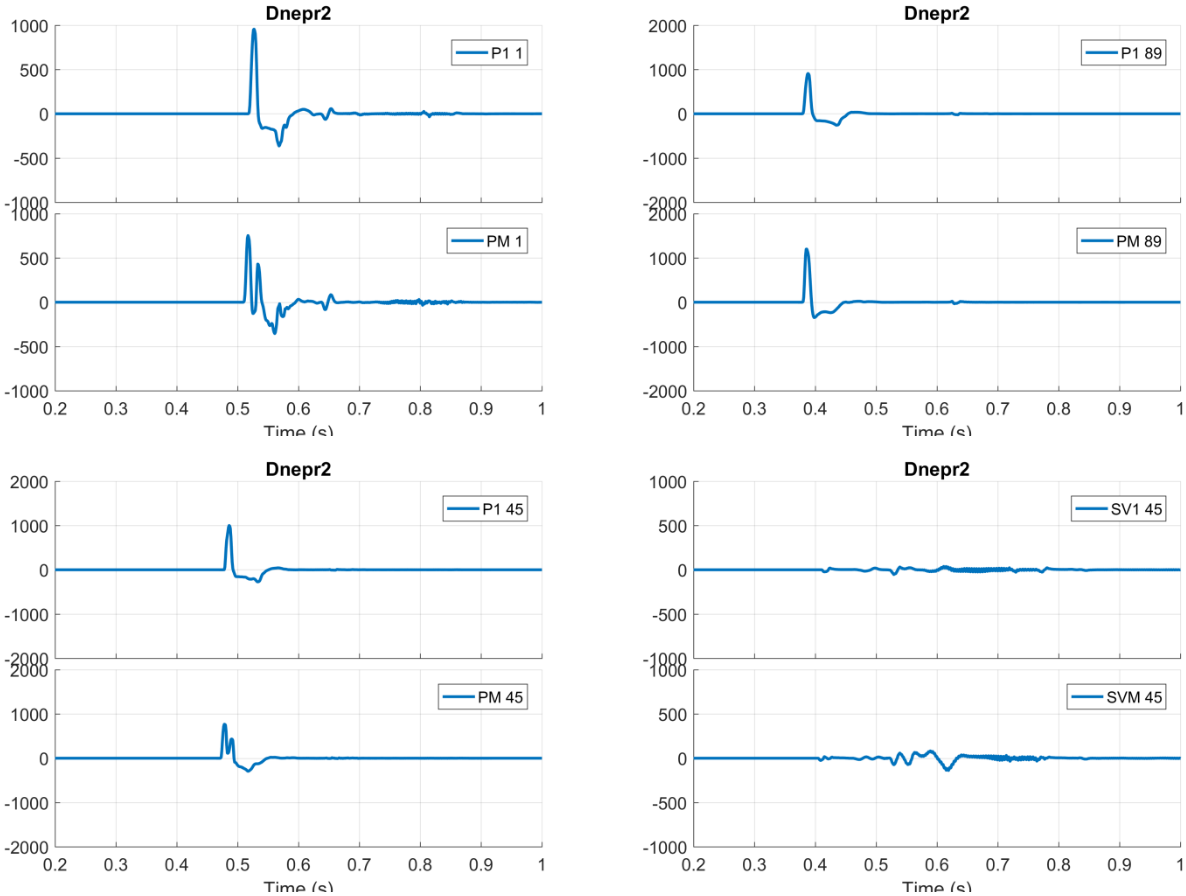

Figure 29. Waveforms from Dnepr2 calculation. ***Top row: P waves at 1 and 89 degrees. Bottom row: P and SV waves at 45 degrees. P1 corresponds to a single explosion with the same total yield. PM to the multiple explosion.***

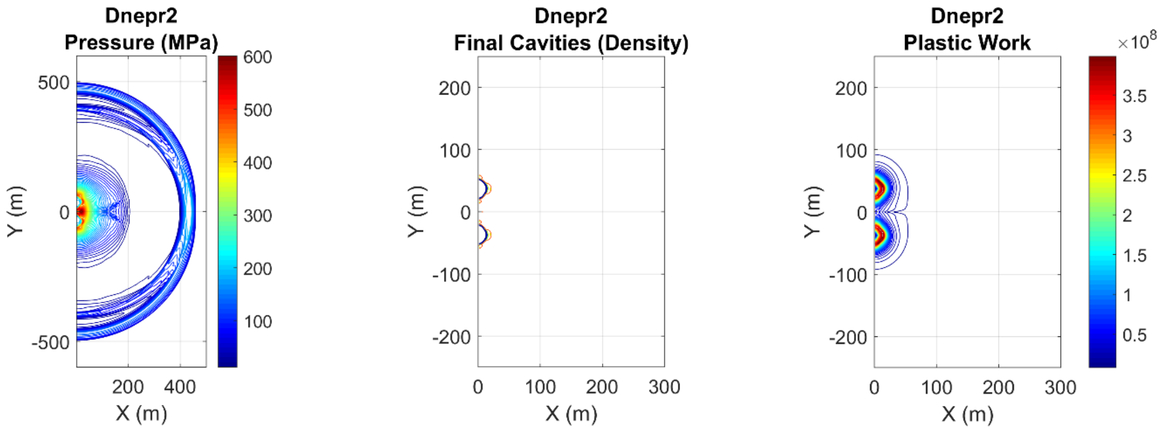

Figure 30. Left: Dnepr 2 pressure at 0.1 seconds. Middle: Final cavity shapes (contours of density). Right: Plastic work.

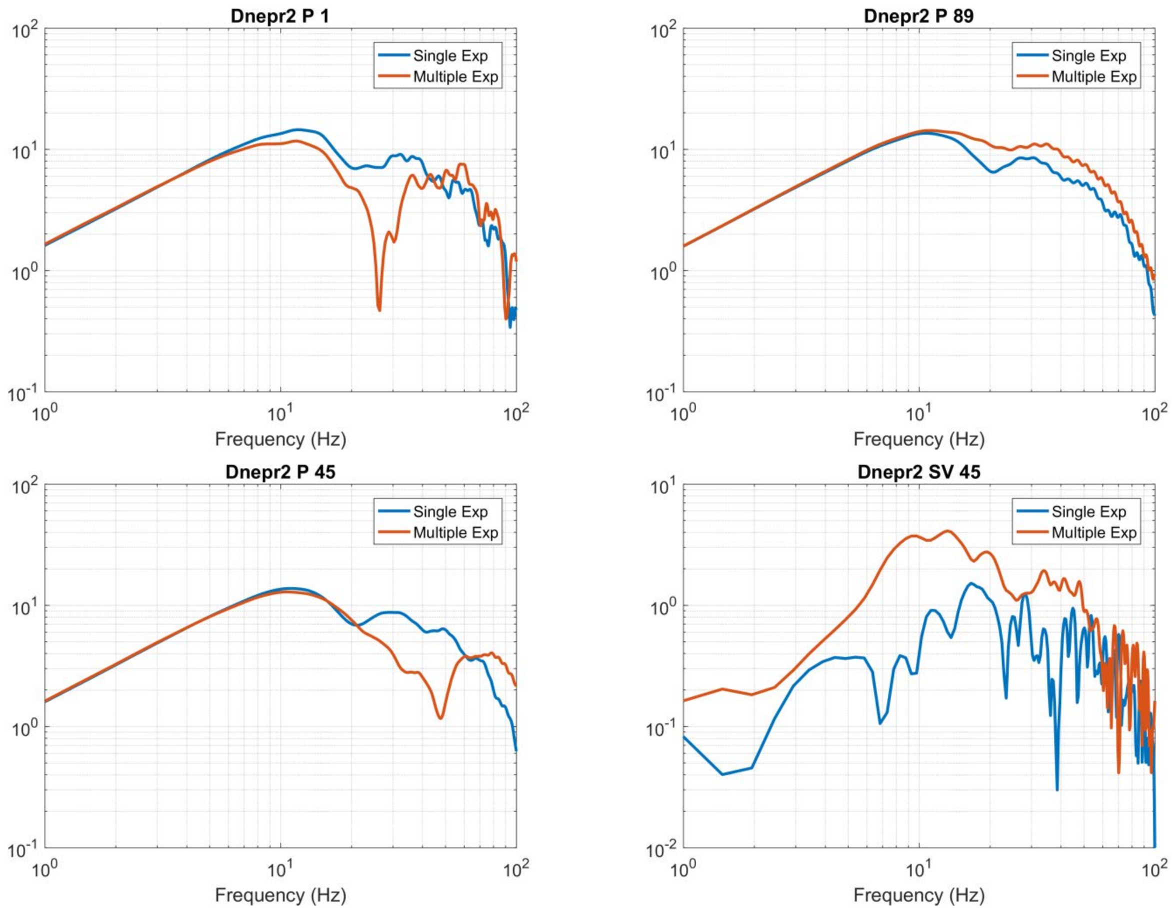

Figure 31. Spectra for the waveforms shown above.

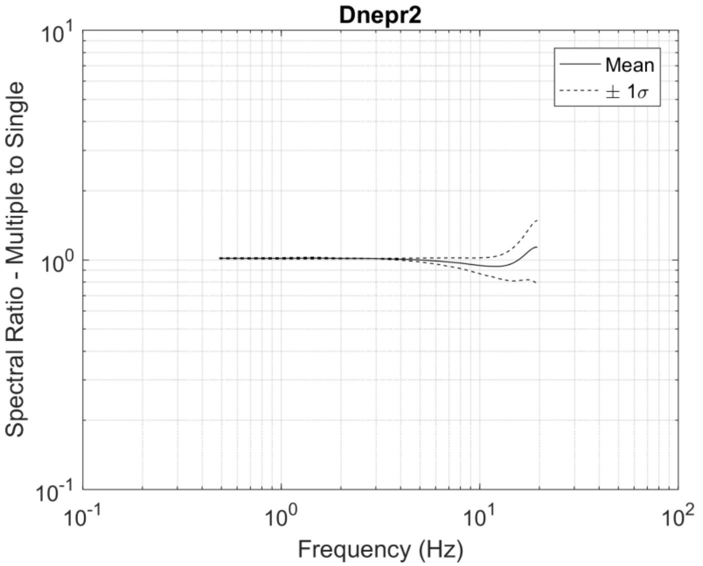

Figure 32. Ratio of multiple to single explosion averaged over all takeoff angles shown together with ±1 standard deviation.

4.1.7 Dnepr 1: 1972/09/04

Single explosion 2.1 kt at 131m depth in the same mine as Dnepr 2. Multiple explosion is Dnepr2.

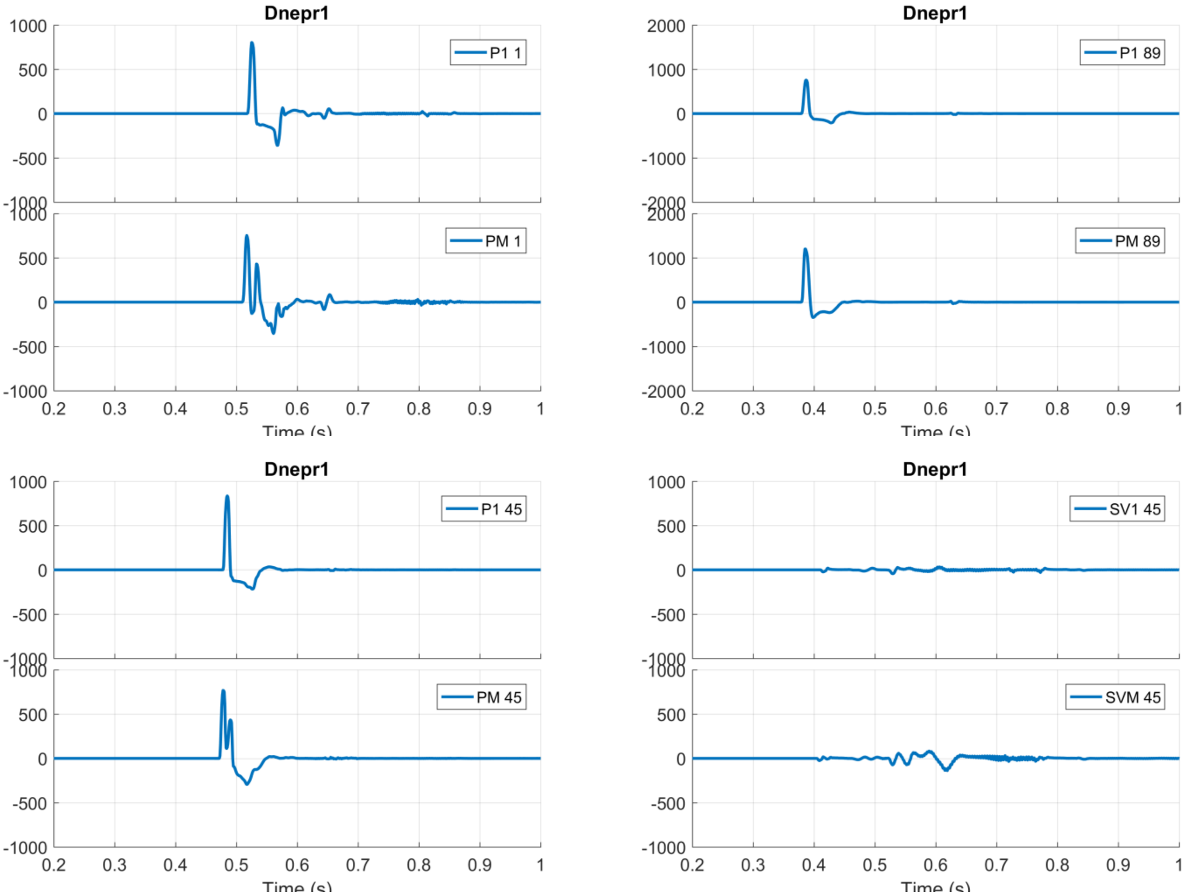

Figure 33. Waveforms from Dnepr1 calculation (single) and Dnepr2 calculation (multiple). ***Top row: P waves at 1 and 89 degrees. Bottom row: P and SV waves at 45 degrees. P1 corresponds to the Dnepr1 single explosion; PM to the Dnepr2 multiple explosion.***

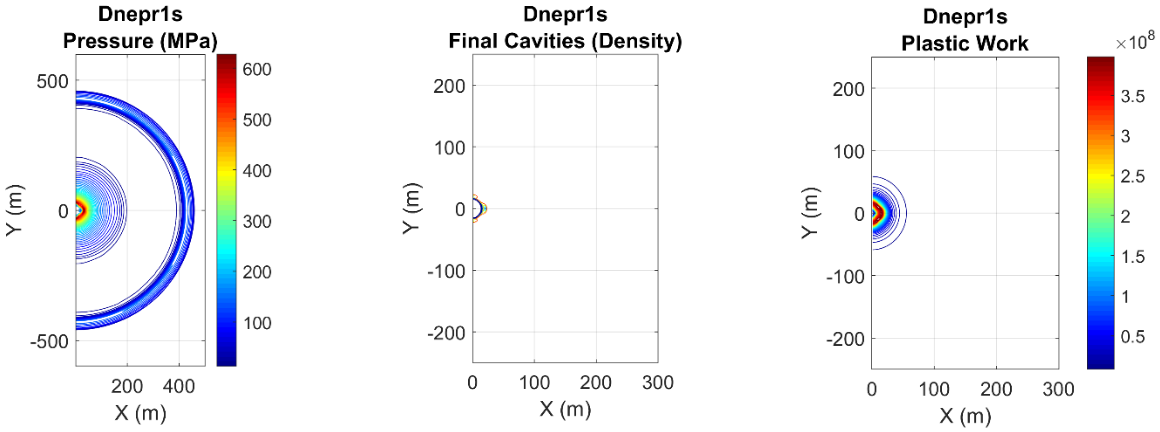

Figure 34. Left: Dnepr 1 pressure at 0.1 seconds. Middle: Final cavity shapes (contours of density). Right: Plastic work.

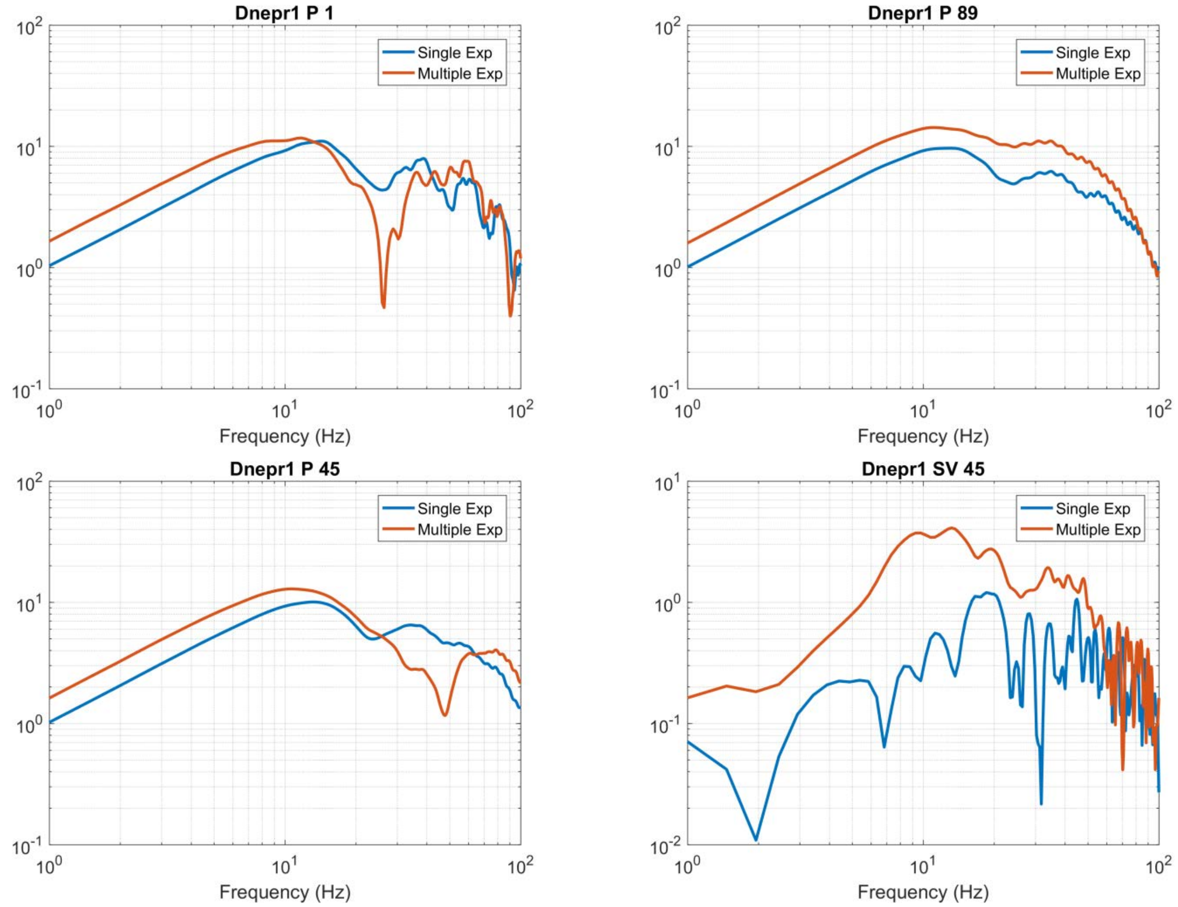

Figure 35. Spectra for the waveforms shown above.

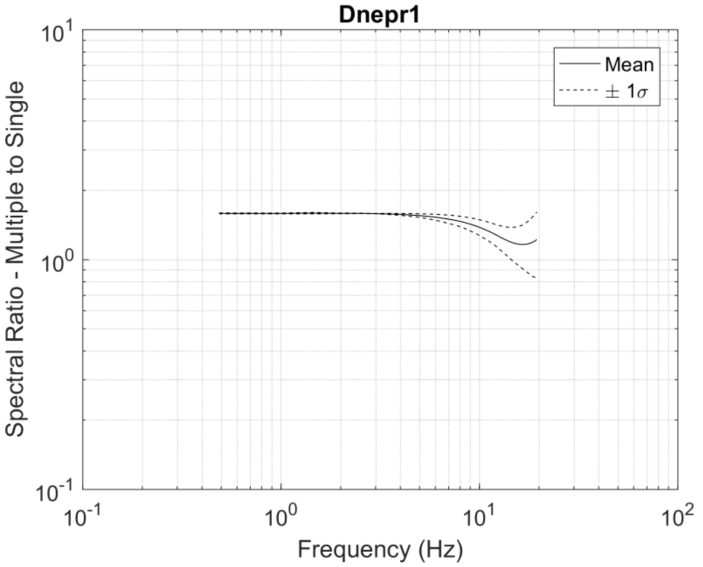

Figure 36. Ratio of Dnepr2 multiple explosion to Dnepr1 single explosion averaged over all takeoff angles shown together with ±1 standard deviation.

4.1.8 Rio Blanco: 1973/05/17

Three 33 kiloton at depths of 1900±126m.

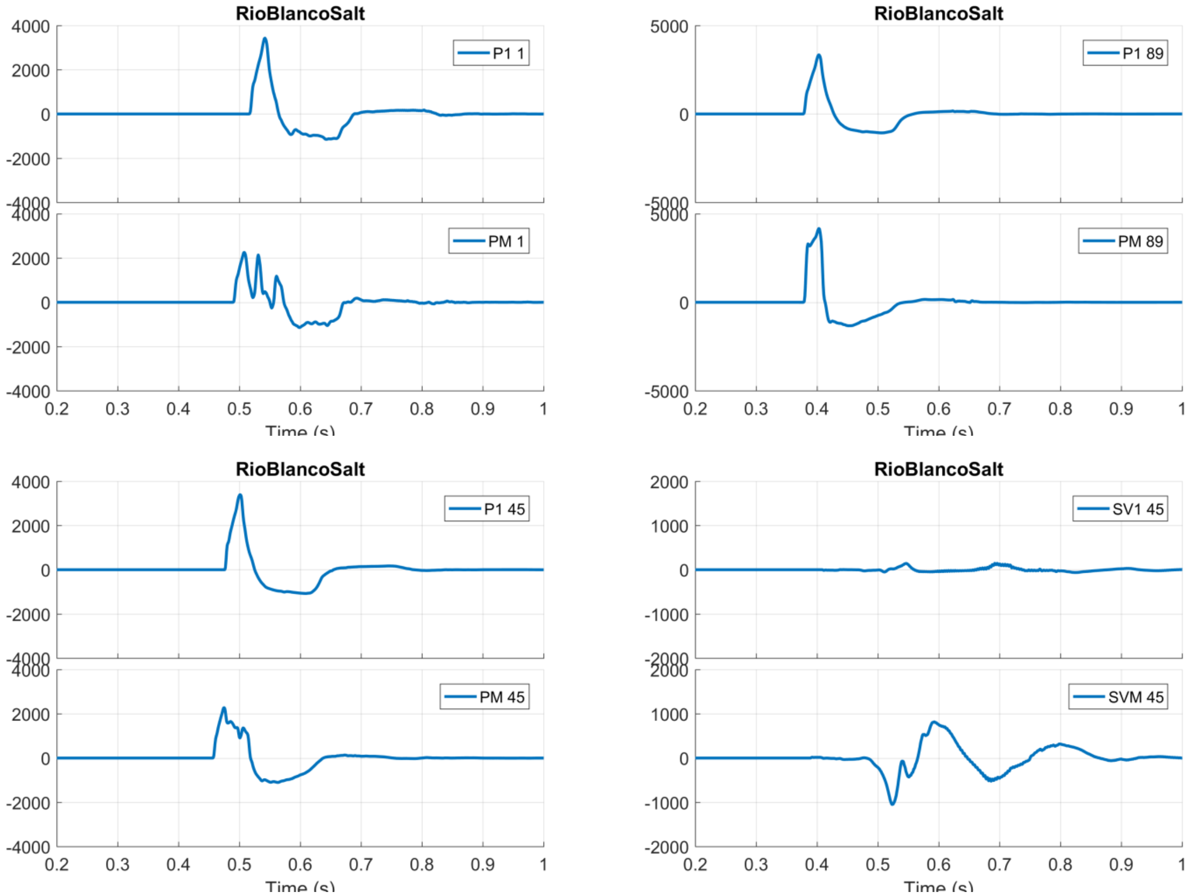

Figure 37. Waveforms from Rio Blanco calculation. ***Top row: P waves at 1 and 89 degrees. Bottom row: P and SV waves at 45 degrees. P1 corresponds to a single explosion with the same total yield. PM to the multiple explosion.***

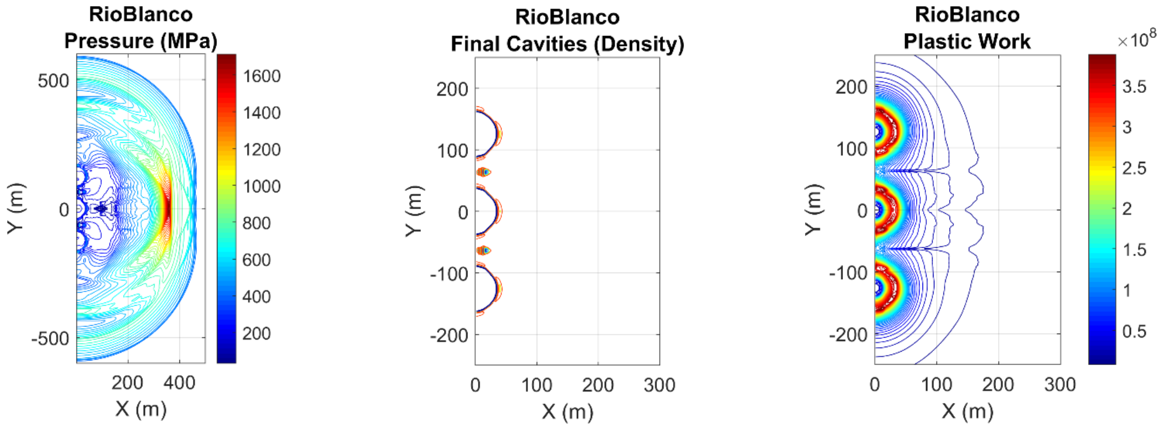

Figure 38. Left: Rio Blanco pressure at 0.1 seconds. Middle: Final cavity shapes (contours of density). Right: Plastic work.

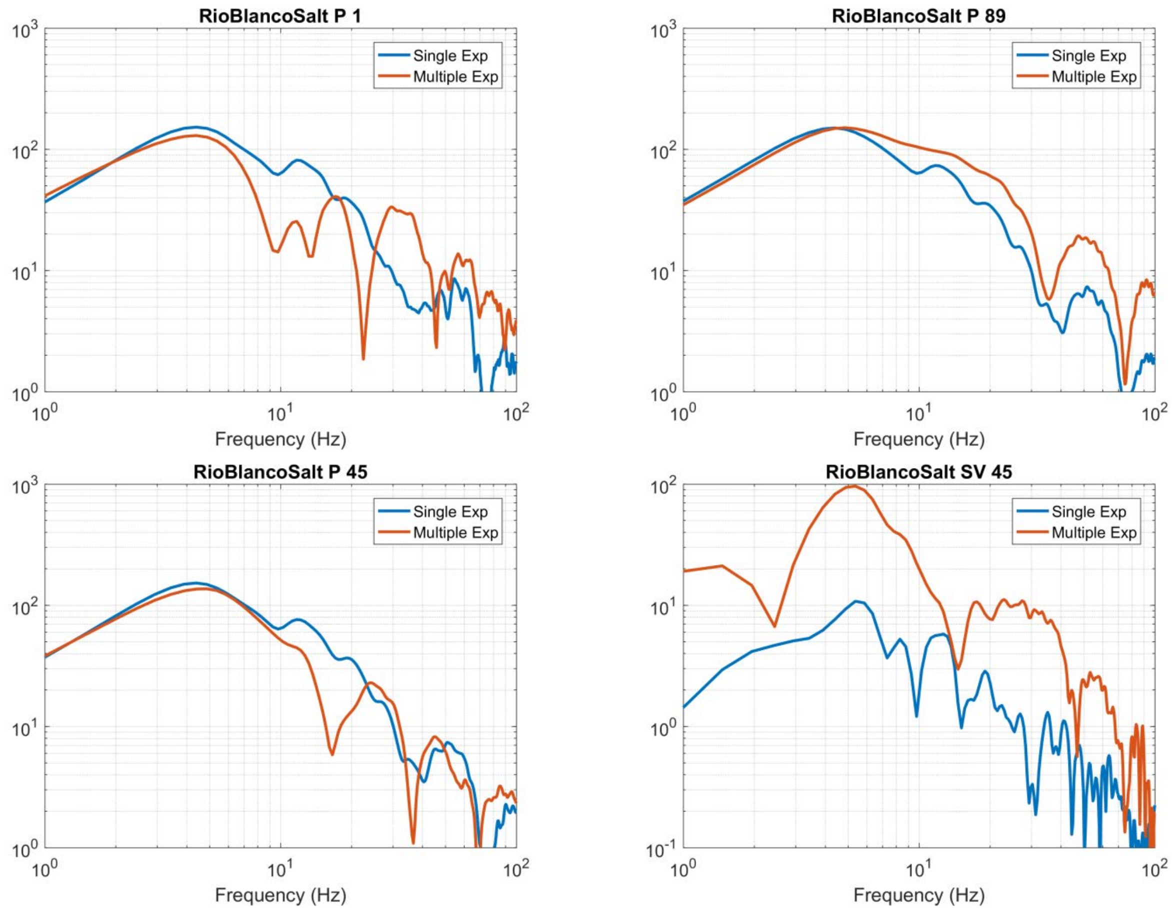

Figure 39. Spectra for the waveforms shown above.

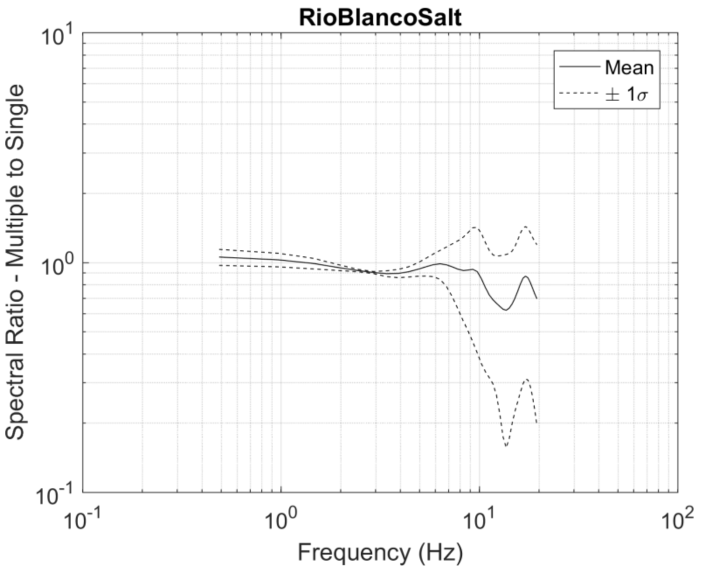

Figure 40. Ratio of multiple to single explosion averaged over all takeoff angles shown together with ±1 standard deviation.

4.1.9 Taiga: 1971/03/23

Three 15 kiloton explosions at 127m depth separated by 165m.

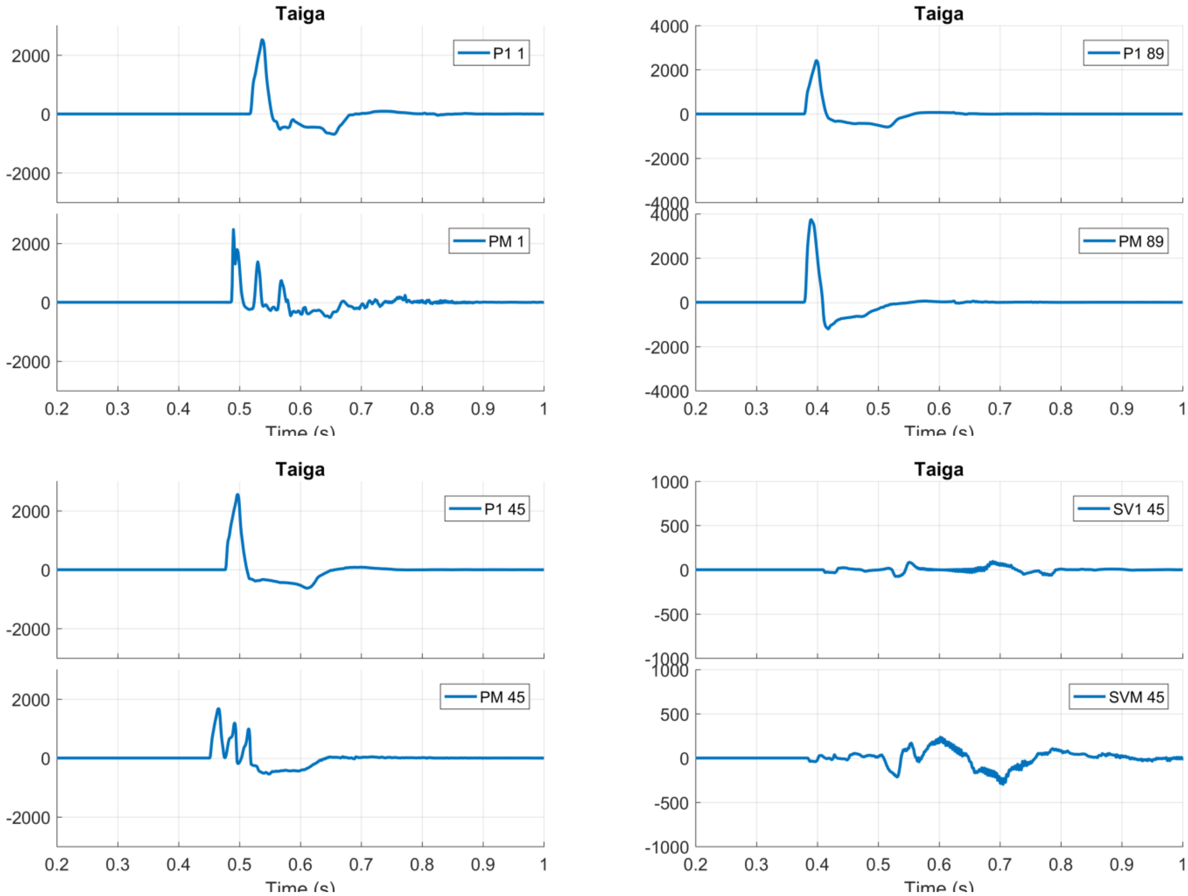

Figure 41. Waveforms from Taiga calculation. ***Top row: P waves at 1 and 89 degrees. Bottom row: P and SV waves at 45 degrees. P1 corresponds to a single explosion with the same total yield. PM to the multiple explosion.***

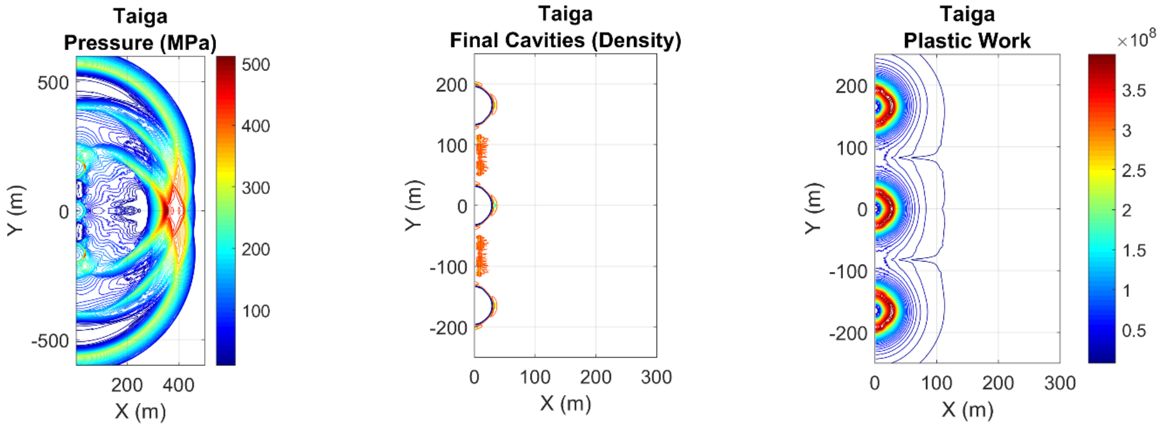

Figure 42. Left: Taiga pressure at 0.1 seconds. Middle: Final cavity shapes (contours of density). Right: Plastic work.

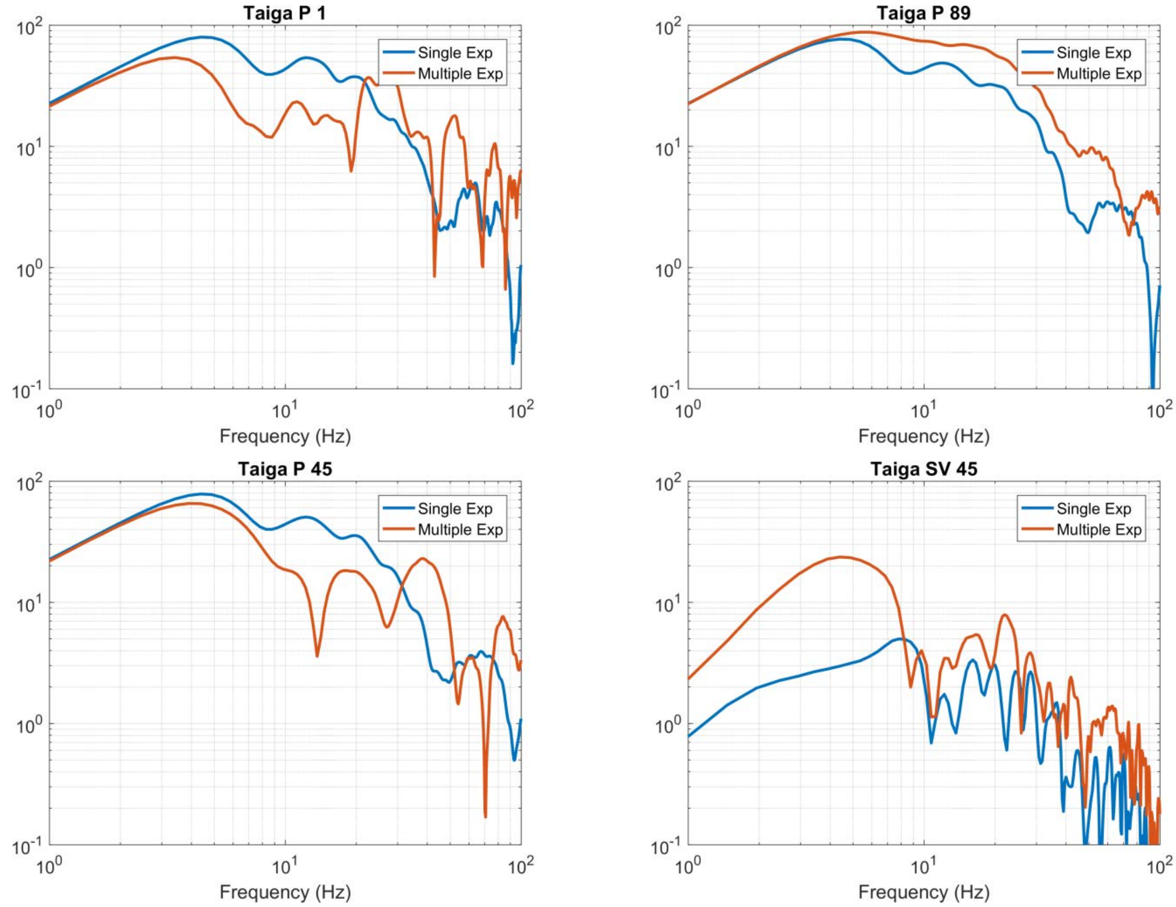

Figure 43. Spectra for the waveforms shown above.

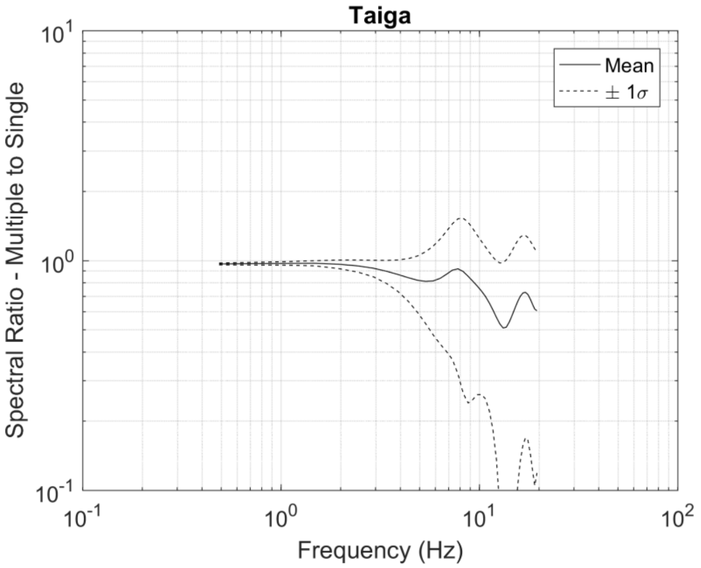

Figure 44. Ratio of multiple to single explosion averaged over all takeoff angles shown together with ±1 standard deviation.

4.1.10 Telkem 2: 1968/11/12

Three 0.24 kiloton at 31.4m depth, 40m separation.

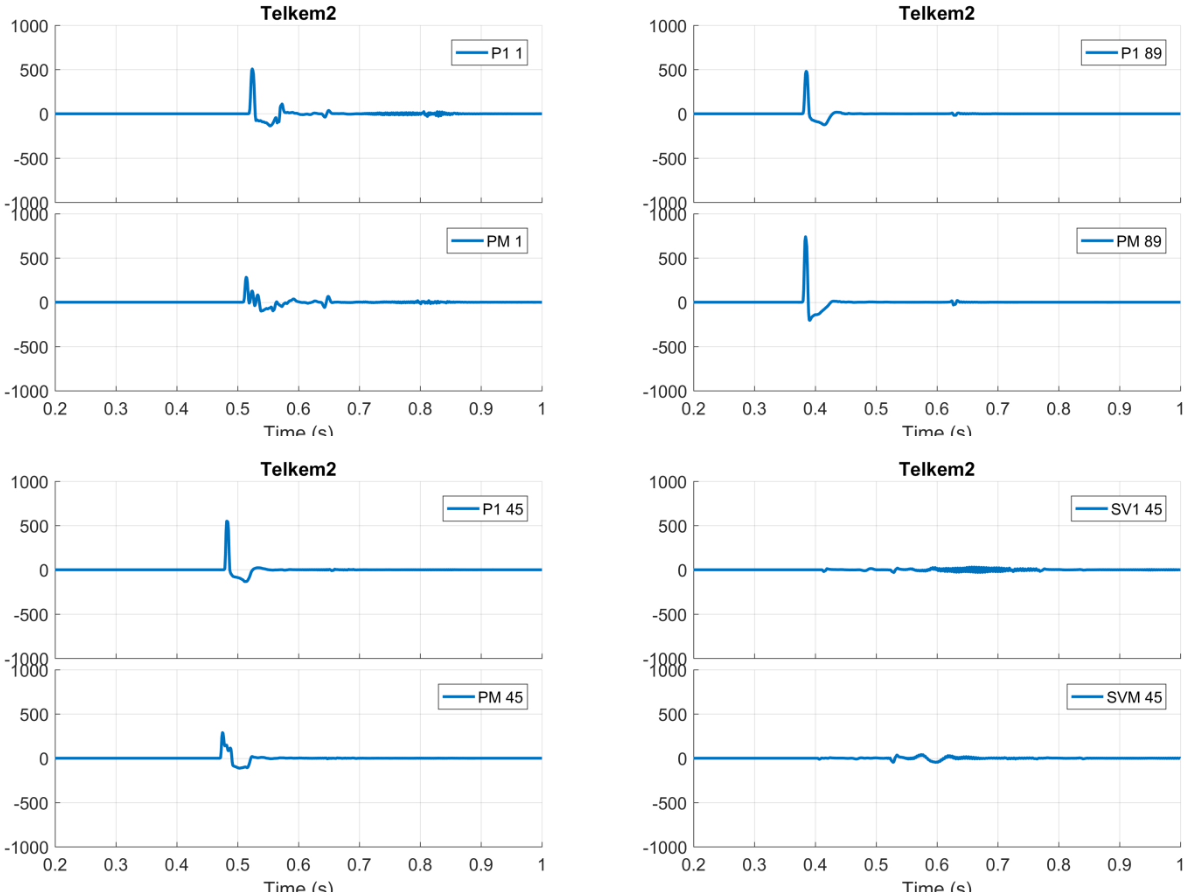

Figure 45. Waveforms from Telkem2 calculation. ***Top row: P waves at 1 and 89 degrees. Bottom row: P and SV waves at 45 degrees. P1 corresponds to a single explosion with the same total yield. PM to the multiple explosion.***

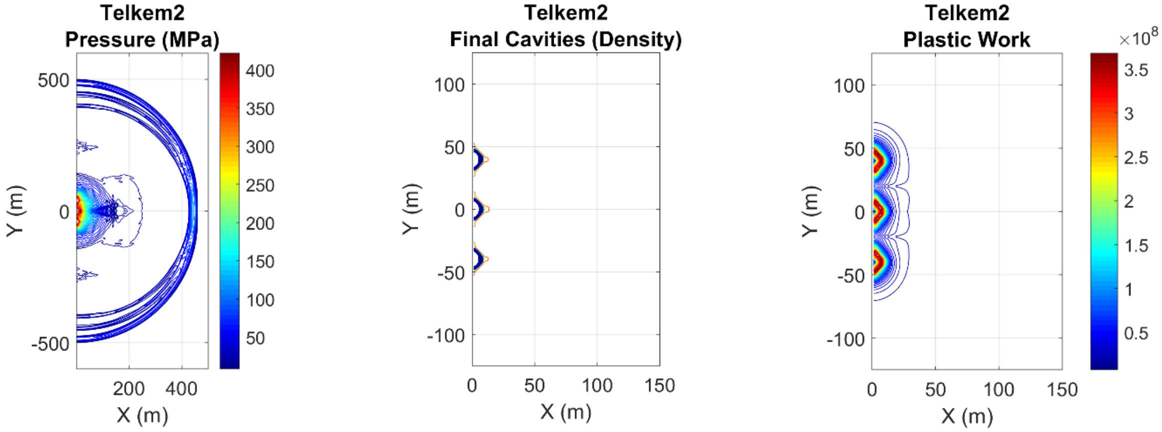

Figure 46. Left: Telkem 2 pressure at 0.1 seconds. Middle: Final cavity shapes (contours of density). Right: Plastic work.

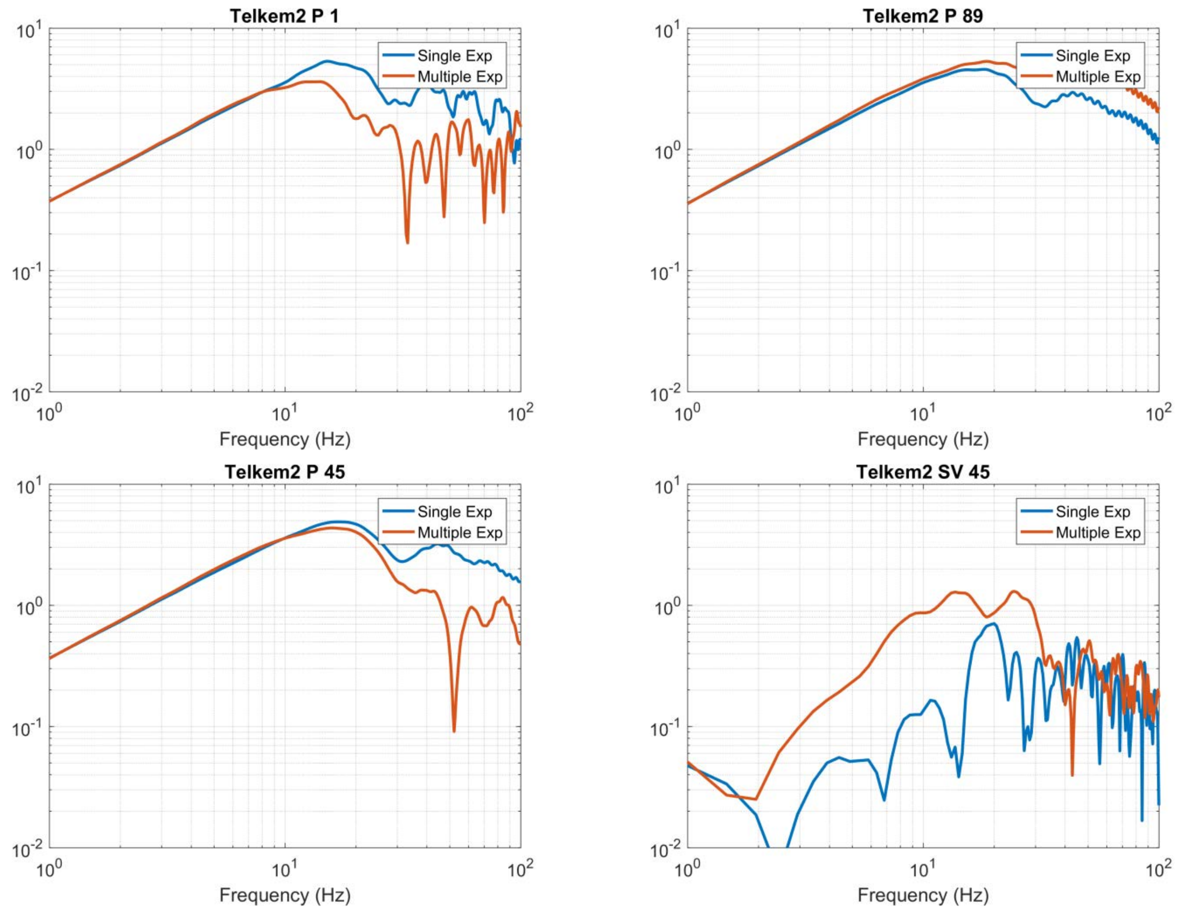

Figure 47. Spectra for the waveforms shown above.

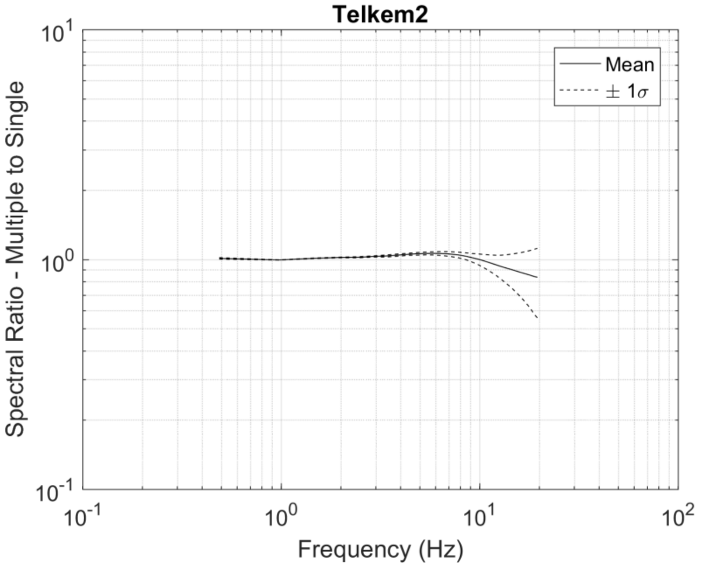

Figure 48. Ratio of multiple to single explosion averaged over all takeoff angles shown together with ±1 standard deviation.

4.2 Modification of the CRAM3D Code for Multiple Explosions

Modification of the baseline CRAM3D code to handle multiple sources required a significant restructuring of the previous 1:many source code to facilitate the many:many mappings among processors that must exchange data, a consequence of adding multiple sources.

In a CRAM3D simulation, each processor is assigned a fixed partition of the simulation grid. The outer grid is split into multiple partitions. The entire inner grid is one partition. Each processor need only know about its neighbors and how to exchange data with them. Each outer-grid partition neighbors a partition to the left and right (except at the grid edges) and possibly the inner-grid partition. The inner-grid neighbors one or more outer-grid partitions. In baseline CRAM3D each data exchange is handled by its own code block, e.g., left, right, inner, explicitly voiding 1:many relationships between the partitions, hence processors. Even the 1:many inner-outer data exchanges are executed by a (relatively inefficient) inner:all-outer broadcast and exchange of the entire rather than by exchanges among only the relevant processors of only the relevant portions of the boundary to each outer grid processor. In the updated, multiple source CRAM3D, additional sources are implemented as additional partitions, as illustrated in Figure 49. As more of these are added, the broadcast approach between inner and outer partitions becomes more wasteful, hence less viable. A significant element of the code restructuring is meant to provide explicit support for these new many:many processor relations for the purpose of data exchange, without significant code inflation. Base variables relating to the inner- and outer-grid specification and interfaces have been grouped into appropriate structures, which are instantiated as arrays to represent the multiple grids and partitions with which a given processor must exchange data. With more than one source-grid processor, the baseline mapping between processor roles and MPI ranks has been completely replaced with a dynamic mapping that supports any number of sources and outer partitions. Many operations have also been vectorized to take advantage of related compiler efficiencies while reducing code bulk and complexity related to unnecessary looping structures.

We also pursue several efficiency-related enhancements that are warranted by the expanded complexity of multiple sources and the increasing sizes of new simulations.

Improved Efficiency of MPI Data Exchange:

Run time is becoming an increasingly important consideration in the CRAM3D simulations as their sizes increase. The expansion to multiple sources has brought into new relief some limitations in the existing implementation of the MPI data exchanges that can dramatically impact run time. In the baseline implementation of CRAM3D, inter-process

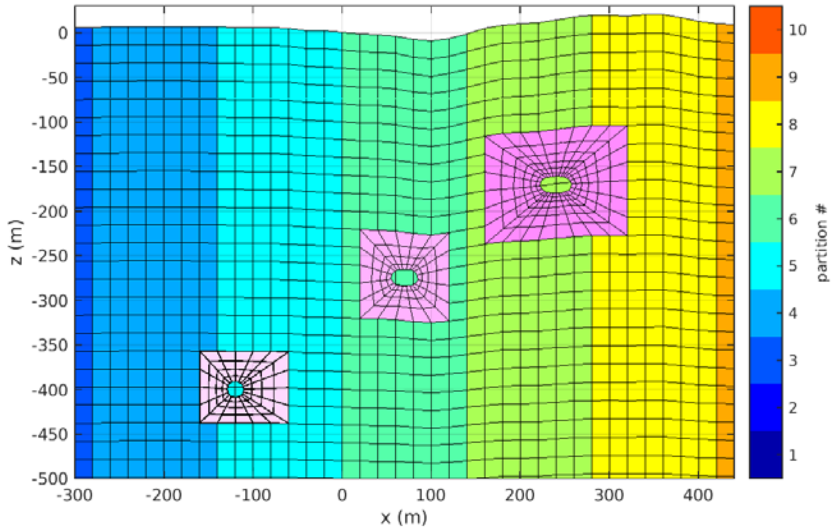

Figure 49. Partitions in a CRAM3D simulation. Each inner grid constitutes its own partition/processor.

communications (IPC) quickly became the run-time limiting factor over computation as more processors were engaged, even for modestly sized simulations. The restructuring of CRAM3D has eliminated most of this problem. Table 2 shows run times for repeated CRAM3D equilibrium simulations performed on the AFRL DoD Supercomputing Resource Center high-performance computing machine, Thunder, using different numbers of CPUs. The dimensions of the simulation grid are 300x200x100 (x,y,z). Currently, CRAM3D supports partitioning of the outer grid in the x direction only and requires a minimum of two zones per partition, which means that at most 150 processors can be applied to the outer grid (i.e. 2 x-zone per processor). Run time improves almost proportionally with the number of processors with a degradation of only about 10% going from 50 to 100 processors and 15% going from 75 to 150 processors.

Table 2. CRAM3D equilibrium run times

Machine	# Outer-Grid CPUs	# X-zones /processor	CRAM3D	Time/X-zone
Thunder	50	6	2:57	1769
Thunder	60	5	2:30	1796
Thunder	75	4	2:05	1872
Thunder	100	3	1:38	1961
Thunder	150	2	1:13	2181

Several inefficiencies in baseline CRAM3D’s implementation of data exchange that contribute to this IPC wall are addressed in the updated multiple source CRAM3D:

1) each processor executes its data exchanges serially, each blocking the next until finished, e.g. exchange with left, once done then right, once done then inner,
2) the inner grid broadcasts the entire boundary to all processors instead of just the relevant portions to its neighbors only, and
3) elastic and viscous components of force are unnecessarily exchanged separately at each iteration.

The weakness of (1) is that at each step, all processors wait for the slowest processor to complete the last step. We modified CRAM3D to execute just the outer-outer exchanges asynchronously, using non-blocking send and receive operations. The reduction in run time is about 20% at 75 processors.

The weakness of (2) is that the source-to-outer grid IPC data volume grows with the number of outer-grid processors, even though the necessary amount of data for exchange almost fixed. MPI broadcasts purport to have $\log_2$ efficiency with respect to the number of processors involved but even at 100 processors this may be the equivalent of adding the IPC burden of O(10) additional processors. We modified CRAM3D to replace the broadcast exchanges with point-to-point exchanges between source and bordering outer partitions of just the boundary portions relevant to each exchange. Thus each boundary node is only exchanged once.

Finally, in each CRAM3D cycle, the elastic and viscous contributions to force are not used individually after they are exchanged; only their sum is used. The only exception is that in relatively rare dump cycles they may be individually written to disk, thus, item (3) effectively doubles the exchange data volume over what is necessary. We modified CRAM3D to exchange only the total force in all but the dump cycles where the elastic and viscous forces are exchanged individually.

Further Reduction of IPC Data Volume

Beyond these improvements, the main additional way to reduce the impact of IPC on run time is to reduce the total area of the processor-processor boundaries for a given number of processors, thus reducing the total amount of data exchanged. This can be done by improving the partitioning geometry. In CRAM3D, the outer grid is partitioned in only the X direction. The volume of data that must be exchanged among partitions reduces dramatically if the grid is partitioned in 2 dimensions, even more in 3 dimensions. Consider even partitioning an M^3 grid over N total processors. The surface areas that need to be exchanged are proportional to M^2 regardless of how it is partitioned, but to N, 2, and $3/N^{1/3}$ for partitioning in 1, 2 and 3 dimensions respectively. For M=1000 zones and N=1000 processors, the 2-D and 3-D partitioning data volumes are 1/500th and 1/3000th of that for 1-D partitioning. More involved modifications to CRAM3D are required to implement this capability. As such it is currently a secondary goal. However, because its impact may be significant, CRAM3D has been structured with the anticipation of extending the partitioning to 2 or 3 dimensions in the future.

Improved Specification of Source (Inner)-Grid and Source-Model Specifications:

In baseline CRAM3D, the user is responsible for deriving self-consistent parameters for constructing the inner grid, (innermost layer width, a dilation factor, number of layers). Grids may be specified with unintended properties, such as inner-grid zones larger than outer grid zones, or even pathological properties that ultimately cause the program to fail (e.g., source outside or too close to the edge of the inner grid). This specification has been updated with options that construct a sensible grid from minimal specification. For example, the source grids in Figure 49 were generated by CRAM3D, specifying only the cavity shape, the desired number of layers and the inner layer thickness. CRAM3D computed the layer dilation factor to make the layers seamlessly blend with outer grid. In addition, the source-grid and source-model parameters can now be specified in tabular formats using human-readable parameter tags.

Multiple Explosion Test Case – 1 kiloton nuclear explosion and 1 kiloton chemical explosion

As a test case of multi-explosion CRAM3D, we perform a calculation with two explosions with the same yield, one nuclear and one chemical. Figure 50 shows velocity magnitude from two explosions separated by 200 meters at 0.06 and 0.15 seconds. The left explosion is a 1 kiloton nuclear explosion, and the right a 1 kiloton chemical explosion, both detonated simultaneously.

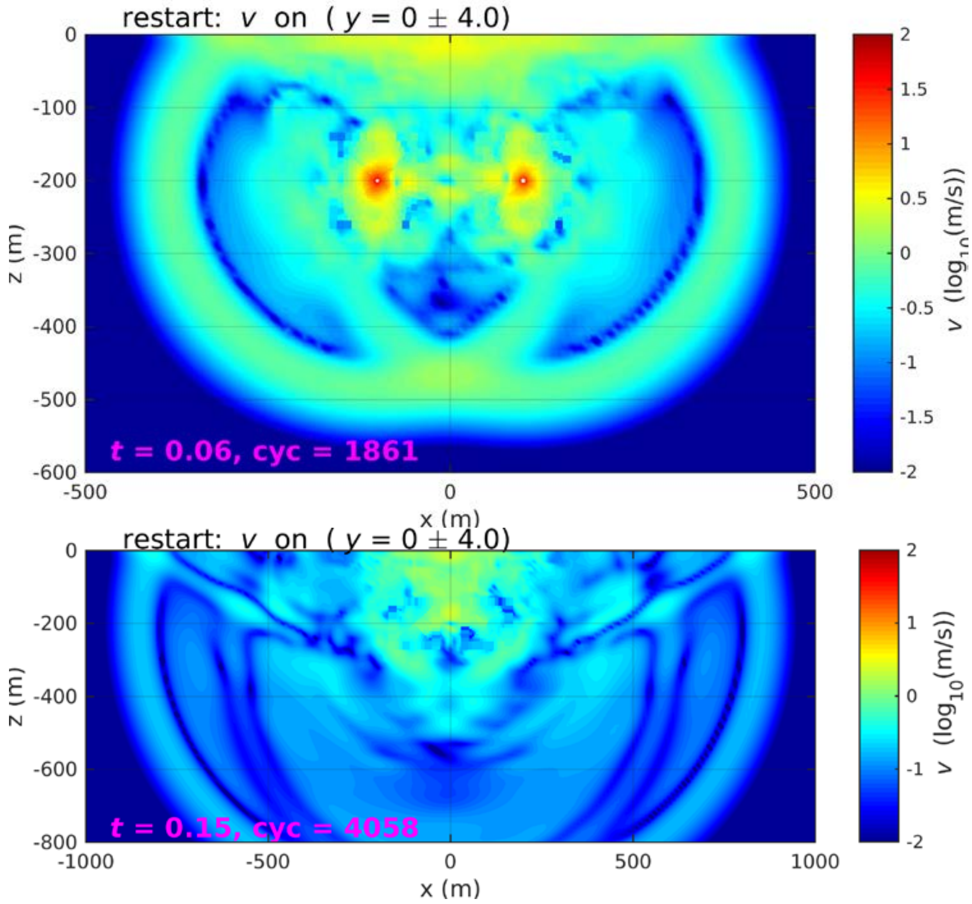

Figure 50. Velocity magnitude from a one kiloton nuclear explosion (left) and a one kiloton chemical explosion (right) separated by 200 meters at 0.06 and 0.15 seconds.

Figure 51 shows the evolution of tensile cracks from 0.02 to 0.10 seconds for the same calculation with the nuclear explosion is on the left, and chemical (ANFO) on the right.

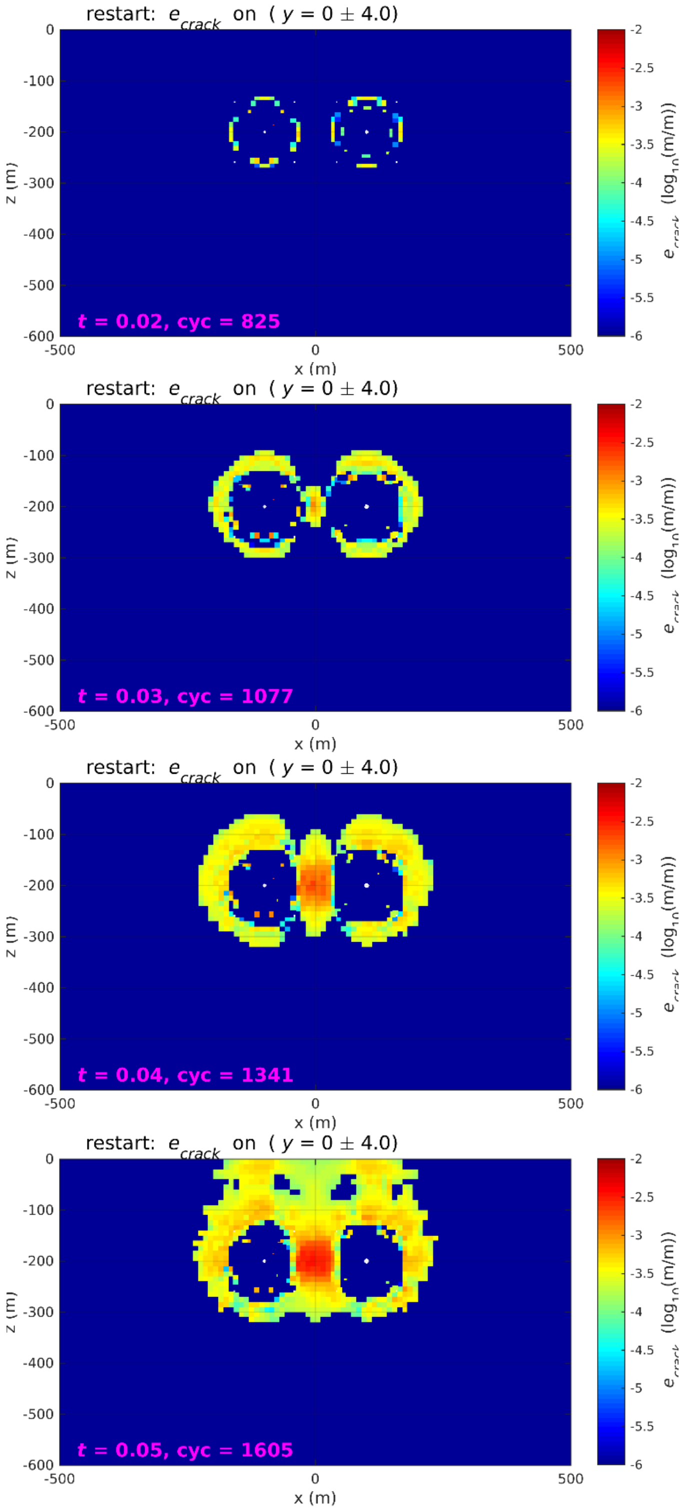

Figure 51. Evolution of tensile cracks from 0.02 to 0.10 seconds. ***Nuclear explosion is on the left, chemical (ANFO) on the right. The quantity shown is log of the crack strain. Time and cycle number are shown on the lower left in each figure.***

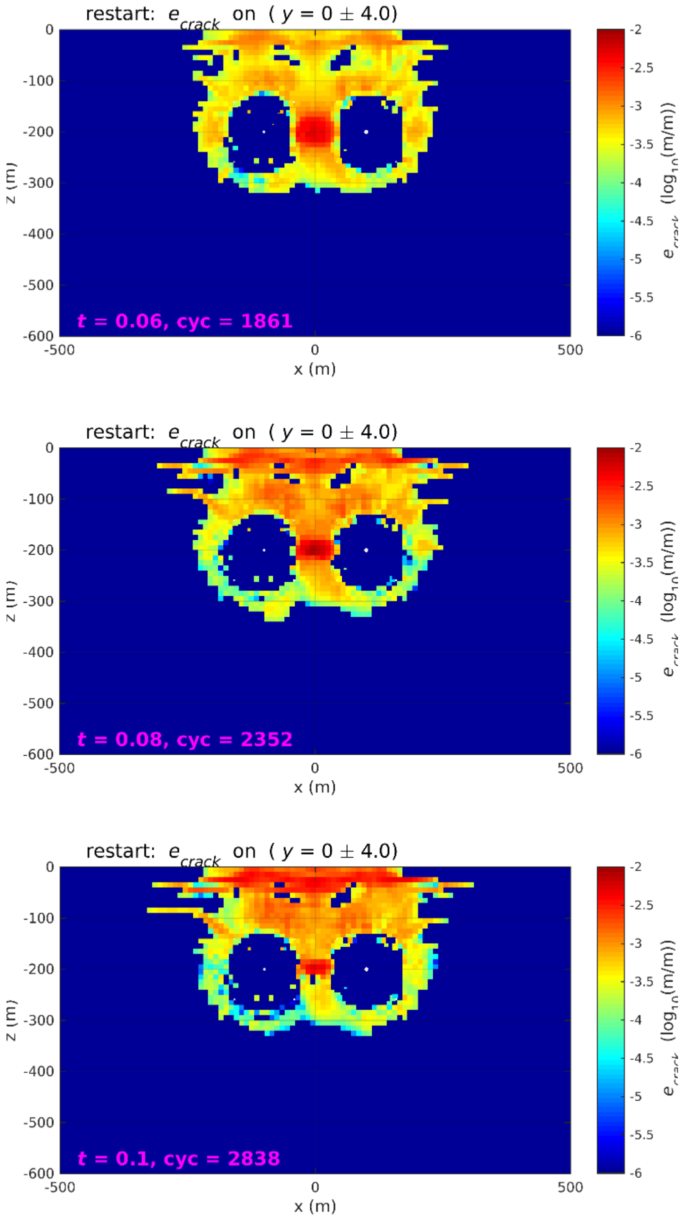

Figure 51 (Continued). Evolution of tensile cracks from 0.02 to 0.10 seconds. ***Nuclear explosion is on the left, chemical (ANFO) on the right. The quantity shown is log of the crack strain. Time and cycle number are shown on the lower left in each figure.***

4.3 CRAM3D Calculations of Multiple Explosions

We perform CRAM3D calculations for a subset of the explosions done with STELLAR (Table 1), excluding the deepest events. With CRAM3D, we can now include the effect of the free surface and use a wider set of material models.

4.3.1 Dnepr2 and Dnepr1

For the first calculation, we model the explosions Dnepr1 and Dnepr2. Dnepr2 consisted of two 1.7 kt explosions at 175m depth, 75m apart horizontally. Apatite is a hard, dense rock, so we use our Shoal granite model for this calculation. This model has a density of 2600 kg/m^3, and at 1.7 kt, using the rule of thumb that a nuclear explosion vaporizes 70 tons/kiloton, we estimate the initial cavity radius at 2.219 meters. We use a uniform 5 meter zoning for the calculation and run it until 0.4 seconds. Figure 52 shows part of the grids and the cavity at the start and end of the calculation. The cavities expand to about 12 meters in radius.

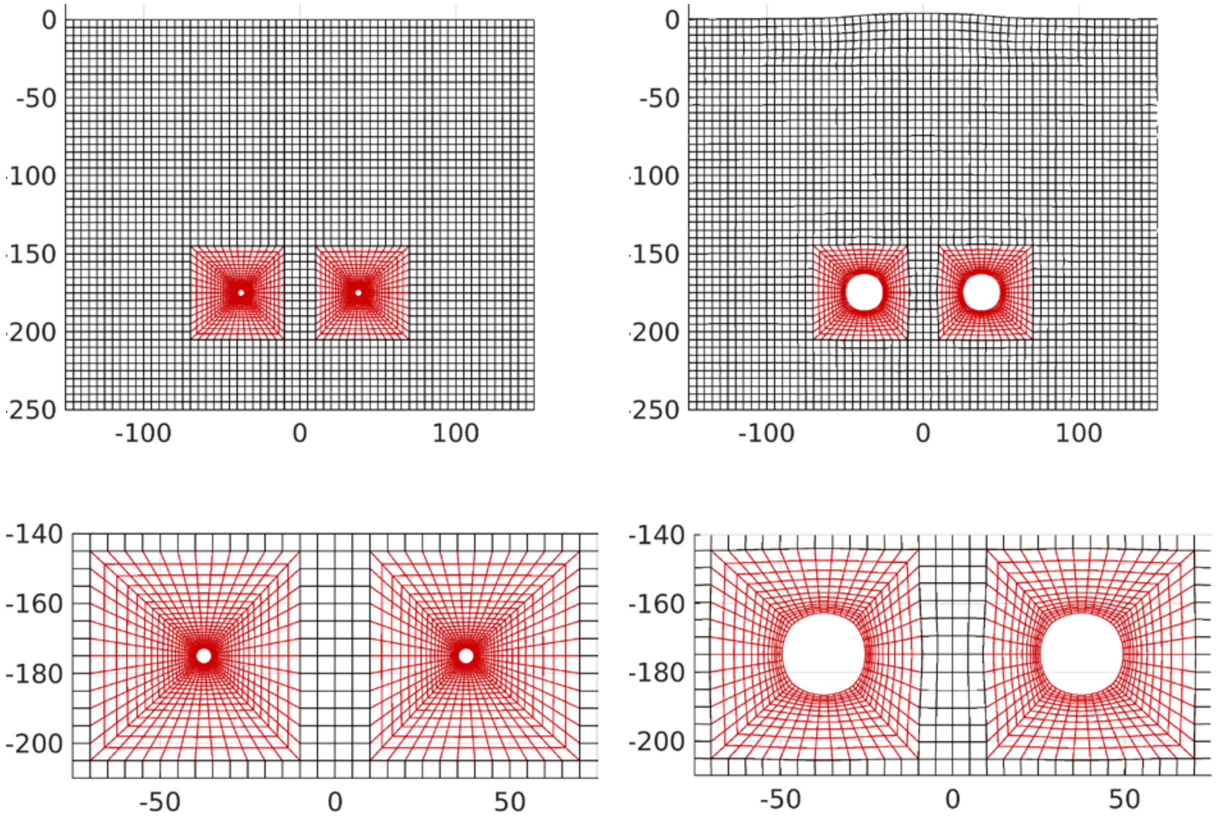

Figure 52. Initial (left) and final (right) grids. Top: grid from below cavity to surface. Bottom: expanded view of inner grids.

Figure 53 shows the regions of tensile cracking at nonlinear yielding, which are extensive, even though the explosion is approximately at normal containment depth for the total yield of 3.4 kilotons.

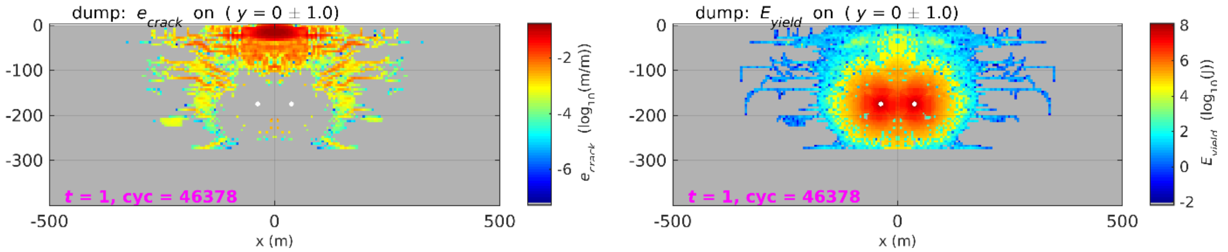

Figure 53. Dnepr2: Tensile crack strains (left) and plastic work (right) show regions of nonlinear deformation.

We also performed a calculation of the single explosion Dnepr1, modifying the parameters slightly for ease of comparison with Dnepr2. The calculation was at the same 175m depth and with a yield of 3.4 kt, equal to the sum of the two Dnepr2 explosions. The initial radius of the cavity is 2.796 meters and it expands to 14.6 meters. Figure 54 shows the grid at the start and end of the calculation (compare with Figure 52).

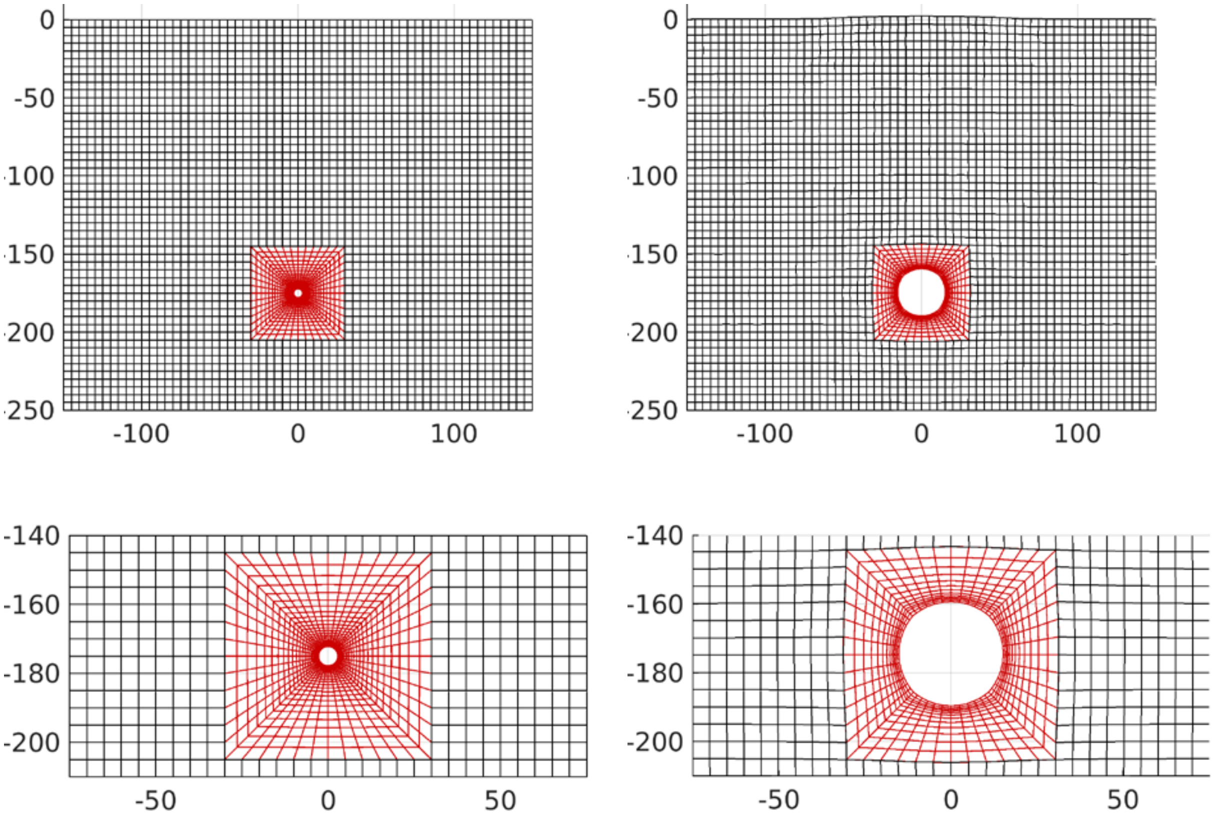

Figure 54. Initial (left) and final (right) grid. Top: grid from below cavity to surface. Bottom: expanded view of inner grids.

Figure 55 shows the regions of tensile cracking at nonlinear yielding for the Dnepr1 calculation, which are similar to those for Dnepr2, but spread out more for Dnepr2.

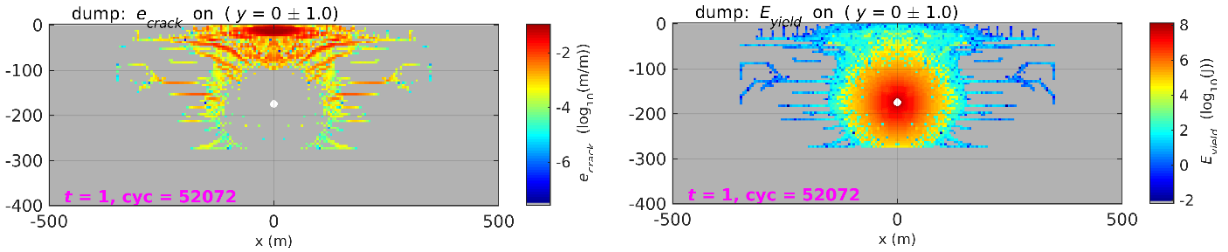

Figure 55. Dnepr1: Tensile crack strains (left) and plastic work (right) show regions of nonlinear deformation.

We used the representation theorem to calculate body waves, surface waves and full waveform seismograms. Figure 56 shows the P, SV and SH waves calculated at a 20 degree takeoff angle from the two calculations. Dnepr1 is axisymmetric so we only show one azimuth. For Dnepr2, we show 3 azimuths. Here 90 degrees is along the direction of the two explosions and 0 degrees is perpendicular to it. There are only very slight differences between the P and SV waves in the two calculations. The double explosion generates an SH wave at a 45 degree angle that is absent in the single calculation and absent at the other angles in both (SH would not be allowed by symmetry at zero or 90 degrees).

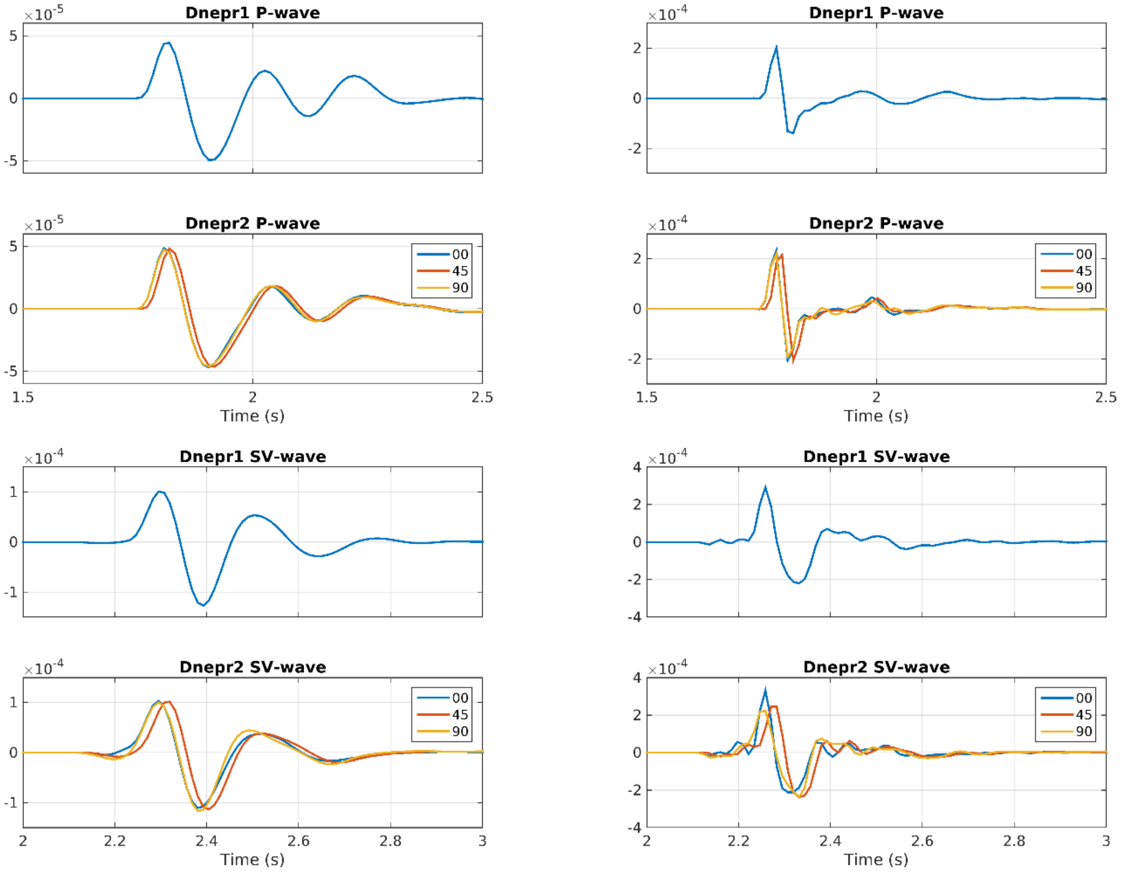

Figure 56. Body waves from Dnepr1 and Dnepr2 calculations. ***Left: lowpass filtered at 5 Hz. Right: lowpass filtered at 20 Hz. Top: P-waves, middle: SV, bottom: SH.***

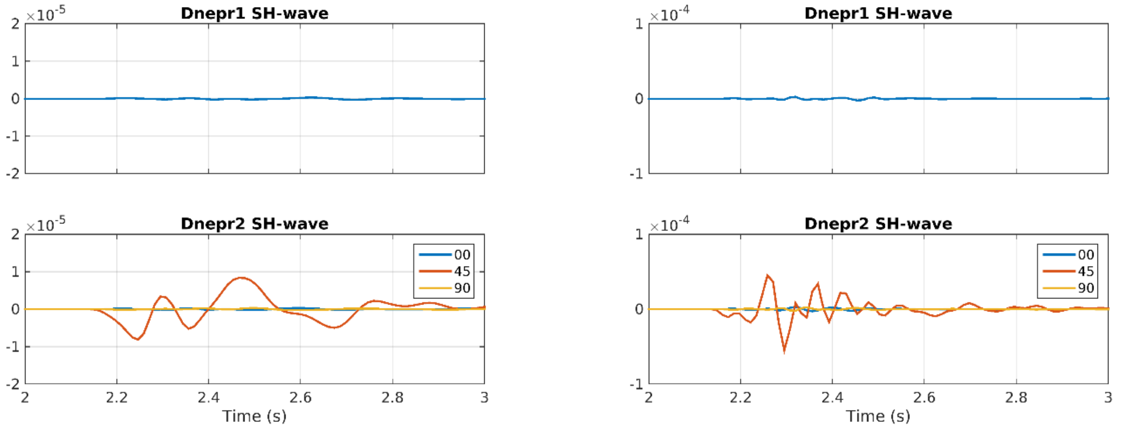

Figure 56 (Continued). Body waves from Dnepr1 and Dnepr2 calculations. ***Left: lowpass filtered at 5 Hz. Right: lowpass filtered at 20 Hz. Top: P-waves, middle: SV, bottom: SH.***

Long period surface waves, low pass filtered at 0.1 Hz are shown in Figure 57. There is some variability in the surface waves from Dnepr2, with smaller surface waves at 90 degrees, parallel to a line through the explosions, and larger at 0 degrees, perpendicular to the line. There is also a Love wave, about half the amplitude of the Rayleigh wave, at 45 degrees. Note that our earlier calculations for a whole space showed that azimuthal variability went away at long periods, but that is not true for surface waves. Surface waves are generated by the static horizontal displacement outside the explosion, and as Figure 58 shows, the double explosion causes an amplification of the displacement in the direction perpendicular to the two explosions.

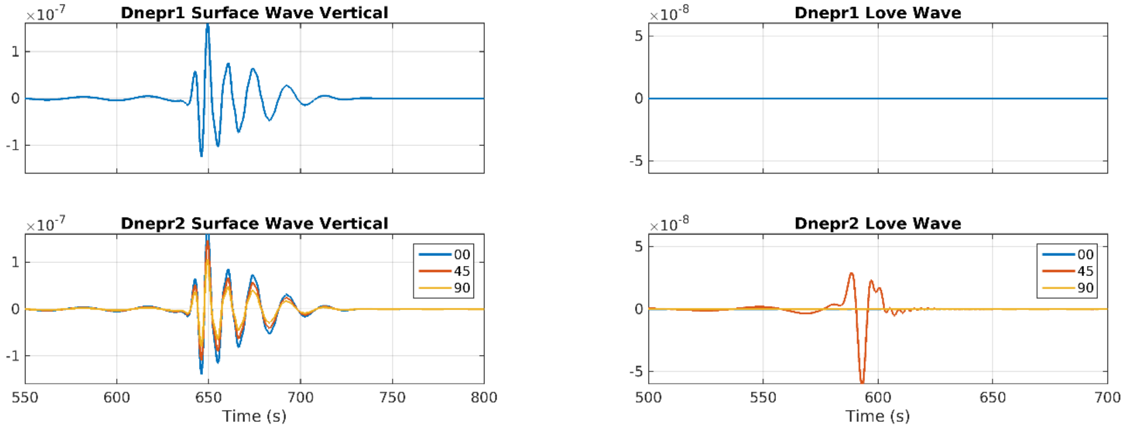

Figure 57. Rayleigh wave (left) and Love wave (right) from Dnepr1 (top) and Dnepr2 (bottom) calculations.

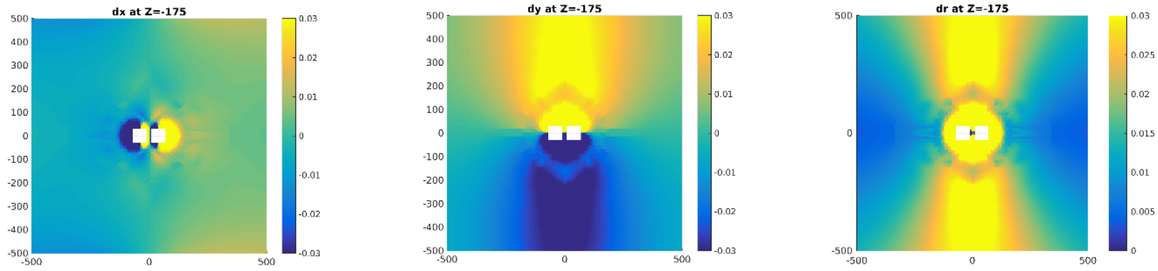

Figure 58. X (left), Y(middle) and radial (right) final displacement at shot level in the Dnepr2 calculation.

Figure 59 shows full waveform seismograms at 250 km. The results are consistent with the other waveforms. The surface wave shows some azimuthal variability and there is a Love wave at 45 degrees. There is little difference in the regional P and S waves.

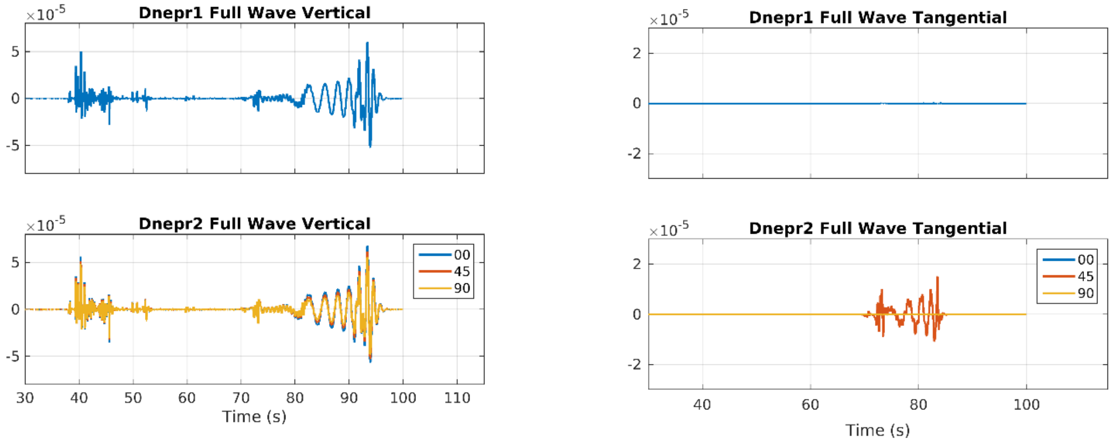

Figure 59. Full waveform seismograms at 250 km from the Dnepr1 and Dnepr2 calculations. Lowpass filtered at 20 Hz.

4.3.2 Taiga

The next calculation is Taiga. Taiga consisted of three 15 kiloton explosions at 127 meters depth, each separated by 165 meters. The explosions were described as in “sandstone/shale”. We modeled this using a below water table model for Pahute Mesa. The rock density is 2000 kg/m^3 and the initial cavity has a radius of 5.00 meters. The Pahute Mesa model has an initial porosity of 2%, which is crushed out at a pressure of 400 MPa. The effective stress model is used, which means that the rock becomes much weaker as the pores are squeezed out. The crush curve for this material is shown in Figure 60.

This calculation is considerably more difficult as it is very shallow (it was intended for excavation). This causes large amounts of tensile cracking near the surface that can cause instability in the calculation. Figure 61 shows the grid near the explosions at the start and end of the calculation. The surface has nearly 50 meters of uplift and the cavities expand to about 70 meters in size.

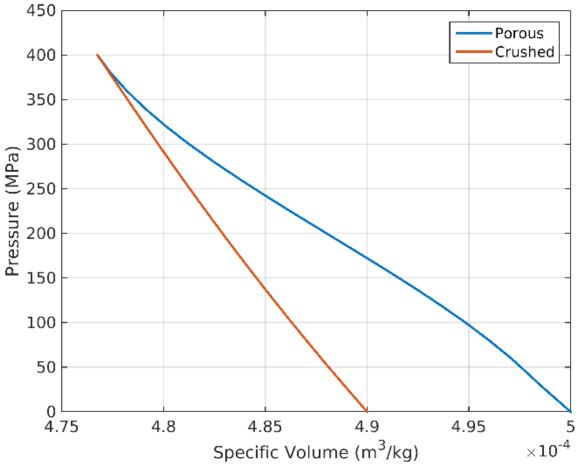

Figure 60. Crush curve for material used in the Taiga calculation.

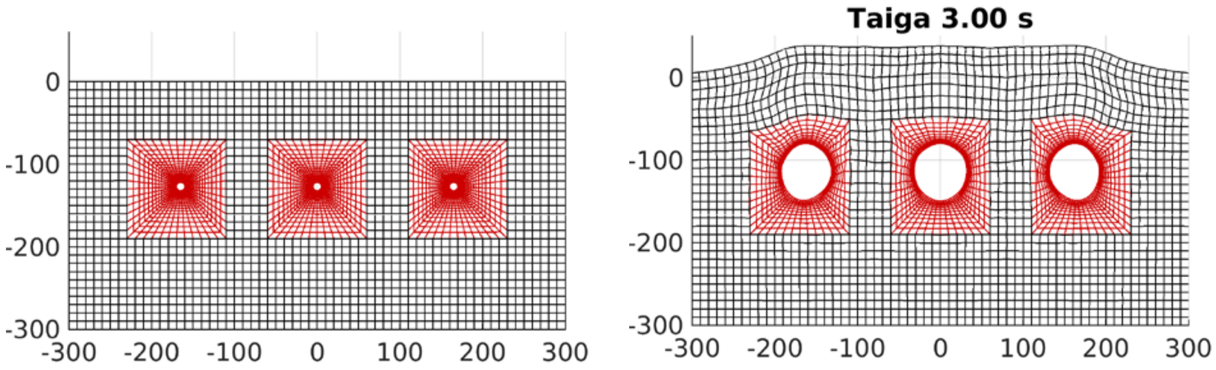

Figure 61. Grid at the start (left) and end (right) of the calculation.

For comparison, we run a single 45 kt explosion at the same scaled depth as the shallower 15 kiloton explosions, which is a depth of 183 meters. The initial cavity radius is 7.22 meters. The cavity expands to more than 50 meters vertically and 40 meters horizontally, and there is about 60 meters of uplift above the explosion (Figure 62). In both cases, the nonlinear deformation is huge (Figure 63).

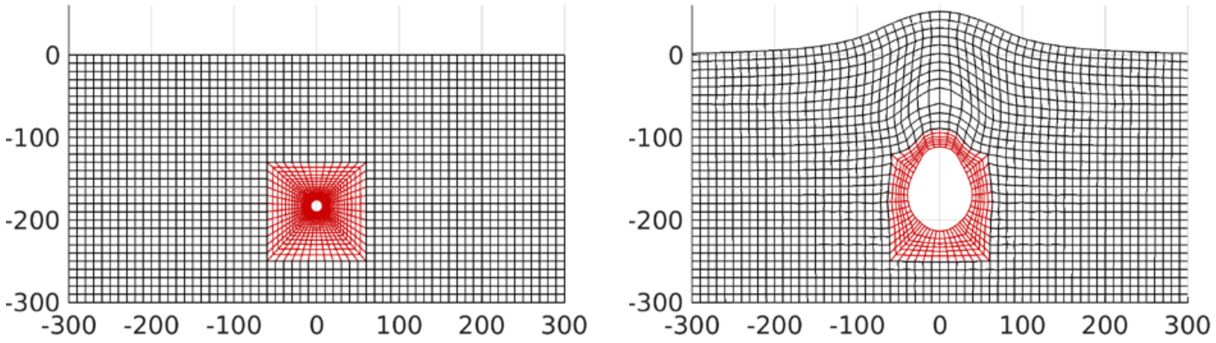

Figure 62. Initial and final grids for the Taiga1 calculation.

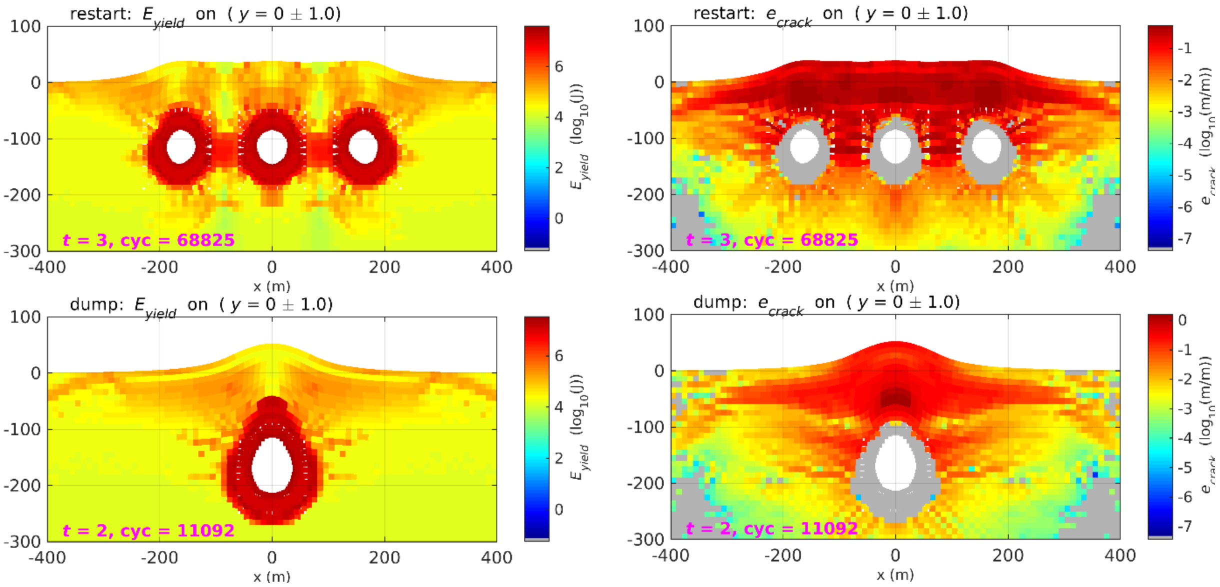

Figure 63. Top: plastic work (left) and tensile crack strains (right) from the Taiga calculation. Bottom: plastic work and crack strains from the Taiga1 calculation.

We used the representation theorem to calculate surface waves and far-field body waves. Figure 64 shows the P, SV and SH waves calculated at a 20 degree takeoff angle from the two calculations. Taiga1 is axisymmetric so we only show one azimuth. For Taiga, we show 3 azimuths. Here 90 degrees is along the direction of the three explosions and 0 degrees is perpendicular to it. There are small differences between the P waves in the two calculations. SV waves are smaller and more variable for the triple calculation than for the single calculation. This is probably because the single explosion generates a more coherent pS phase than the triple explosion. The triple explosion generates an SH wave at a 45 degree angle that is absent in the single calculation and absent at the other angles in both (SH would not be allowed by symmetry at zero or 90 degrees).

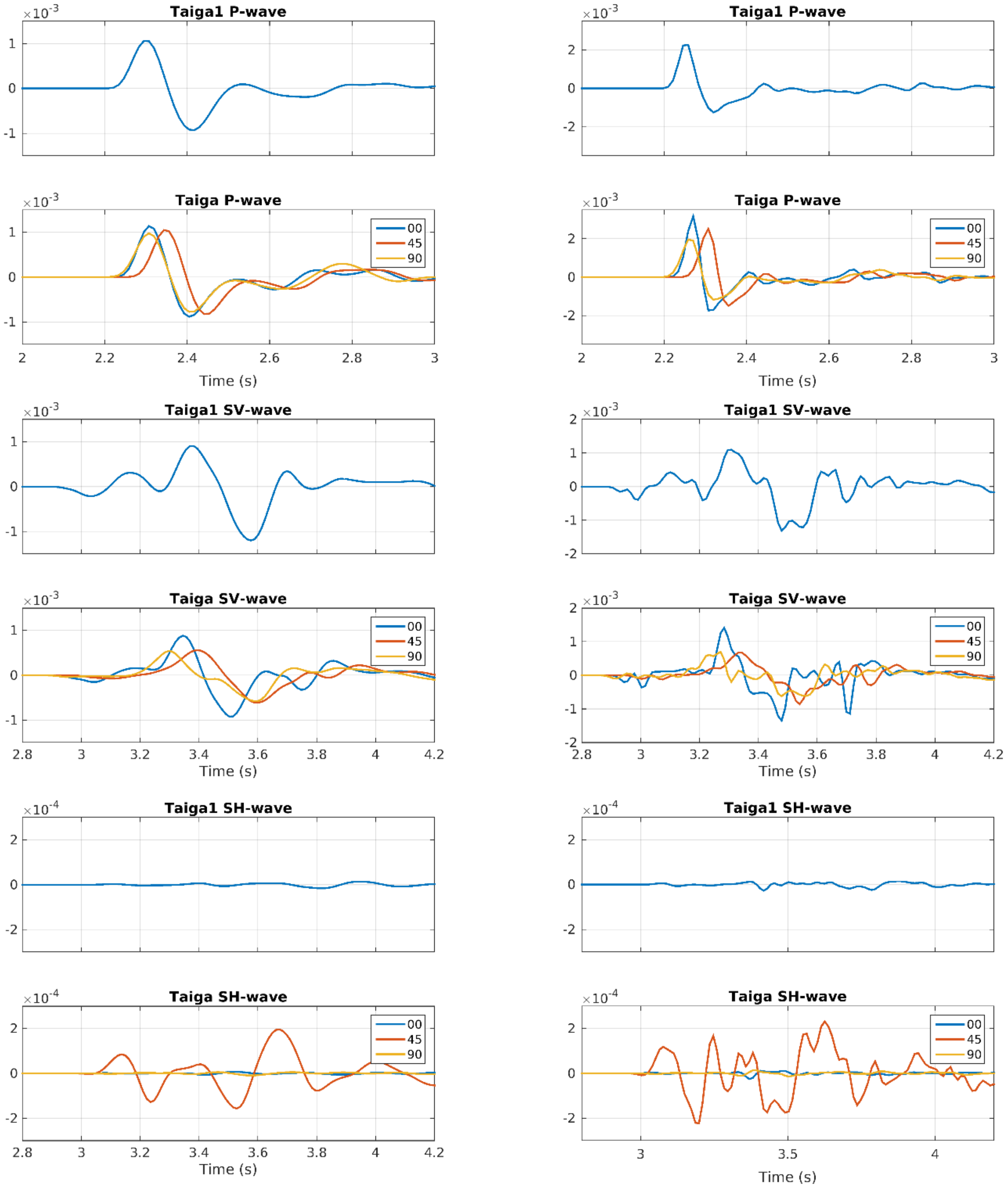

Figure 64. Body waves from Taiga1 (single explosion) and Taiga (triple explosion) calculations. ***Left: lowpass filtered at 5 Hz. Right: lowpass filtered at 20 Hz. Top: P-waves, middle: SV, bottom: SH.***

Long period surface waves, low pass filtered at 0.1 Hz are shown in Figure 65. There is a Love wave from Taiga, about 10% the amplitude of the Rayleigh wave, at 45 degrees. There is also variability in surface wave amplitudes, with smaller surface waves at 0 degrees, perpendicular to a line through the explosions, and larger at 90 degrees, parallel to the line. This is opposite the radiation pattern we found for Dnepr2. Surface wave variability is smaller than for Dnepr2 and is difficult to see in Figure 65, so we show an expanded scale view in Figure 66. Figure 67 shows the static horizontal displacement: the triple explosion causes an amplification of the displacement in the direction parallel to the three explosions, again opposite what we found for Dnepr2.

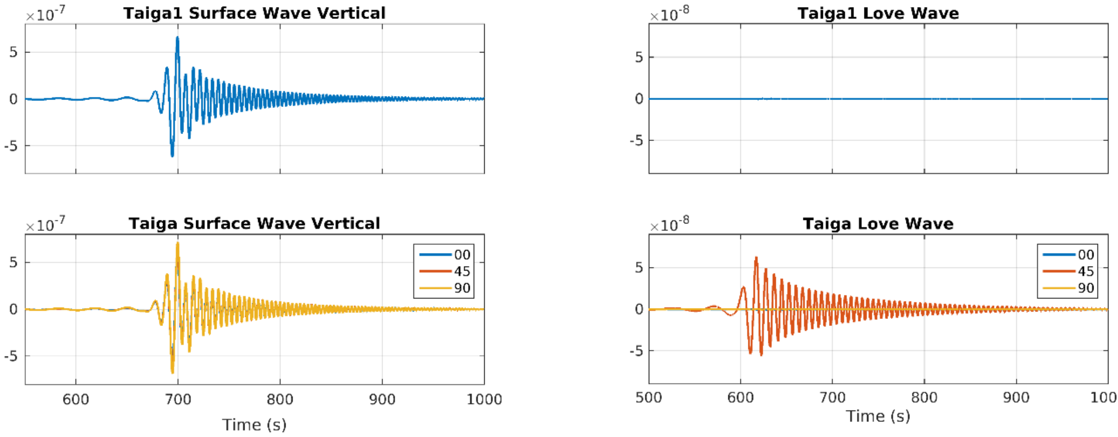

Figure 65. Rayleigh wave (left) and Love wave (right) from Taiga1 (top) and Taiga (bottom) calculations.

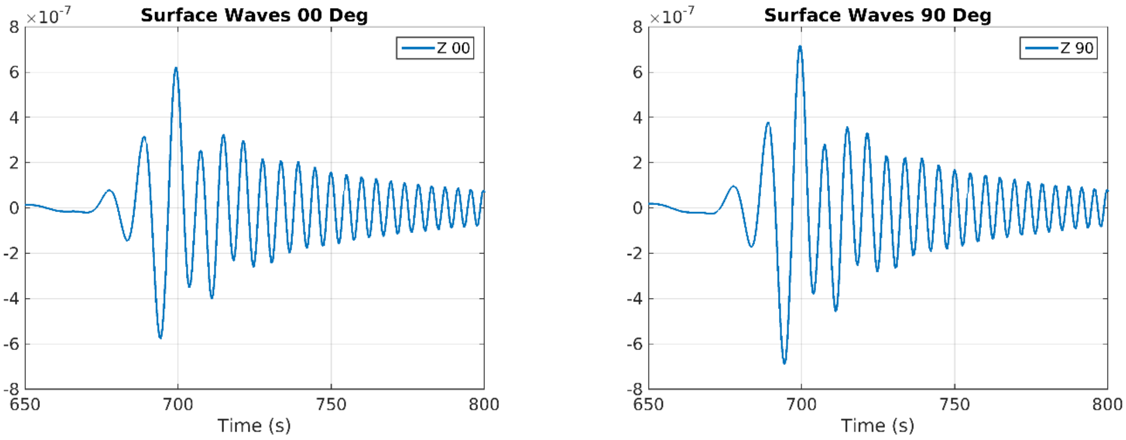

Figure 66. Vertical component Rayleigh wave from Taiga at zero degrees (left) and at 90 degrees (right). ***90 degrees is along the direction of the explosions.***

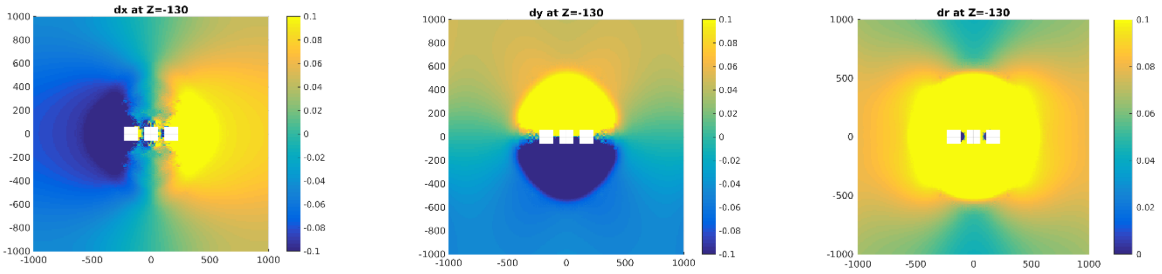

Figure 67. X (left), Y (middle) and radial (right) final displacement at shot depth for the Taiga calculation.

Figure 81 shows full waveform seismograms at 250 km. The waveforms show some small differences between Taiga1 and Taiga at different azimuths, and there is a small Love wave at 45 degrees. However, the differences are quite small.

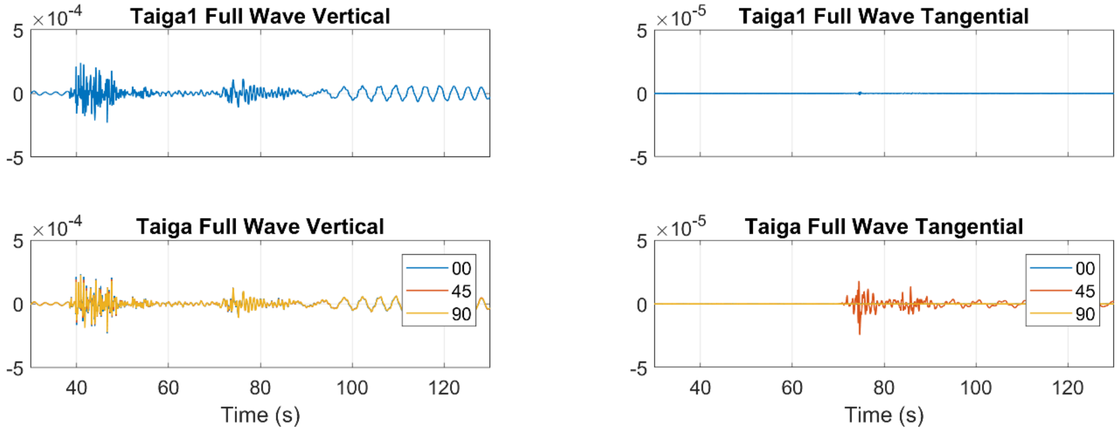

Figure 68. Full waveform seismograms at 250 km from the Taiga1 and Taiga calculations. ***Low pass filtered at 10 Hz.***

4.3.3 Azgir1

Azgir1, referred to in Sultanov et al (1999) as Azgir A-7, was a 56 kiloton explosion at 970m depth above an 18 kiloton explosion at 1040m depth in salt. This is considerably deeper than the calculations described above, and it was overburied relative to normal containment depth by a factor of 2. Consequently, the nonlinear free surface interaction is small. Figure 69 and Figure 70 show the initial and final states of the grid. As with the STELLAR calculation, the two cavities are squeezed close together and almost merge. Both cavities are distorted from a spherical shape. Figure 71 shows the plastic work generated in the two calculations. The results are similar, but not identical. The Eulerian STELLAR and Langrangian CRAM3D have a significant difference that becomes visible in cases like this where there is strong interaction between two cavities. The STELLAR calculation causes some mixing of materials, so there is some rock in the cavity and the cavity boundary becomes fuzzy, while CRAM3D boundaries always completely separate the initial materials. Both the STELLAR and CRAM3D calculations used a simple plastic salt model with a density of 2200 kg/m^3, compressional velocity of 4550 m/s and shear velocity of 2540 m/s.

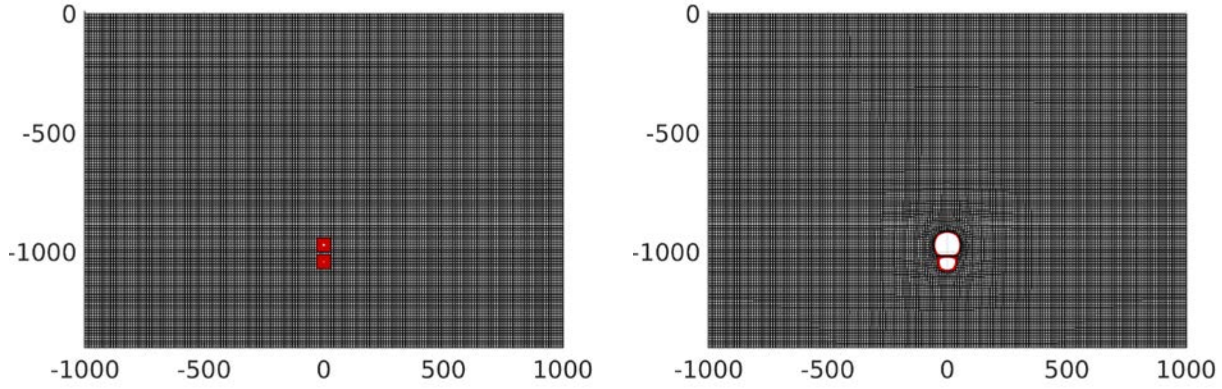

Figure 69. Initial (left) and final (right) grid states.

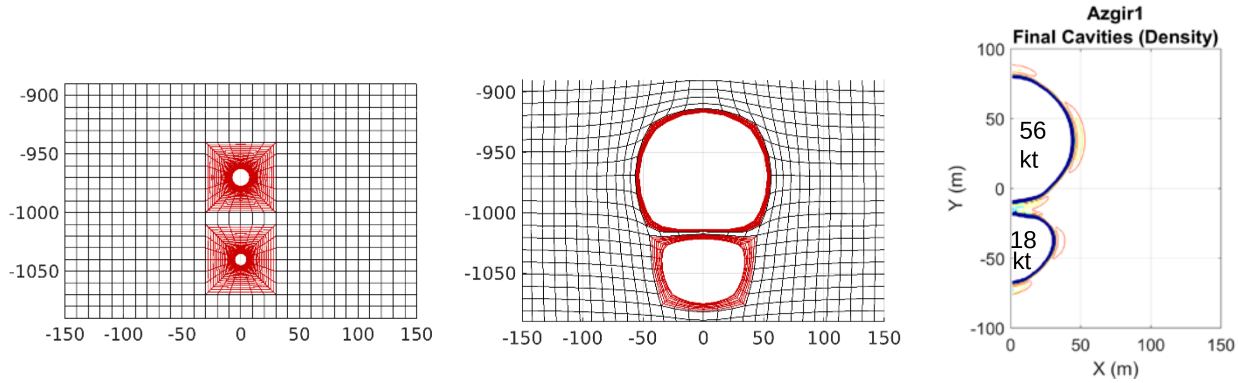

Figure 70. Initial Azgir1 cavities and inner grids (left); final cavity shapes for Azgir1 (middle) and corresponding final cavity shapes from STELLAR calculation (right).

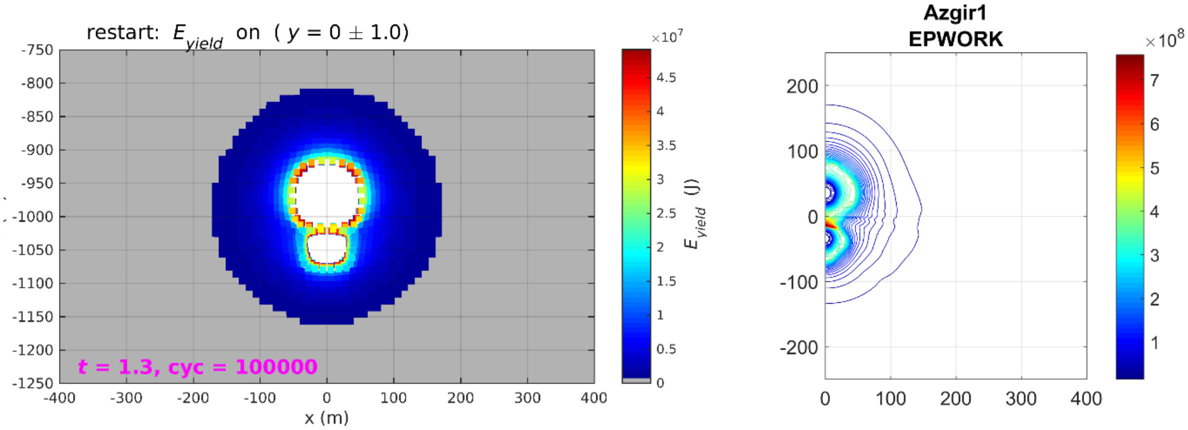

Figure 71. Azgir plastic work from CRAM3D calculation (left) and from STELLAR (right).

Figure 72 shows a comparison of far-field body waves from the CRAM3D and STELLAR calculations, both calculated for a 20 degree take-off angle. The initial P-waves are identical in both cases. CRAM3D shows strong pP and pS phases not present in the whole space STELLAR calculation. This asymmetric shape generates some shear (SV) waves not present in a single explosion. The calculated direct shear waves from the CRAM3D calculation are larger than from the STELLAR calculation, probably because of the more solid CRAM3D material boundary as discussed above. The geometry is axisymmetric so no SH waves are generated.

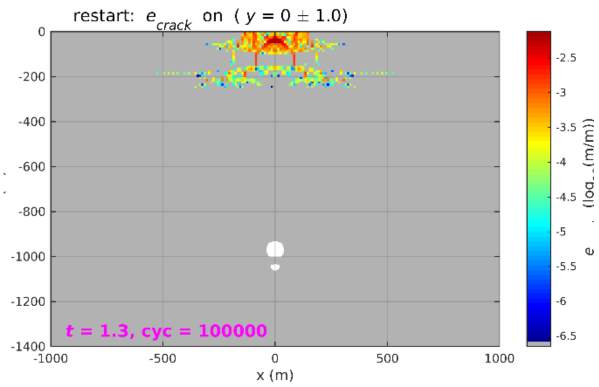

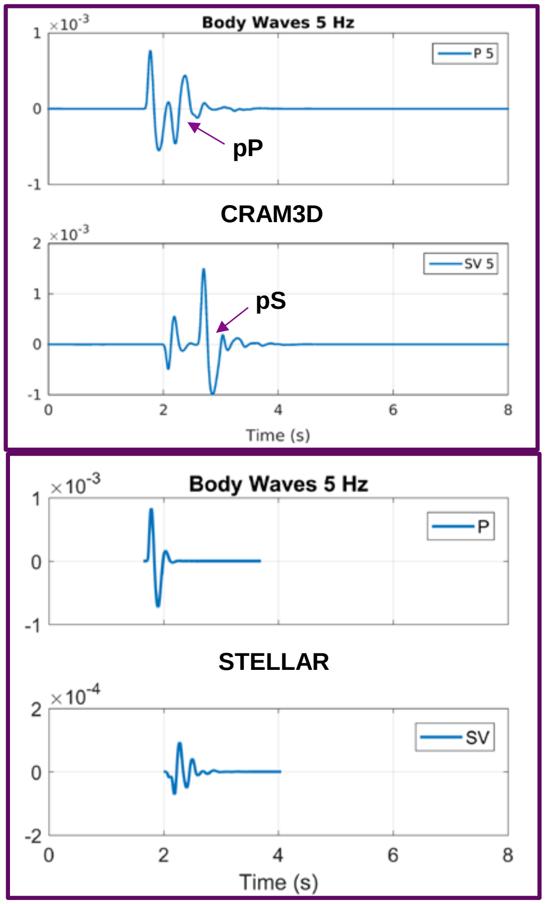

Figure 72. Top left: Regions of tensile cracking in the Azgir1 calculation. Top right: Far-field downgoing P and S waves from the CRAM3D calculation. Bottom right: Far-field body waves from the STELLAR calculation

4.3.4 Rio Blanco

Rio Blanco was a set of three 33 kiloton vertically separated explosions in shale at depths of 1779, 1899 and 2039 meters. As with the other explosions, we performed two CRAM3D calculations, one with the triple explosion and one a single explosion with the same total yield. For shale at this depth, we used a material model previously used for oil shale (Table 3).

Table 3. Shale Material Properties

Compressional Velocity Vp	3910 m/s
Shear Velocity Vs	1830 m/s
Density	2310 kg/m^3
Bulk Modulus K	250x10^8 Pa
High Pressure Modulus B ($P=K\mu+B\mu^2$)	500x10^8 Pa
Shear Modulus G	77.3x10^8 Pa
Zero Pressure Strength τ_0	0.051x10^8 Pa
High Pressure Strength τ_m	2.08x10^8 Pa
Pressure for Maximum Strength P_m	4.90x10^8 Pa
Melt Energy e_m	4.62x10^9 J/m^3

Figure 73 shows the grid used in the calculation. Grid spacing was 20 meters throughout most of the grid, but reduced to 10 meters in the source region in order to allow separation of the inner grids. The initial cavity radius for all three cavities is 6.20 meters. They expand to radii of 22.80, 23.32, and 23.05 meters from bottom to top, respectively. The equivalent single explosion starts with a radius of 8.95 meters and expands to 33.82 meters.

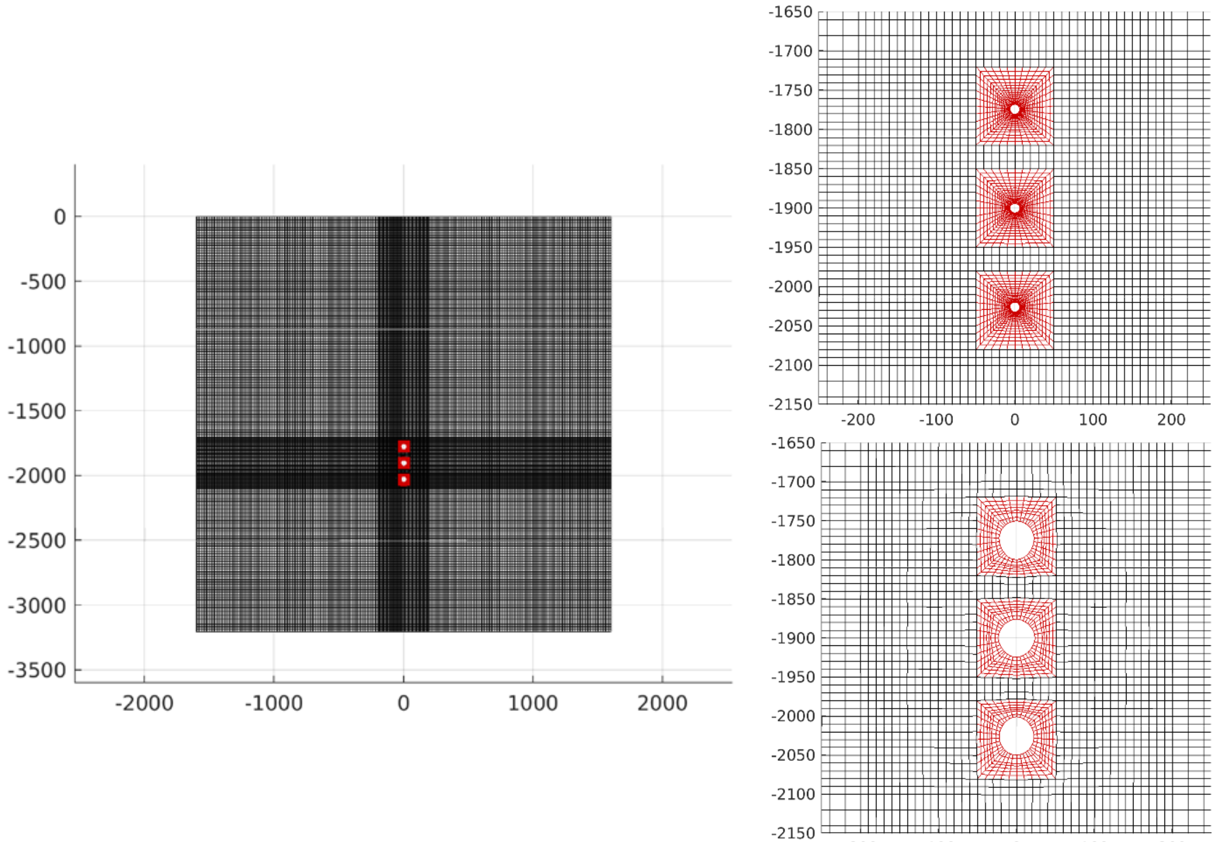

Figure 73. Left: final state of full grid used for Rio Blanco calculation. Top right: Initial state of source region grid; bottom right: final state of source region grid.

Figure 74 shows the regions of nonlinear deformation for the triple and single explosions. Because the explosions are so deep, there is only a small amount of free surface interaction and no tensile cracking occurred.

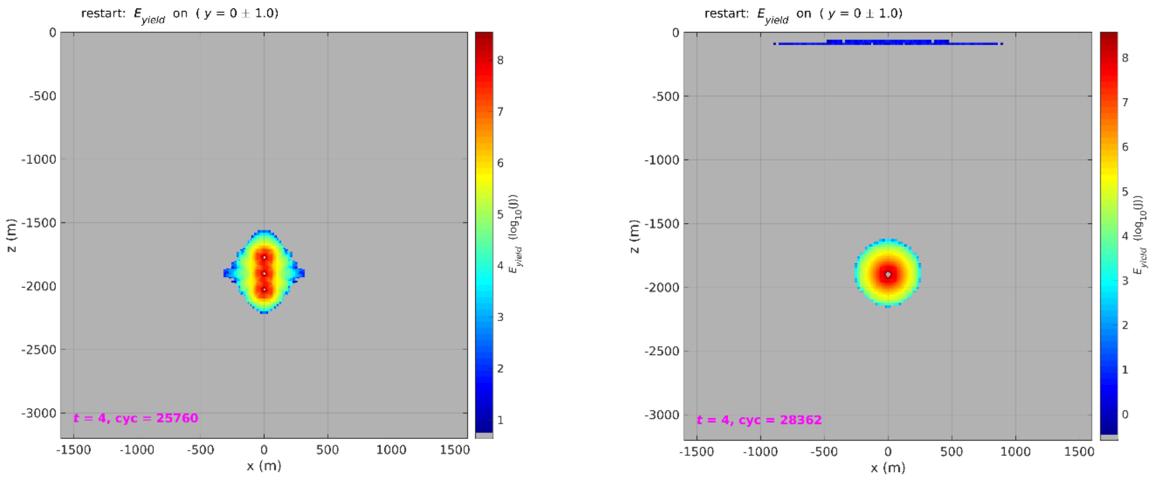

Figure 74. Regions of nonlinear deformation for Rio Blanco (left) and the single explosion equivalent (right).

To propagate the calculation we use the earth structure shown in Figure 75. This is an earth model for the western United States with the properties of the top 3 km modified to correspond to the shale properties used in the calculation. We used this structure for calculations of surface waves and full waveform regional seismograms. For far-field body waves we use a half space with the properties of the top layer. Since the calculation is axisymmetric, we only calculate seismograms in one direction. Body waves were calculated for a takeoff angle of 20º.

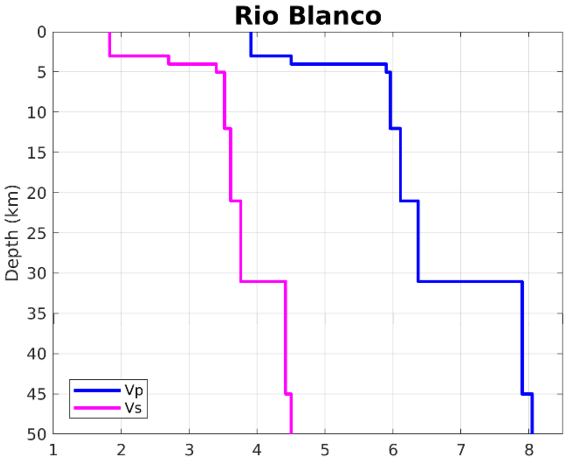

Figure 75. Earth structure used for Rio Blanco calculation. Units are velocity in km/s.

Figure 76 and Figure 77 show the far-field body waves calculated from the two explosion calculations discussed above. Waveforms were low-pass filtered at 20 Hz and 5 Hz, respectively. As with the STELLAR calculations discussed earlier, we find that the far-field body waves at steep takeoff angles (along the axis between the explosions) is reduced for the triple explosion relative to the single explosion, and that this reduction is largest at higher frequencies. However, for the Cram3D calculation with the shale model in place of the salt model, amplitude reductions persist to lower frequencies. The P-wave low-pass filtered at 5 Hz is 40% larger for the single explosion than for the triple explosion. The largest part of the SV phase is pS, and this is also larger for the single explosion than for the triple at 20 Hz, while there is only a small difference at 5 Hz. Figure 78 shows the P and SV spectra. Differences in the P spectra diminish at lower frequencies.

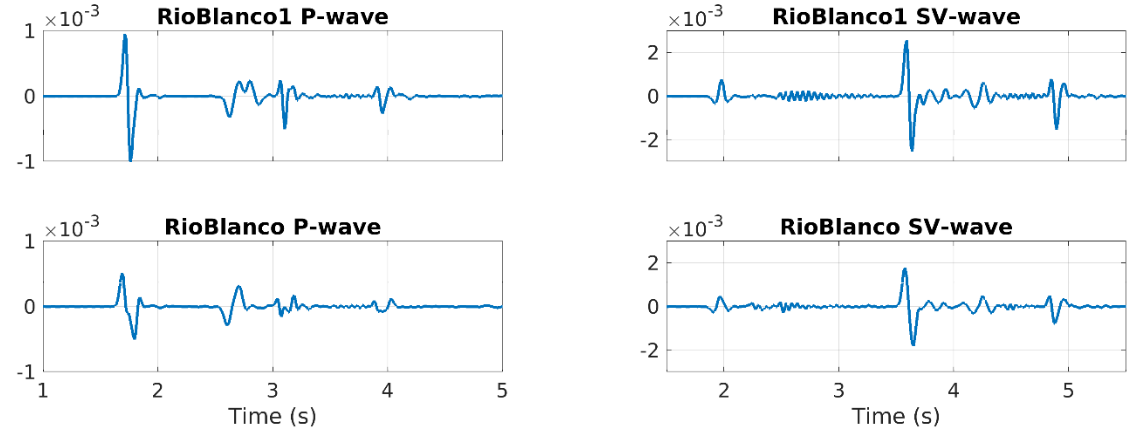

Figure 76. Body waves from the Rio Blanco calculation low-pass filtered at 20 Hz. Top: yield equivalent single explosion. Bottom: Rio Blanco triple explosion. Left: far-field P-wave. Right: far-field SV-wave.

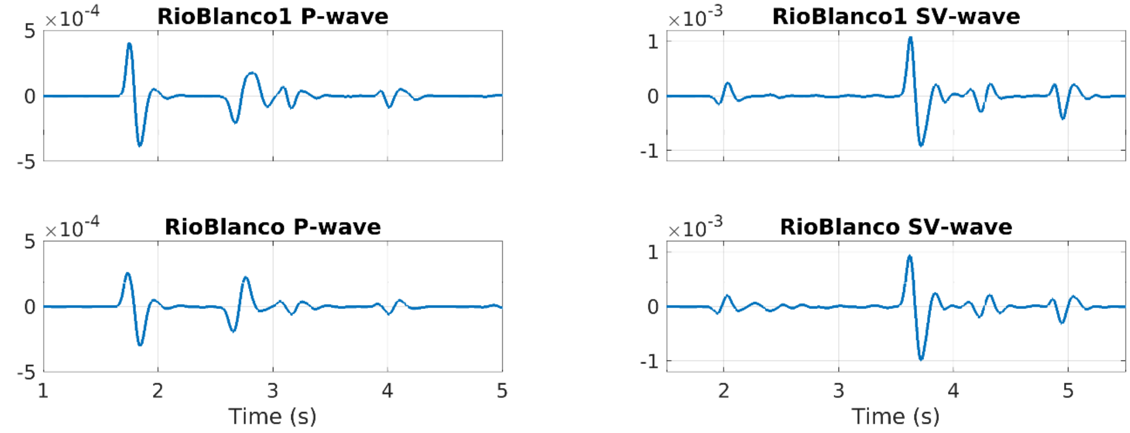

Figure 77. Body waves from the Rio Blanco calculation low-pass filtered at 5 Hz. Top: yield equivalent single explosion. Bottom: Rio Blanco triple explosion. Left: far-field P-wave. Right: far-field SV-wave.

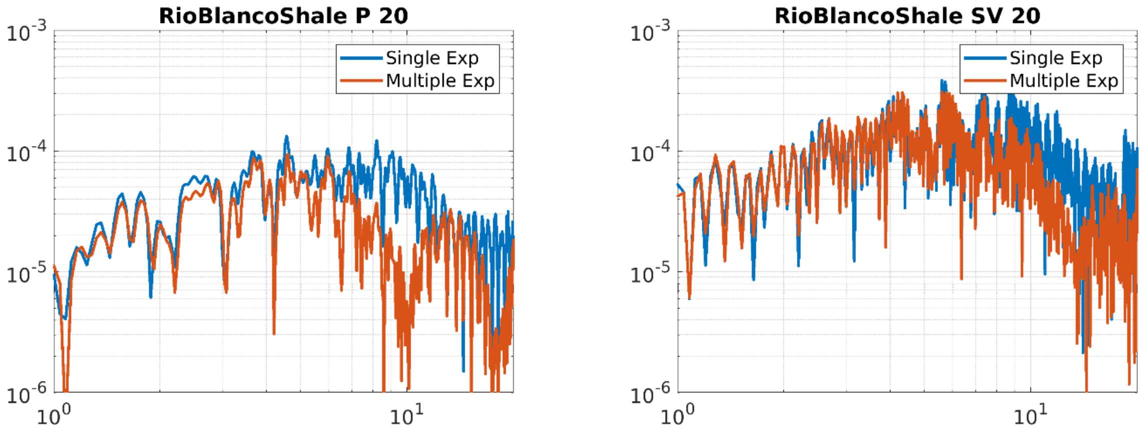

Figure 78. P (left) and SV (right) body wave spectra at a 20 degree takeoff angle.

Figure 79 shows the vertical and horizontal components of the Rayleigh waves calculated from the single and multiple explosion calculations. There is no apparent difference between the waveforms from the single vs. multiple explosions.

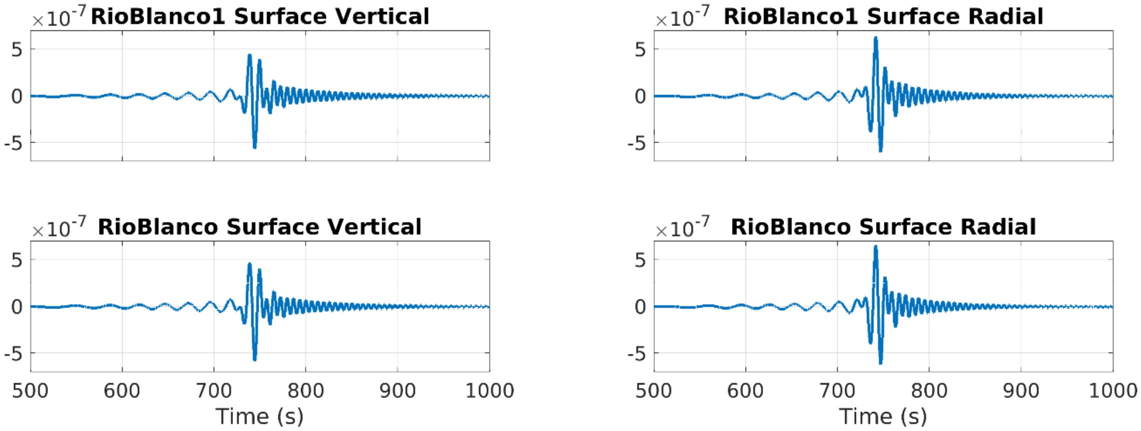

Figure 79. Fundamental mode Rayleigh waves at 2000 km from the Rio Blanco calculations. *Top: yield equivalent single explosion. Bottom: Rio Blanco triple explosion. Left: vertical component. Right: radial component.*

Figure 80 shows the first 12 seconds for the full regional waveform calculated at a distance of 250 km, low-pass filtered at 10 Hz. The waveform from the single explosion is larger, particularly the initial P-wave, which is consistent with the earlier results.

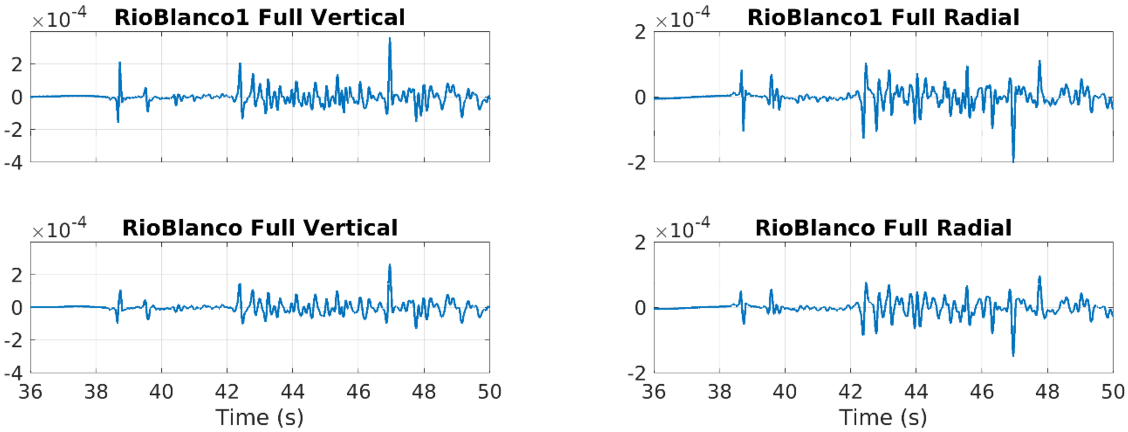

Figure 80. Full regional waveforms at 250 km from the Rio Blanco calculations, limited to early part of the waveform and low-pass filtered at 10 Hz. *Top: yield equivalent single explosion. Bottom: Rio Blanco triple explosion. Left: vertical component. Right: radial component.*

4.3.5 Telkem2

Telkem2 was essentially a smaller version of Taiga. It consisted of three 0.24 kiloton explosions separated by 40 meters and buried at 31.4 meters depth. As with Taiga, it was described as being in sandstone/shale. We initially used the same material model used for Taiga, and a smaller grid spacing because of the smaller yield. We ran the calculation for 0.5 seconds, and found very strong deformation of the cavities and the surface above (Figure 81). At 0.5 seconds there is still upward motion above the cavities and the calculation became unstable at 0.55 seconds.

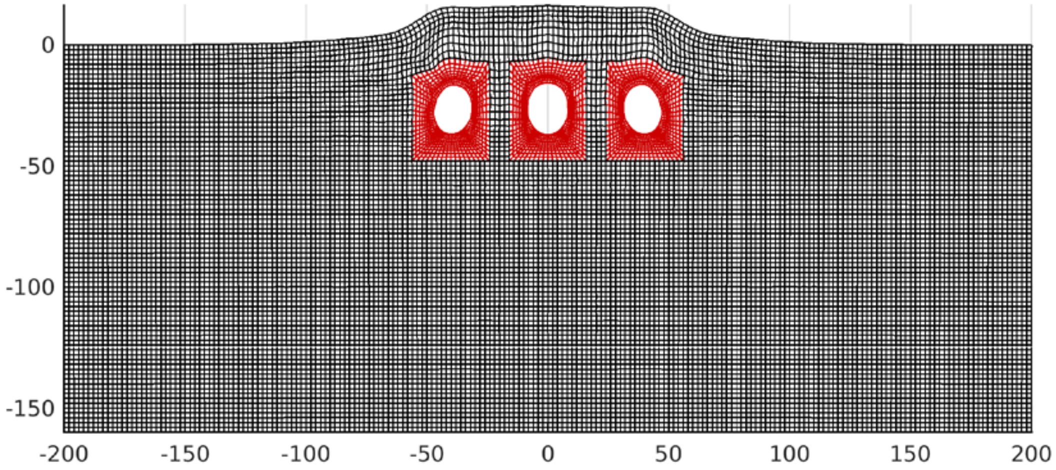

Figure 81. Final grid deformation at 0.5 seconds for the Telkem2 calculation.

To get a stable solution, we changed the material model to the oil shale model used for Rio Blanco. This is a stronger model than the Taiga model which reduces the vertical deformation. We ran the calculation to 1.0 seconds (Figure 82).

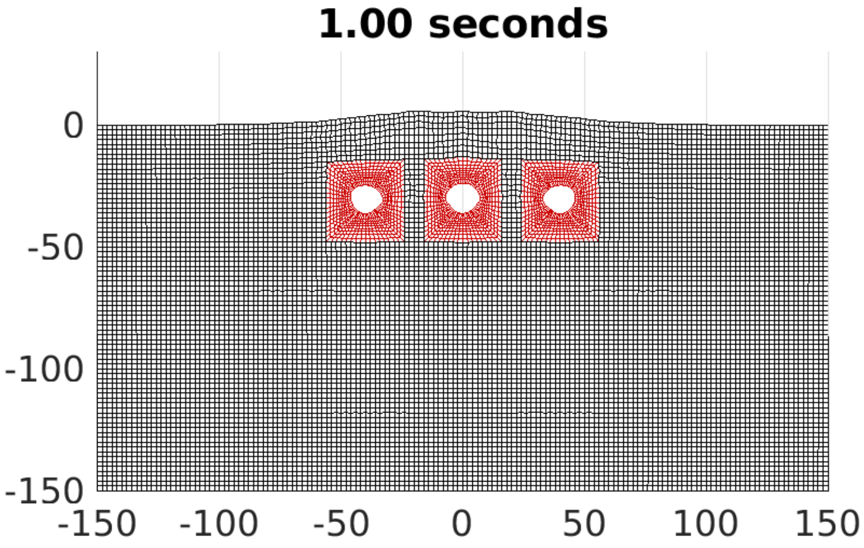

Figure 82. Final state of grid using oil shale model

As with the Taiga material model, the maximum deformation occurs at about 0.5 seconds, but the material then rebounds and returns to smaller vertical deformation. Figure 83 shows the grid shapes at 0.5 and 1.0 seconds, and Figure 84 shows the velocity and displacement at ground zero. By the end of the calculation at 1.0 seconds, the vertical displacement has dropped from 7 meters to 6 meters and is still declining.

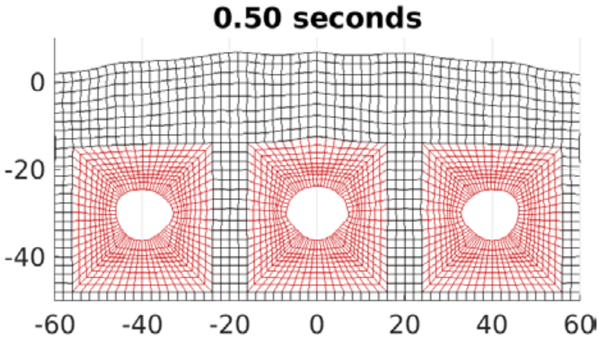

Figure 83. Left: inner grids at 0.5 seconds. Right: inner grids at 1.0 seconds. The vertical deformation is a maximum at 0.5 seconds.

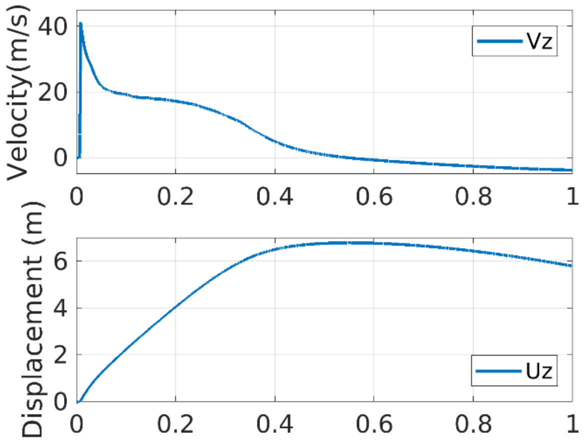

Figure 84. Velocity (top) and displacement (bottom) time histories at ground zero directly above the central cavity.

Regions of plastic yielding and tensile cracking are extensive (Figure 85).

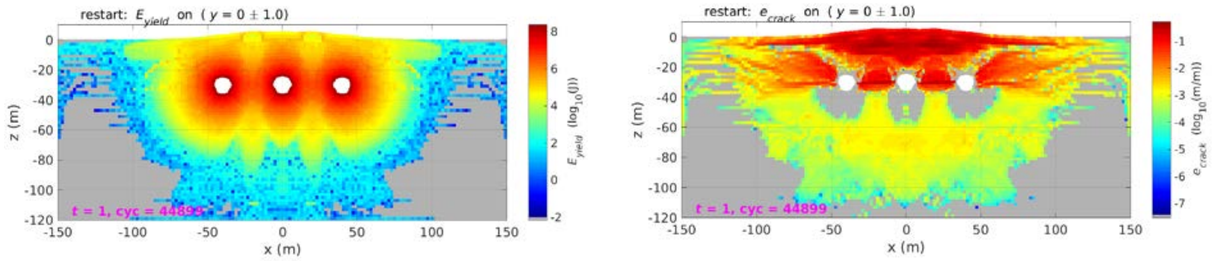

Figure 85. Left: plastic work. Right: tensile cracking.

Figure 86 shows the horizontal displacement at shot depth. The horizontal displacement is largest perpendicular to the direction through the explosion, so we expect larger surface waves in the Y direction. This is similar to the result we found for Dnepr2, and opposite the result for Taiga.

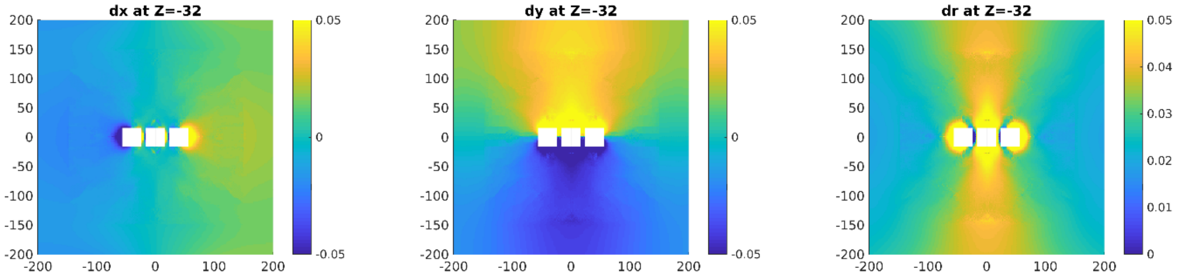

Figure 86. Horizontal displacement at shot depth for Telkem2. From left to right: X, Y and radial displacement.

For the single explosion comparison, we ran two explosions, one at the same shot depth as Telkem2 (31.4 meters) and one at the same scaled depth (45.3 meters), both with a yield of 0.72 kilotons, 3 times that of Telkem2. Figure 87 shows fundamental mode surface waves from the two calculations, together with the Telkem2 surface waves. The Telkem2 results show a maximum at 0 degrees azimuth (Y in the CRAM3D calculation) as expected. The surface wave from the deeper single explosion at the same scaled depth is slightly larger than the surface wave from the explosion at the same depth.

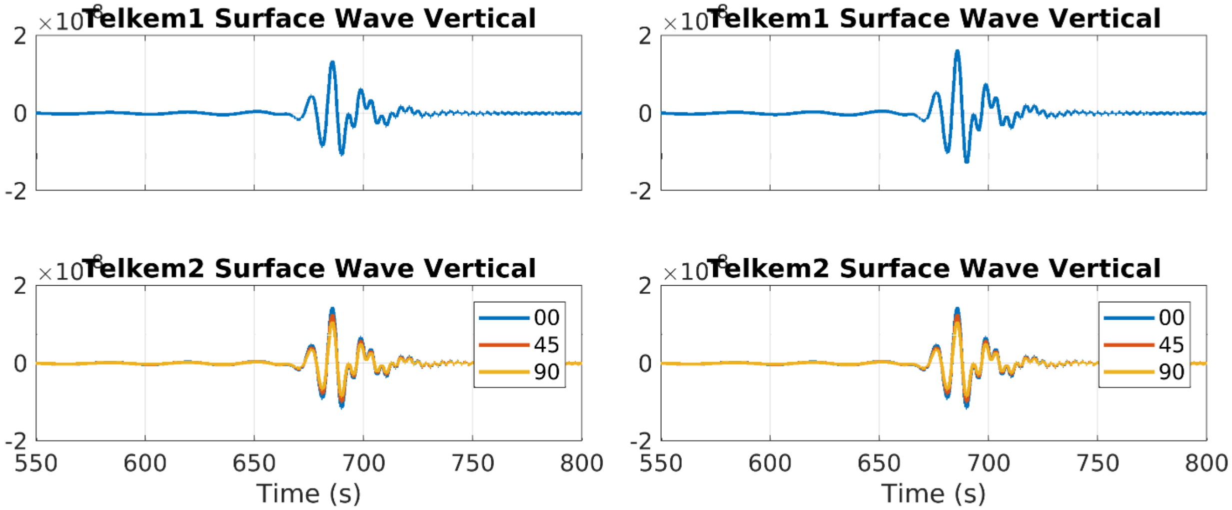

Figure 87. Fundamental mode surface wave at 2000 km from the Telkem2 and Telkem1 calculations. ***Left: Single calculation at the same depth; right at the same scaled depth. Low pass filtered at 10 seconds period.***

Figure 88 shows far-field P-waves, Figure 89 SV-waves and Figure 90 SH waves from the same calculations, all at a take-off angle of 20 degrees from vertical. P-waves are nearly identical for all azimuths and for the multiple explosion and both single explosion calculations. SV waves show some variation in amplitude with azimuth, largest at 0 degrees and smallest at 90 degrees, and the SV wave from the scaled depth single explosion is slightly larger than the SV wave from the single explosion at the same depth as the triple explosion. An SH wave appears at 45 degree azimuth that is about 1/5 the size of the SV wave. SH is zero by symmetry for the other azimuths and the single explosions.

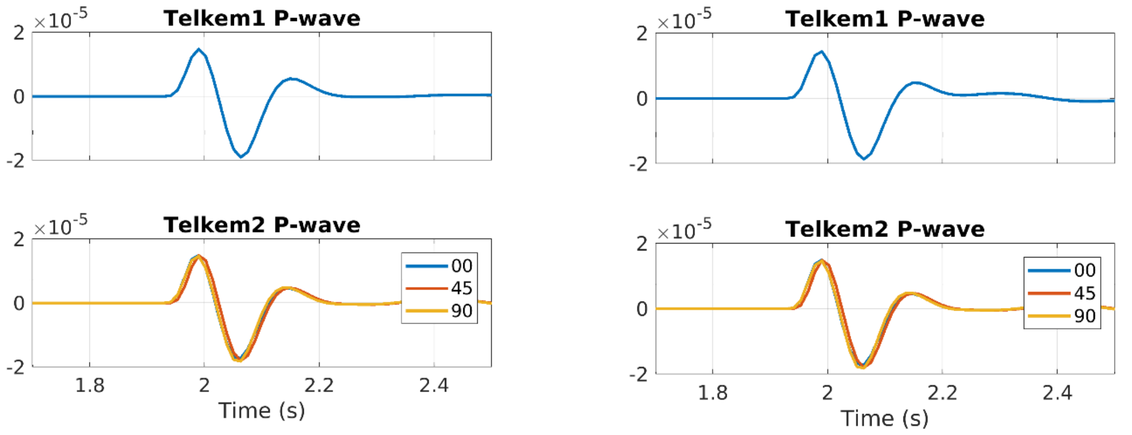

Figure 88. Downgoing P-waves at a takeoff angle of 20 degrees from the Telkem2 and Telkem1 calculations. ***Left: Single explosion calculation at the same depth; right at the same scaled depth. Low pass filtered at 5 seconds period.***

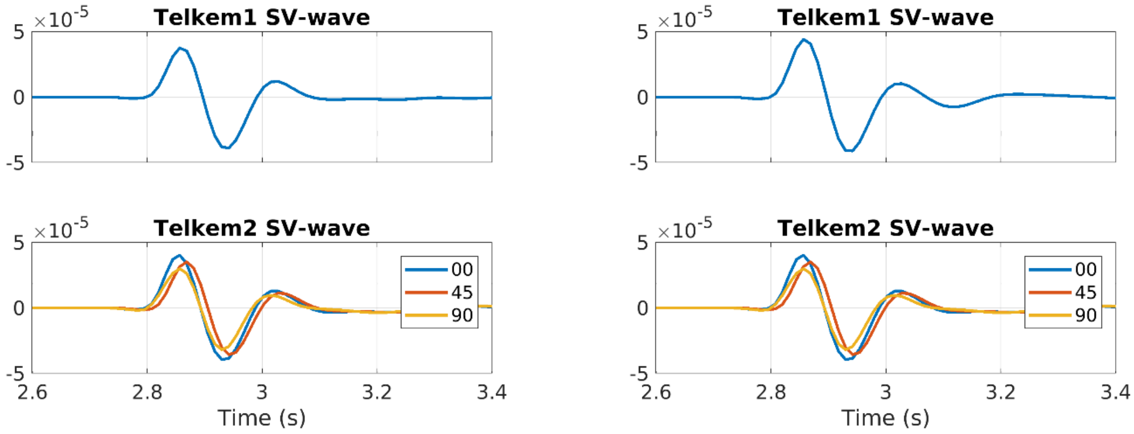

Figure 89. Downgoing SV-waves at a takeoff angle of 20 degrees from the Telkem2 and Telkem1 calculations. ***Left: Single explosion calculation at the same depth; right at the same scaled depth. Low pass filtered at 5 seconds period.***

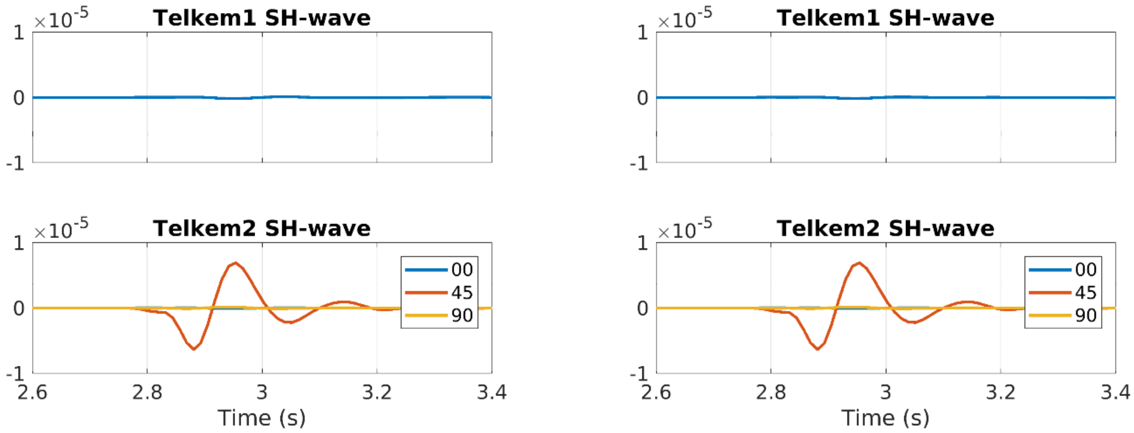

Figure 90. Downgoing SH-waves at a takeoff angle of 20 degrees from the Telkem2 and Telkem1 calculations. ***Left: Single explosion calculation at the same depth; right at the same scaled depth. Low pass filtered at 5 seconds period.***

5. Conclusions

We have performed a set of numerical simulations of multiple near-simultaneous explosions, and evaluated the effect of the close location in time and space on body and surface waves. We did this using two codes, the hydrodynamic Eulerian code STELLAR for whole space calculations, and the Lagrangian finite element code CRAM3D for layered half space calculations. CRAM3D was modified under this project to allow multiple explosions to be calculated. While STELLAR allows a clean calculation of the effect of close multiple explosions on body waves, CRAM3D also includes the important effects of gravity, variable overburden pressure with depth and nonlinear interaction of the shock wave with the free surface.

The STELLAR calculations clearly show the effect of proximity of the explosions and accurately calculate the nonlinear interactions between closely spaced, deep explosions. We find that at low frequencies the far-field body waves are nearly identical to body waves from a single explosion with the same total yield. However at higher frequencies (above ~5 Hz for ~10 kt explosions) differences appear and at sufficiently high frequencies multiple pulses corresponding to each explosion will be visible in directions along the axis of the multiple explosions, while the pulses will combine into a single, larger arrival in the direction perpendicular to the axis (Figure 91).

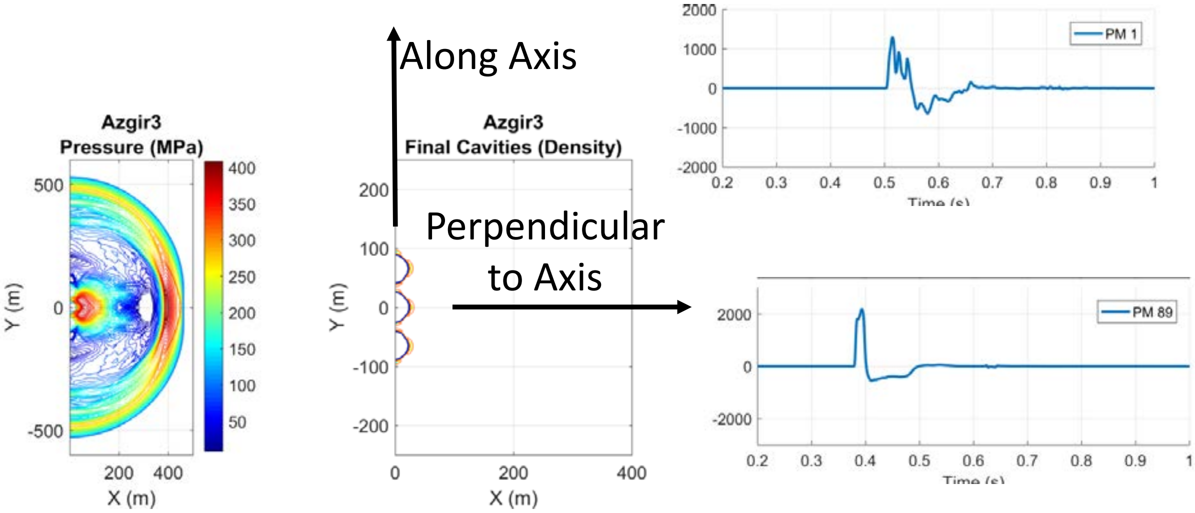

Figure 91. At high frequencies body waves separate into pulses in the direction of the axis, but they combine into an amplified pulse in the perpendicular direction.

We have performed calculations of five multiple explosions with CRAM3D. These include the very shallow Taiga and Telkem2 explosions as well as Azgir1, Dnepr2 and Rio Blanco. We used a material model for shale for Rio Blanco and Telkem2, granite for Dnepr2, salt for Azgir1 and a weak shale/sandstone model for Taiga. For each multiple explosion calculation, we performed a second calculation of a single explosion with the same total yield at the same depth or scaled depth. For Telkem2, we did calculations at both the same depth and scaled depth. The results for far-field body waves are very consistent with the STELLAR calculations, except that they include free surface reflections from the (nonlinear) interaction with the free surface. At longer periods, the body waves are nearly identical for single and multiple explosions except for the generation of SH waves by explosions that are separated horizontally. Multiple explosions that are not axisymmetric exhibit azimuthal variations in surface wave amplitudes and generate Love waves. Unlike the body waves, the radiation pattern in surface wave amplitudes persists to the longest periods. This happens because of asymmetry in the static displacement deformation near the explosion source.

Together with this report, we are delivering a new version of CRAM3D (version 4.0) that includes the ability to calculate multiple explosions.

References

Adushkin, V.V. and A.A. Spivak (2007), Underground explosions (in Russian), Nauka, Moscow.

Apsel, R. J. and J. E. Luco (1983), On the Green's Functions for a layered half-space, Part II, Bull. Seismol. Soc. Am., 73, pp. 931-951.

Bache, T. C. and D. G. Harkrider (1976), The body waves due to a general seismic source in a layered earth model, Bull. Seismol. Soc. Am., 66, pp. 1805-1819.

Bache, T. C., S. M. Day, and H. J. Swanger (1982), Rayleigh wave synthetic seismograms from multi-dimensional simulations of underground explosions, Bull. Seismol. Soc. Am., 72, pp. 15-28.

Colella, P. and P. R. Woodward (1984), The Piecewise Parabolic Method (PPM) for Gas-Dynamical Simulations, Journal of Computational Physics, 54, pp. 174-201.

Luco, J. E. and R. J. Apsel (1983), On the Green's Functions for a layered half-space, Part I, Bull. Seismol. Soc. Am., 73, pp. 909-929.

Murphy, J. R. and B. W. Barker (2001), Application of Teleseismic P-wave Spectra to Seismic Yield Estimation of Underground Nuclear Explosions, Pure Appl. Geophys., 158, pp. 2123-2171, doi: 10.1007/PL00001144.

Rimer, N., T. Barker, S. Rogers, J. Stevens, and D. Wilkins (1994), Simulation of seismic signals from partially coupled nuclear explosions in cylindrical tunnels, Rep. DNA-TR-94-136, Defense Nuclear Agency, Alexandria, VA, August.

Russian Federation for Atomic Energy (1996), *USSR Nuclear Weapons Tests and Peaceful Nuclear Explosions, 1949 through 1990,* Russian Federation Nuclear Center – VNIIEF, ISBN 5-85165-062-1.

Stevens, J. L., T. G. Barker, S. M. Day, K. L. McLaughlin, N. Rimer, and B. Shkoller (1991), Simulation of teleseismic body waves, regional seismograms, and Rayleigh wave phase shifts using two-dimensional nonlinear models of explosion sources, AGU Geophysical Monograph 65: Explosion Source Phenomenology, S. Taylor, H. Patton, P. Richards, editors, ISBN 0-87590-031-3, pp. 239-252, doi:10.1029/GM065p0239.

Stevens, Jeffry L., Heming Xu, Michael O’Brien, Walter Nagy, and Norton Rimer (2011), Wave propagation from complex 3D sources using the representation theorem, AFRL-RV-HA-TR-2011-1019, SAIC, San Diego, CA, March.

Stevens, J. L., T. W. Thompson, and M. O’Brien (2014), Seismic Wave Generation and Propagation from Complex 3D Explosion Sources, AFRL-RV-PS-TR-2014-0084, Leidos, San Diego, CA, April.

Stevens, J. L., M. O’Brien, and T. W. Thompson (2017), Decomposition of the Seismic Source Using Numerical Simulations and Observations of Nuclear Explosions, AFRL-RV-PS-TR-2017-0120, Leidos, San Diego, CA, May.

Sultanov, D. D., J. R. Murphy and Kh. D. Rubinstein (1999), “A Seismic Source Summary for Soviet Peaceful Nuclear Explosions,” Bull. Seism. Soc. Am., 89, pp. 640-647.

Von Seggern, D. H. (1974), Analysis of Seismic Data for the Rio Blanco Explosion, Teledyne Geotech, Alexandria, VA, SDAC-TR-74-9, available at http://www.dtic.mil/dtic/tr/fulltext/u2/a005781.pdf.

List of Symbols, Abbreviations, and Acronyms

AFRL	Air Force Research Laboratory
ANFO	Ammonium Nitrate and Fuel Oil
PPM	Piecewise Parabolic Method
TOA	Take-off Angle

DISTRIBUTION LIST

DTIC/OCP
8725 John J. Kingman Rd, Suite 0944
Ft Belvoir, VA 22060-6218 1 cy

AFRL/RVIL
Kirtland AFB, NM 87117-5776 1 cy

Official Record Copy
AFRL/RVBYE/Dr. Frederick Schult 1 cy